Pure

Bangor University

DOCTOR OF PHILOSOPHY

NEXAFS Spectroscopy Studies of Polymer Nanocomposites

Winter, Allen

Award date:
2017

Awarding institution:
Bangor University

Link to publication

General rights
Copyright and moral rights for the publications made accessible in the public portal are retained by the authors and/or other copyright owners and it is a condition of accessing publications that users recognise and abide by the legal requirements associated with these rights.

- Users may download and print one copy of any publication from the public portal for the purpose of private study or research.
- You may not further distribute the material or use it for any profit-making activity or commercial gain
- You may freely distribute the URL identifying the publication in the public portal ?

Take down policy
If you believe that this document breaches copyright please contact us providing details, and we will remove access to the work immediately and investigate your claim.

Download date: 26. Apr. 2024

PRIFYSGOL
BANGOR
UNIVERSITY

NEXAFS Spectroscopy Studies of Polymer Nanocomposites

By

Allen Douglas Winter

Supervisor: Dr. Eva M. Campo

Submitted in partial fulfilment of the requirements
for the degree of Doctor of Philosophy
in Electronic Engineering

College of Physical and Applied Sciences
School of Electronics

January 2017

Publications

Journal articles

1. A. D. Winter, W. Y. Rojas, A. D. Williams, S. S. Kim, F. Ouchen, D. A. Fischer, C. Weiland, E. Principe, S. Banerjee, C. Huynh, R. R. Naik, Y. Liu, A. Mehta, J. Grote, D. Prendergast, and E. M. Campo. Monitoring deformation in graphene through hyperspectral synchrotron spectroscopy to inform fabrication. *Submitted* 2016.

2. W. Y. Rojas, A. D. Winter, J. Grote, S. S. Kim, A. D. Williams, C. Weiland, E. Principe, D. A. Fischer, S. Banerjee, D. Prendergast, and E. M. Campo. Strain and bond length dynamics upon growth and transfer of graphene by NEXAFS spectroscopy. *Submitted* 2016.

3. E. M. Campo, D. Yates, B. Berson, W. Y. Rojas, A. D. Winter, M. Ananth, J. J. Santiago-Aviles, and E. M. Terentjev. Tomography of electrospun carbon nanotube polymeric blends by focus ion beam: alignment and phase separation analysis from multicontrast electron imaging. *Macromolecular Chemistry and Physics, Accepted* 2016.

4. A. D. Winter, K. Czaniková, E. Larios, V. Vishniyakov, C. Jaye, D. A. Fischer, M. Omastová, and E. M. Campo. Interface dynamics in strained polymer nanocomposites: Stick-slip wrapping as a prelude to mechanical backbone twisting derived from sonication-induced amorphization. *The Journal of Physical Chemistry C*, **119**: 20091–20099, 2015.

5. A. D. Winter, C. Jaye, D. A. Fischer, M. Omastová, and E. M. Campo. Prestrain relaxation in non-covalently modified ethylene-vinyl acetate | PyChol | multiwall carbon nanotube nanocomposites. *APL Materials*, **2**: 066105, 2014.

6. A. D. Winter, E. Larios, F. M. Alamgir, C. Jaye, D. A. Fischer, M. Omastová, and E. M. Campo. Thermo-active behaviour of ethylene-vinyl acetate | multiwall carbon nanotube composites examined by in situ near edge x-ray absorption fine structure spectroscopy. *The Journal of Physical Chemistry C*, **118**: 3733–3741, 2014.

7. A. D. Winter, E. Larios, F. M. Alamgir, C. Jaye, D. A. Fischer, and E. M. Campo. Near-edge x-ray absorption fine structure studies of electrospun poly (dimethylsiloxane)/poly (methyl methacrylate)/multiwall carbon nanotube composites. *Langmuir*, **29**: 15822–15830, 2013.

Conference proceedings

1. A. D. Winter, C. Jaye, D. A. Fischer, M. Omastová, and E. M. Campo. Molecular Disorder in Prestrained Nanocomposites: Effects of Processing on Durability of Thermally-Active Ethylene-Vinyl Acetate | PyChol | Multiwall Carbon Nanotubes. *MRS Proceedings*, **1718**, 2015.

2. A. D. Winter, E. Larios, C. Jaye, D. A. Fischer, M. Omastová, and E. M. Campo. Thermo-active polymer nanocomposites: a spectroscopic study. *SPIE NanoScience+Engineering*, 2014.

3. A. D. Winter, E. Larios, F. M. Alamgir, C. Jaye, D. A. Fischer, and E. M. Campo. Polymer-carbon nanotube composites: electrospinning, alignment and interactions. *SPIE NanoScience+Engineering*, 2014.

Book chapters

1. A. D. Winter, E. Larios, C. Jaye, C. Weiland, E. Principe, M. Omastová, and E. M. Campo. Noncovalent Interactions in Polymer Nanocomposites. *New Horizons in Nanoscience and Engineering* ed. by D. L. Andrews and J. G. Grote. Bellingham, Washington: SPIE Press, 2015. Chap. 4, 147–190.

Acknowledgements

First and foremost, I wish to express my deep gratitude to my PhD supervisor, Dr. Eva Campo, for her continued support and encouragement over the past four years. Her advice in times of panic was invaluable. Thanks to her expert guidance, I feel I have really matured as a scientist. And then there's all the pizzas she treated us to!

I'd like to thank Dr. James Wang and Prof. Alan Shore, who formed my PhD committee and offered constructive criticisms which always improved the quality of my work. Also in the department, many thanks to Dr. Yanhua Hong for her training in AFM and Raman spectroscopy, and Dr. Iestyn Pierce, who always made time for me when I needed external input.

My sincere thanks also goes to Peter Albrecht, Conan Weiland, and Cherno Jaye for their teaching and training in NEXAFS spectroscopy at the National Synchrotron Light Source, Brookhaven National Laboratory.

I thank my colleague Wudmir Rojas for insightful discussions and his input from a theoretical perspective. His patience when attempting to teach me Density Functional Theory is to be commended.

I'd like to thank Bangor University for the award of the Anniversary Research Studentship, and the Air Force Office of Scientific Research, who awarded me funding to support my final PhD year.

I am extremely grateful to my parents Allen and Nora, and my younger brothers John, Paul, and Michael. Even though they were 12460.6 km away, their emotional and spiritual support was felt every day.

Lastly, my love and gratitude to Natalie, my wife-to-be. You have always been there to celebrate my triumphs and support me through my trials. I really could not have done this without you constantly by my side.

Abstract

Polymer nanocomposites, with the huge range of property sets (both structural and functional) they can exhibit, could pave the way towards "materials by design"—one of the promises of nanotechnology. Hindering the mass adoption of polymer nanocomposites is a limited understanding of the complex relationship between processing steps, structural parameters at the nanoscale, and resulting macroscale bulk properties. To this end, the work presented in this thesis reports on the investigations of four polymer nanocomposite case studies, each addressing effects of different variables, through NEXAFS spectroscopy—a synchrotron technique that offers rich chemical and structural information. In the first case study, non-covalent interactions resulting from electrospinning of a polymer blend of polydimethylsiloxane–poly (methyl metacrate) filled with carbon nanotubes are addressed, as well as effects of nanofiller diameter. The second study investigates the thermoactive behaviour of ethylene vinyl acetate | multiwall carbon nanotube composites through *in situ* temperature-resolved NEXAFS spectra, and an actuation mechanism is proposed. The third case study explores ageing effects of this thermoactive nanocomposite, and reports on the lifetime of non-covalent interactions. Finally, the fourth case study explores the effects of excessive sonication, which is seen here to drastically damage nanofiller and resulting matrix–filler interactions. This work represents four additional points in a growing dataset from other studies of polymer nanocomposites that—when sufficiently populated—could be mined through clustering algorithms and machine learning approaches to extract the elusive processing–structure–property link, which will enable the wide-spread exploitation of polymer nanocomposite technology.

Contents

1 Introduction **1**

1.1 Aims and Objectives 4

1.2 Thesis outline 5

2 Carbon nanotubes and polymer nanocomposites **8**

2.1 Carbon Nanotubes 8

2.1.1 CNT synthesis 9

2.1.2 Applications 11

2.2 Polymer nanocomposites 14

2.2.1 Dispersion strategies 14

2.2.2 Alignment solutions 17

2.2.3 CNT functionalisation 19

2.2.4 State-of-the-art polymer nanocomposites 20

3 Synchrotron radiation and NEXAFS spectroscopy **36**

3.1 Synchrotron radiation 36

3.2 Synchrotron components 37

3.2.1 Linear accelerator 38

3.2.2 Booster ring 38

3.2.3 Storage ring 38

3.2.4 Beamlines 39

3.3 NEXAFS spectroscopy 40

3.3.1 NEXAFS principles 41

3.3.2 Calibration and post-processing 44

3.4 Related NEXAFS research 46

4 Electrospun PDMS–PMMA|MWCNT composites **52**

4.1 Introduction 52

4.2 Experimental 53

4.2.1 Materials and reagents 53

4.2.2 Electrospinning 54
4.2.3 NEXAFS spectroscopy 55
4.2.4 Scanning and Transmission Electron Microscopy 56
4.3 Spectral analysis 57
4.3.1 Spectral identification 57
4.3.2 Alignment, homogeneity, molecular conformation 59
4.4 Non-covalent interaction models 61
4.5 Linear combination analysis 63
4.6 Summary 67

5 EVA|MWCNT composites: Thermoactive behaviour 74
5.1 Introduction 74
5.2 Experimental 75
5.2.1 Materials and reagents 75
5.2.2 Nanocomposite fabrication 75
5.2.3 *In situ* temperature-resolved NEXAFS spectroscopy 76
5.3 Spectral identification 77
5.4 Nanoparticle dispersion and alignment 79
5.5 Actuation: Temperature-resolved NEXAFS analysis 80
5.6 Actuation model 84
5.7 Summary 86

6 Ageing-derived failure of EVA|MWCNT composites 90
6.1 Introduction 90
6.2 Ageing effects in NEXAFS spectroscopy 91
6.3 Failure of active behaviour 95
6.4 Summary 99

7 Excessive sonication in EVA|MWCNT composites 102
7.1 Introduction 102
7.2 Experimental 103
7.2.1 Nanocomposite fabrication 103
7.2.2 Characterisation 103
7.3 Damage to graphitic structure 103
7.4 Load transfer 107
7.5 Angular- and strain-resolved NEXAFS spectroscopy 108
7.6 Model: stick-slip dynamics and backbone twisting 110

7.7 Summary 113

8 Conclusions **118**

A Collaborations and authorship **122**

Chapter 1

Introduction

Advances in every technological field demand simultaneous advances in materials—be it improvements or modification of properties, or added functionality. Polymers are a prime platform for these new materials, given their low cost and unsurpassed versatility in mechanical properties. As an example, elastomeric fibres have a tensile strength of 4–9 MPa and a Young's modulus of 0.01–0.03 GPa, while M5 fibres (high performance synthetic fibres developed by Azko Nobel) have a tensile strength of up to 9 GPa and a Young's modulus of 330–350 GPa—higher even than Kevlar®.[1] Even with such high performance polymeric fibres, mechanical properties achieved experimentally are a fraction of theoretical predictions.[1]

Further improvements to polymer properties have been achieved through polymer blends and composites, now a principle material class in the polymer industry.[2] Composite materials consist of three components: the matrix (usually polymer, metal or ceramic), reinforcement filler, and the interface.[3] Each of these materials is chemically different and has distinct properties, making composites different to alloys. The high filler content required for traditional polymer composites, however, compromises the neat matrix properties which makes polymers attractive materials in the first place, such as mechanical properties and processability.[2]

Research for new and improved advanced materials has now shifted to the field of polymer nanocomposites (PNCs), i.e. polymer matrices filled with filler materials having at least one dimension in the 1–100 nm scale. Compared to conventional composites, considerably better mechanical properties can be achieved in PNCs, partly due to the lower filler content required to produce sufficient change in properties.[4] Further, while traditional microcomposites were fabricated to improve existing properties in the matrix, addition of nanofillers has been widely reported to result in not only new structural properties—absent in the pristine matrix—

[1] K. Song et al. *Materials*, **6**: 2543–2577, 2013.
[2] R. A. Vaia and H. D. Wagner. *Mater. Today*, **7**: 32–37, 2004.
[3] E. T. Thostenson, C. Li, and T.-W. Chou. *Compos. Sci. Technol.*, **65**: 491–516, 2005.
[4] G. Armstrong. *Eur. J. Phys.*, **36**: 063001, 2015.

but also new functional properties suitable for sensors and actuators.[5–9] The wide range of both polymeric matrices and nanofillers available could potentially result in an immense range of property sets suitable for many applications. In fact, polymer nanocomposites have already found initial commercial applications in a variety of fields including electronics, energy, and even clothing,[10] and the global market for this class of materials was predicted to exceed $5100 million by 2020.[4]

Carbon nanotubes (CNTs) have long been considered suitable fillers for both structural and functional PNCs, given their very large aspect ratios and extraordinary mechanical (Young's modulus and tensile strength of up to 1.2 TPa and 2 GPa respectively), electrical (conductivities of $10^6 - 10^7$ Sm^{-1}), thermal (6000 $Wm^{-1}K^{-1}$) and optical properties.[2,3,10,11] Additionally, they are at present being manufactured with a range of properties (dimensions, purity, etc) at a reasonable cost.[12] Along with layered silicates, CNTs are the most investigated filler in the field of PNCs.[2] A more in-depth description of CNTs is given in Chapter 2.

The transition from the micro to the nanoscale yields drastic changes in the fundamental physics within PNCs, dramatically altering the physical properties of the system. Nanofillers have very high surface areas per unit volume, which causes a large increase in the size of the interfacial area.[3] In constrast to conventional composites whose properties are determined by the filler dimensions,[4] the properties of PNCs are dominated by the properties of the matrix–filler interface.[3] Additionally, presence of nanofillers in PNCs results in comparable filler dimension, particle–particle distances, polymer radius of gyration (describing chain dimensions), and size of interfacial region.[2] The implications of this are important, since certain property sets nucleate when the morphology length scales coincide with length scales of fundamental physics pertaining to these properties.[2]

Given the wealth of possible property sets potentially affordable by PNCs, why is this technology not yet ubiquitously exploited? The obstacle is a lack of understanding of the processing–structure–property relationship (Figure 1.1), which prevents the prediction and tailoring of PNC properties to meet specific requirements.[13] As discussed above, the established corresponding link pertaining to conventional microcomposites does not apply to PNCs.[4]

[5] Z. Li et al. *Polymer*, **85**: 67–76, 2016.
[6] K. Hayashida and Y. Matsuoka. *Carbon*, **85**: 363–371, 2015.
[7] O. Breuer and U. Sundararaj. *Polym. Compos.*, **25**: 630–645, 2004.
[8] P. M. Ajayan et al. *Adv. Mater.*, **12**: 750–753, 2000.
[9] S. V. Ahir and E. M. Terentjev. *Nat. Mater.*, **4**: 491–495, 2005.
[10] M. F. L. De Volder et al. *Science*, **339**: 535–539, 2013.
[11] S. Iijima. *Nature*, **357**: 56–58, 1991.
[12] Y. Y. Huang and E. M. Terentjev. *Adv. Funct. Mater.*, **20**: 4062–4068, 2010.
[13] J. Jancar et al. *Polymer*, **51**: 3321–3343, 2010.

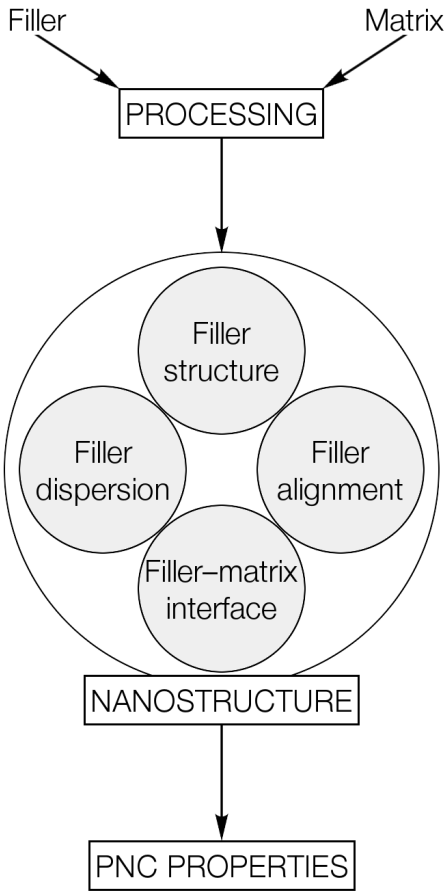

Figure 1.1: Prediction and tailoring of PNC properties requires an in-depth understanding of the processing–structure–property relationship.

Four key nanostructural parameters conditioning resulting PNC properties have been identified (described in more detail in Chapter 2): filler structure (which determines its properties), filler dispersion within the matrix, orientational order of nanofillers (i.e. alignment), and the filler–matrix interface, where the ultimate PNC properties are thought to nucleate.[3,4,14] These are firstly dependent on processing schemes, but also share a complex interdependence with each other.[13] For instance, sonication is a commonly-used technique to break CNT bundles and produce an efficient dispersion within a polymeric matrix, but—being a highly energetic procedure—can compromise the CNT structure, and therefore affect the interactions at the filler–matrix interface. In turn, the new interactions may limit effectiveness of alignment solutions. Similarly, CNTs (which are chemically innert) may be covalently functionalised to ensure strong interactions at the filler–matrix interface, but this necessarily damages the CNT structure responsible for its remarkable properties.

A good illustration of the fine sensitivity of resulting bulk properties to nanostructural

[14]G. Mittal et al. *J. Ind. Eng. Chem.*, **21**: 11–25, 2015.

variables can be found in a study by Huang and Terentjev, who produced polydimethylsiloxane (PDMS)|MWCNT composites via several distinct processing schemes.[12] Each differently processed composite displayed different electrical properties, even though the chemistry was identical.[12] Their work highlights both the difficulties pertaining to reproducibility, and the need of a thorough understanding of the processing–structure relationship, which would pave the way towards tailoring PNC properties for different applications.

How nanoscale phenomena, dependent on structural parameters, propagate to the macroscale resulting in a given property set (structure–property paradigm) is unknown. Few models have been proposed, and these are heavily disputed.[13] In the absence of bridging laws linking nanoscale phenomena and the macroscale continuum, it would be a difficult task—even given an established processing–structure relationship—to predict bulk properties.[13] However, there is a growing wealth of published works on specific PNC systems, specifying particular materials, processing schemes, and ultimate properties. In line with the Materials Genome Initiative,[15] this body of work could be used as a rich data source, which could then be analysed with clustering algorithms and machine learning approaches to establish the much needed processing–structure–property link.[16]

1.1 Aims and Objectives

The goal of this thesis is to further understanding of the processing–structure relationship in PNCs through the investigation of different case studies, thus contributing to the aforementioned PNC system database in the vein of the Materials Genome Initiative.[17] The experimental technique of choice is Near Edge X-ray Absorption Fine Structure (NEXAFS) spectroscopy, which probes the unoccupied molecular states pertaining to specific absorbing atoms, and offers rich information on chemistry and structure. The technique is discussed in detail in Chapter 3. Conclusions from this synchrotron technique are complemented by more commonplace techniques such as Raman spectroscopy and atomic force microscopy (AFM).

[15] A. Jain et al. *APL Mater.*, **1**: 011002, 2013.
[16] C. M. Breneman et al. *Adv. Funct. Mater.*, **23**: 5746–5752, 2013.
[17] E. M. Campo. *SPIE Professional*, **July**: 14–15, 2016.

1.2 Thesis outline

Each of the case studies reported here focusses on structural and functional effects of specific processing schemes, as well as dynamics of resulting non-covalent interactions.[†] Chapter 4 reports findings on an electrospun polymeric blend of PDMS and poly(methyl methacrylate) (PMMA) filled with unmodified MWCNTs of two different diameters. Angle-resolved NEXAFS spectra reveal strong anisotropic structure, and nanotube alignment—induced by electrospinning—is confirmed by scanning electron microscopy. Spectra indicate a CNT diameter-dependent interaction, and two non-covalent interaction models addressing all findings are proposed. In the final section of the chapter, an extension of the well-known linear combination analysis method is employed, aimed at isolating the spectral signature of the polymer–CNT interaction. Chapter 5 is an investigation of thermoactive ethylene vinyl acetate (EVA)|MWCNT composites using *in situ* temperature-resolved NEXAFS spectroscopy. In this PNC system, nanotubes were non-covalently functionalised with a novel compatibiliser to aid dispersion and enhance polymer–CNT interactions, and CNT alignment was induced through strain. *In situ* actuation reveals a coupled intensity interplay of NEXAFS resonances, upon which an actuation mechanism model is proposed. The same PNC system was studied a year later, reported in Chapter 6, to investigate ageing effects on non-covalent interactions. Evidence of strain relaxation was observed through NEXAFS spectra and AFM. Further, spectral trends related to thermal actuation were no longer present. Thus, the failure mechanism is proposed, along with a semi-quantitative measure of failure extent. Chapter 7 reports on a PNC system with identical chemistry, but processed under an 'agressive' sonication scheme. NEXAFS spectroscopy reveals a very different system, and the interaction dynamics are investigated using increasing uniaxial strain as a probe.

[†]The work presented here is the result of multiple collaborations. Appendix A, 'Collaborations and authorship', specifies per chapter the work performed by the candidate, and credits the rest to the appropriate collaborators.

Bibliography

[1] K. Song, Y. Zhang, J. Meng, E. C. Green, N. Tajaddod, H. Li, and M. L. Minus. Structural polymer-based carbon nanotube composite fibers: understanding the processing–structure–performance relationship. *Materials*, **6**: 2543–2577, 2013.

[2] R. A. Vaia and H. D. Wagner. Framework for nanocomposites. *Materials Today*, **7**: 32–37, 2004.

[3] E. T. Thostenson, C. Li, and T.-W. Chou. Nanocomposites in context. *Composites Science and Technology*, **65**: 491–516, 2005.

[4] G. Armstrong. An introduction to polymer nanocomposites. *European Journal of Physics*, **36**: 063001, 2015.

[5] Z. Li, M. Tang, J. Dai, T. Wang, and R. Bai. Effect of multiwalled carbon nanotube-grafted polymer brushes on the mechanical and swelling properties of polyacrylamide composite hydrogels. *Polymer*, **85**: 67–76, 2016.

[6] K. Hayashida and Y. Matsuoka. Electromagnetic interference shielding properties of polymer-grafted carbon nanotube composites with high electrical resistance. *Carbon*, **85**: 363–371, 2015.

[7] O. Breuer and U. Sundararaj. Big returns from small fibers: a review of polymer/carbon nanotube composites. *Polymer composites*, **25**: 630–645, 2004.

[8] P. M. Ajayan, L. S. Schadler, C. Giannaris, and A. Rubio. Single-walled carbon nanotube-polymer composites: strength and weakness. *Advanced Materials*, **12**: 750–753, 2000.

[9] S. V. Ahir and E. M. Terentjev. Photomechanical actuation in polymer-nanotube composites. *Nature Materials*, **4**: 491–495, 2005.

[10] M. F. L. De Volder, S. H. Tawfick, R. H. Baughman, and A. J. Hart. Carbon nanotubes: present and future commercial applications. *Science*, **339**: 535–539, 2013.

[11] S. Iijima. Helical microtubules of graphitic carbon. *Nature*, **357**: 56–58, 1991.

[12] Y. Y. Huang and E. M. Terentjev. Tailoring the electrical properties of carbon nanotube–polymer composites. *Advanced Functional Materials*, **20**: 4062–4068, 2010.

[13] J. Jancar, J. F. Douglas, F. W. Starr, S. K. Kumar, P. Cassagnau, A. J. Lesser, S. S. Sternstein, and M. J. Buehler. Current issues in research on structure–property relationships in polymer nanocomposites. *Polymer*, **51**: 3321–3343, 2010.

[14] G. Mittal, V. Dhand, K. Y. Rhee, S.-J. Park, and W. R. Lee. A review on carbon nanotubes and graphene as fillers in reinforced polymer nanocomposites. *Journal of Industrial and Engineering Chemistry*, **21**: 11–25, 2015.

[15] A. Jain, S. P. Ong, G. Hautier, W. Chen, W. D. Richards, S. Dacek, S. Cholia, D. Gunter, D. Skinner, G. Ceder, and K. A. Persson. Commentary: The Materials Project: A materials genome approach to accelerating materials innovation. *APL Materials*, **1**: 011002, 2013.

[16] C. M. Breneman, L. C. Brinson, L. S. Schadler, B. Natarajan, M. Krein, K. Wu, L. Morkowchuk, Y. Li, H. Deng, and H. Xu. Stalking the Materials Genome: A Data-Driven Approach to the Virtual Design of Nanostructured Polymers. *Advanced Functional Materials*, **23**: 5746–5752, 2013.

[17] E. M. Campo. Materials Genome Initiative aims to expedite development, commercialization of advanced materials. *SPIE Professional*, **July**: 14–15, 2016.

Chapter 2

Carbon nanotubes and polymer nanocomposites

2.1 Carbon Nanotubes

Carbon nanotubes (CNTs) were first observed through TEM in 1952 by Russian scientists Radushkevich and Lukyanovich,[1] but it was through Iijima's 1991 publication "Helical microtubules of graphitic carbon," where he reported growth of CNTs via arc-discharge evaporation,[2] that CNTs gained an enormous research interest.

CNTs are cylindrical structures of hexagonal sp^2 carbon atoms, sometimes described as rolled up sheets of graphene (Figure 2.1a), with extremely high aspect ratios: diameters in the nanometres and lengths typically in the micrometres—although lengths of around 2 mm have been achieved.[3,4] Depending on the synthesis method, two types of CNTs can be fabricated, which exhibit different properties: single-walled CNTs (SWCNTs), composed of a single graphitic layer, and multi-walled CNTs (MWCNTs), consisting of several concentric layers held together through van der Waals forces (Figure 2.1b).[3]

Owing to the almost perfect sp^2 carbon structure, CNTs possess extremely appealing mechanical properties, with reported values for Young's modulus $\sim$1 TPa and tensile strength as high as 95 GPa.[5,6] Additionally, remarkable transport properties (electrical and thermal conductivities of 10^2–10^6 S/cm and 2000–6000 W/mK)[5] are afforded by CNTs' delocalised π system (Figure 2.1c). The chirality—that is, the 'rolling angle' of the graphene sheet

[1] L. V. Radushkevich and V. M. Lukyanovich. *Zurn Fisic Chim*, **26**: 88–95, 1952.

[2] S. Iijima. *Nature*, **357**: 56–58, 1991.

[3] R. Saito, G. Dresselhaus, and M. S. Dresselhaus. *Physical properties of carbon nanotubes*. vol. 35 World Scientific, 1998.

[4] Z. W. Pan et al. *Nature*, **394**: 631–632, 1998.

[5] P.-C. Ma et al. *Compos. Part A*, **41**: 1345–1367, 2010.

[6] M.-F. Yu et al. *Science*, **287**: 637–640, 2000.

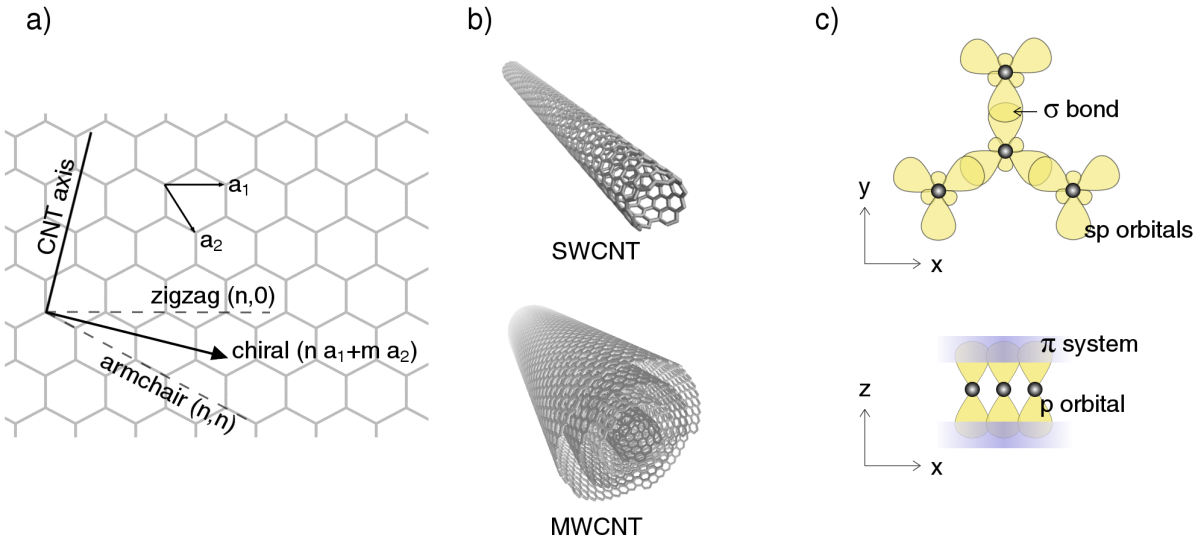

Figure 2.1: a) CNTs can be visualised as rolled up sheets of graphene. The chirality refers to the rolling angle, defined by the two unit vectors a_1 and a_2. b) A single-walled carbon nanotube (SWCNT) and a multi-walled carbon nanotube (MWCNT), consisting of concentric nanotubes. c) sp^2 structure of Carbon atoms in graphene form σ bonds on the plane (xy) through the head-on overlap of sp orbitals, and a π system through the side-on overlap of p_z orbitals (xz plane).

if a CNT were cut and layed flat (Figure 2.1a)—in SWCNTs is particularly interesting to the electronics community since it has crucial consequences on the electronic properties, producing semiconducting or metallic particles, by varying the band gap from 0 to 2.2 eV.[7] In contrast, MWCNTs are always metallic.

2.1.1 CNT synthesis

Several techniques exist for synthesising nanotubes, each producing CNTs of varying purity and quality; the most common are arc discharge, laser ablation and chemical vapour deposition. The method resulting in CNTs with least amount of structural defects is arc discharge;[8] this technique was originally used to produce fullerenes until Iijma observed growth of CNTs.[2] Arc discharge is a high-temperature (>1700 °C) technique where a DC arc voltage is applied between two graphite electrodes submerged in an inert gas. The product is a mixture of components, with fullerenes deposited inside the chamber as soot, and MWCNTs (or SWCNTs when the anode contains a metal catalyst) are deposited on the

[7] G. R. Ahmed Jamal, M. Shamsul Arefin, and S. M. Mominuzzaman. "Empirical prediction of bandgap in semiconducting single-wall carbon nanotubes" in: *Electrical & Computer Engineering (ICECE), 2012 7th International Conference on*. IEEE 2012. 221–224

[8] J. Prasek et al. *J. Mater. Chem.*, **21**: 15872–15884, 2011.

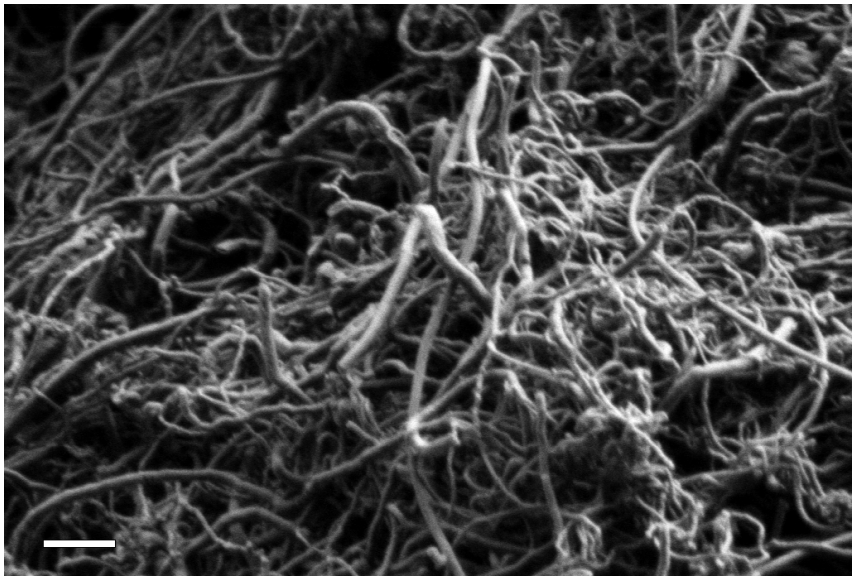

Figure 2.2: Highly tangled and agglomerated CVD-grown MWCNTs seen in SEM. Bar is 500 nm.

cathode.

Laser ablation is a method for the synthesis of high-quality and high-purity MWCNTs, first used in 1995 by Richard Smalley and coworkers.[9] Inside a 1200 °C furnace, Carbon from a graphite target is vaporised by a high power laser, resulting in CNTs deposited in a typically water-cooled Copper collector.[8] Similar to the arc-discharge technique, the use of metal catalysts added to the graphite target produces SWCNTs. Although both these techniques produce high-quality CNTs, they suffer from poor scalability.

Large-scale production of CNTs can be achieved through chemical vapour deposition (CVD) growth (Figure 2.2).[8] In this technique, a substrate with surficial metal catalysts is heated to 700 °C, while a carbon-containing gas flows inside a reaction chamber. The gas is decomposed and actuated through either thermal of plasma methods, and Carbon atoms arrange into CNTs at the catalyst sites. The type of CNT, as well as diameters, depends on the catalyst particles.[10] Studies have also demonstrated CVD growth of uniform vertically aligned CNTs through regularly patterned catalysts on the growth substrate,[11] as well as using nanoporous anodized aluminium oxide as template for CNT growth.[12]

[9] T. Guo et al. *Chem. Phys. Lett.*, **243**: 49–54, 1995.
[10] M. L. Terranova, V. Sessa, and M. Rossi. *Chem. Vap. Deposition*, **12**: 315–325, 2006.
[11] D. Kim et al. *Thin Solid Films*, **516**: 706–709, 2008.
[12] M. J. Kim et al. *Thin Solid Films*, **435**: 312–317, 2003.

2.1.2 Applications

With their unique properties, CNTs have been considered prime materials for myriad applications, from mechanical reinforcement to artificial muscles. This section provides a brief review of state-of-the-art CNT applications.

Electronic applications

As mentioned earlier, the electronic properties of CNTs depend considerably on the chirality. The possibility of producing both metallic and semiconducting SWCNTs with ballistic transport properties garnered interest in CNT-based transistors. The IBM group first developed field-effect transistors using individual SWCNTs fabricated through laser ablation.[13] Fabricated in a back-gate configuration using Pt source and drain electrodes patterned on a SiO_2 layer and CNT channel transferred onto the electrodes, it was shown that a gate voltage, externally applied on the doped silicon substrate beneath the oxide layer, could modulate the conductance of the p-type device by more than 5 orders of magnitude, similar behaviour to MOSFETs.[14] Later, n-type CNT FETs were also fabricated and characterised, assembled in a top gate structure.[15] Further research transitioned from single devices to logic circuits operating as inverters, NOR gates, static RAM cells, and AC ring oscillators.[16]

Paving the way for large-scale fabrication, Javey and coworkers developed self-aligned gate structures for CNT FETs, preventing gaps and overlaps between source, drain and gate electrodes.[17] The technique was recently developed into wrap-gate geometries i.e. gate uniformly wrapping CNT channel, to produce both p-type and n-type CNT FETs (by using Al_2O_3 and HfO_2 gate dielectrics respectively), ideal for CMOS technology.[18]

In parallel with CNT for CMOS research, promising advances have been made in CNT FETs for pass-transistor logic (PTL). Unlike CMOS, where signals are only added to the gate, signals in PTL can be added to any terminal of FETs, making the technology significantly more efficient than CMOS. PTL is difficult to achieve with Si technology, as a zero threshold voltage is needed—this can be attained with CNTs.[19] A one-bit full subtractor and full adder were designed and characterised using three pairs of n-type and p-type FETs fabri-

[13] R. Martel et al. *Appl. Phys. Lett.*, **73**: 2447–2449, 1998.

[14] M. Endo, M. S. Strano, and P. M. Ajayan. "Potential applications of carbon nanotubes" in: *Carbon nanotubes*. Springer, 2007. 13–62

[15] S. J. Wind et al. *Appl. Phys. Lett.*, **80**: 3817–3819, 2002.

[16] A. Bachtold et al. *Science*, **294**: 1317–1320, 2001.

[17] A. Javey et al. *Nano Lett.*, **4**: 1319–1322, 2004.

[18] A. D. Franklin et al. *Nano Lett.*, **13**: 2490–2495, 2013.

[19] L.-M. Peng, Z. Zhang, and S. Wang. *Mater. Today*, **17**: 433–442, 2014.

cated on individual CNTs;[20,21] using CMOS technology, this would require 28 FETs for each combinatorial circuit.

Energy Applications

The high electrical conductivity and chemical stability of CNTs makes them interesting materials for electrochemical systems such as Lithium-ion batteries, solar cells, supercapacitors, and others.[14]

In Lithium-ion batteries, CNTs can find application as either electrodes (reversible capacity of up to 1 Ahg^{-1} has been measured),[22] or as anode filler material.[23] With the drive for flexible electronics, CNTs may solve the challenge of flexible batteries. Indeed, ultraflexible Li-ion batteries were recently assembled using CNT electrodes modified into cones through elastocapillary aggregation, with performances surpassing that of traditional Fe_2O_3 electrode batteries.[24]

Another route towards energy storage is that of supercapacitors, and CNTs have attracted interest in the field after the observed energy density increase in CNT-electrode supercapacitors.[25] Energy densities of 110.6 Wh kg^{-1} were recently recorded for supercapacitor building blocks based on CNT-graphene flexible structures which allow rapid ion diffusion.[26]

CNTs have been researched also as materials for organic solar cell bulk heterojuntions to form a percolating network of electron acceptors within a conjugated polymer. High aspect ratios allow percolation at low CNT concentrations.[14] In 2002, an increase of two orders of magnitude in short-circuit current was demonstrated in SWCNT-poly(3-octylthiophene) (P3OT) versus pristine P3OT.[27] Improvements in performance were then reported through use of different conjugated polymers, and through functionalisation of CNTs with dyes with increased absorption within the solar spectrum.[28] CNTs have also been used as hole collectors in perovskite solar cells, with efficiencies up to 5.28%.[29]

[20] L. Ding et al. *ACS Nano*, **6**: 4013–4019, 2012.
[21] L. Ding et al. *Nat. Commun.*, **3**: 677, 2012.
[22] B. Gao et al. *Chem. Phys. Lett.*, **307**: 153–157, 1999.
[23] M. Endo et al. *Carbon*, **38**: 183–197, 2000.
[24] S. Ahmad et al. *Adv. Mater.*, **28**: 6705–6710, 2016.
[25] C. Niu et al. *Appl. Phys. Lett.*, **70**: 1480–1482, 1997.
[26] D. T. Pham et al. *ACS Nano*, **9**: 2018–2027, 2015.
[27] E. Kymakis, I. Alexandrou, and G. A. J. Amaratunga. *J. Appl. Phys.*, **93**: 1764–1768, 2003.
[28] S. Bhattacharyya, E. Kymakis, and G. A. J. Amaratunga. *Chem. Mater.*, **16**: 4819–4823, 2004.
[29] Z. Li et al. *Nanoscale*, **8**: 6352–6360, 2016.

Sensors

Carbon nanotubes for sensing applications is a large area of research. For gas sensing, important for environmental purposes and chemical safety, the presence of defects in CNTs is useful as they are likely binding sites for gas molecules.[30] The conductance of a semiconducting SWCNT gas sensor in a FET configuration was reported to vary by three orders of magnitude with exposure to NO_2 and NH_3 gas within seconds.[31] This effect is likely caused by the charge transfer between the gas molecules and SWCNTs.[32] Charge transfer with specific gases can be achieved by CNT functionalisation.[33]

CNTs have also been developed as biosensors to detect glucose,[34] proteins,[35] and DNA hybridisation.[36] Many of these devices exploit the photoluminescence of CNTs, which is more advantageous than traditional fluorophores for biomedical applications.[14] Good operation was reported for such sensors injected into living cells.[14]

Strain sensors is another application for CNTs, particularly for MEMS devices. It was found that small strain levels generated variations in resistivity of vertically aligned CNTs.[14,37] Recently, a strain sensor based on SWCNT inside a polymeric matrix was fabricated, with reported high stability and sensitivity—enough to detect emotional expressions and eye movements when placed on the face.[38]

Biological and medical applications

There are two big areas of research of CNTs for medical applications: drug delivery, and targeted imaging/labelling of live cells and tissues. Although early comparisons to asbestos generated concerns into the cytotoxicity of CNTs,[39,40] it is now understood that biological compatibility depends on CNT functionalisation.[41,42]

Through non-covalent functionalisation, CNTs can be loaded with drugs, fluorophore, proteins and DNA for *in vivo* delivery.[43] The main challenges now are drug release, and CNT

[30] M. Mittal and A. Kumar. *Sens. Actuators. B*, **203**: 349–362, 2014.
[31] J. Kong et al. *Science*, **287**: 622–625, 2000.
[32] A. Goldoni et al. *J. Am. Chem. Soc.*, **125**: 11329–11333, 2003.
[33] S. Mao, G. Lu, and J. Chen. *J. Mater. Chem. A*, **2**: 5573–5579, 2014.
[34] K. Besteman et al. , **3**: 727–730, 2003.
[35] R. J. Chen et al. *Proc. Natl. Acad. Sci. U.S.A.*, **100**: 4984–4989, 2003.
[36] A. Star et al. *Proc. Natl. Acad. Sci. U.S.A.*, **103**: 921–926, 2006.
[37] S. Vemuru et al. *J. Strain Anal. Eng. Des.*, **44**: 555–562, 2009.
[38] E. Roh et al. *ACS Nano*, **9**: 6252–6261, 2015.
[39] B. Liu, E. M. Campo, and T. Bossing. *PLOS ONE*, **9**: e88681, 2014.
[40] Y. Sato et al. *Mol. Biosyst.*, **1**: 176–182, 2005.
[41] H. Dumortier et al. *Nano Lett.*, **6**: 1522–1528, 2006.
[42] S. Marchesan et al. *Mater. Today*, **18**: 12–19, 2015.
[43] Z. Liu et al. *Nano Res.*, **2**: 85–120, 2009.

clearance.[44] Biocompatible and water-stable MWCNT functionalised with the copolymer poly(*p*-phenyle)-*g*-poly(ethylene glycol) and an estrogen-specific antibody were used to image estrogen receptors in cancer cells through fluorescence microscopy.[45] More recently, a magnetic nanoprobe comprising SWCNTs, gold nanoparticles, superparamagnetic iron oxide nanoparticles and quantum dots was constructed for enhanced Raman scattering imaging and magnetic guidance of live cells.[46]

2.2 Polymer nanocomposites

The three biggest challenges in the fabrication of polymer CNT composites are achieving CNT dispersion, CNT alignment, and a strong interfacial interaction between CNT and polymer. This section firstly describes commonly used techniques to achieve these goals; these techniques need thorough consideration, as they ultimately condition interactions within the system, and therefore the final system properties. The chapter concludes with recent examples of polymer nanocomposites from the literature, fabricated either for enhanced structural properties or for functional behaviour.

2.2.1 Dispersion strategies

Dispersion of CNTs is arguably the biggest challenge in nanocomposite fabrication, as well as for other applications.[5] Indeed, due to their large surface area, CNTs agglomerate into bundles (Fig. 2.2) consisting of up to a few hundred individual nanotubes held by van der Waals forces, which has detrimental consequences on resulting properties.[5,47] In nanocomposites, good dispersion is vital in producing homogeneous system, as well as achieving the most effective CNT-polymer interactions.[48] This section gives an overview of the most commonly employed dispersion solutions, highlighting the advantages and downfalls of each method.

Ultrasonication

This technique—the most widely employed for nanoparticle dispersion[5]—achieves dispersion by applying ultrasonic energy through an ultrasonic probe or *sonicator* which breaks apart CNT bundles into individual tubes. This occurs due to the enormous shear rates (up to $\sim 10^9$ s^{-1}) and extreme local temperatures (up to 15000 K) upon cavitation, the event arising when

[44] V. Biju. *Chem. Soc. Rev.*, **43**: 744–764, 2014.
[45] M. Yuksel et al. *Biomacromolecules*, **13**: 2680–2691, 2012.
[46] H. Wang et al. *Talanta*, **119**: 144–150, 2014.
[47] J. N. Coleman, U. Khan, and Y. K. Gun'ko. *Adv. Mater.*, **18**: 689–706, 2006.
[48] X.-L. Xie, Y.-W. Mai, and X.-P. Zhou. *Mater. Sci. Eng. R*, **49**: 89–112, 2005.

an acoustic compression wave exceeds a threshold energy density.[49] Sonication requires CNTs to be suspended in a low-viscosity solvent, such as water, ethanol or toluene. It is possible to sonicate CNTs directly with the polymer, but this requires an extra process to reduce the viscosity of the polymer beforehand. For this reason, incorporation into polymer matrix typically occurs after sonication.

Although sonication is very effective for CNT dispersion, the cavitation process can severely damage the nanoparticles, which—just like CNT agglomerates—have detrimental effects on properties. This has been widely observed,[50–53] yet it is currently not clear what are 'safe' sonication conditions that will avoid this damage. In the literature, power (including oscillation amplitude and duty cycle) and exposure time are the sonication parameters typically reported, but these are not enough to standardise sonication experiments: the acoustic energy injected into the nanoparticle dispersion also depends on sonicated volume, tip immersion, suspension viscosity (which combines properties of solvent and nanoparticles), among others.[54] In fact, Huang and coworkers reported a sonication model that predicts that CNTs always experience damage as long as cavitation occurs, and become progressively shorter until they reach a limiting length determined by nanoparticle diameter d and tensile strength σ^*, given approximately as $L_{lim} \approx 7 \times 10^{-}4d\sqrt{\sigma^*}$.[49]

Calendering

A calender, the apparatus used for the calendering process, principally consists of three rollers (the method is often referred to as the *three roll mills* method) which rotate at different velocities. A viscous material is fed between the first and second rollers, which rotate in opposing directions and produce intense shear mixing. The material then flows beneath the second roller and above the third, where it is collected. The mismatch in angular velocities and small gaps between the rollers result in enormous shear forces which can disperse and homogenise the material very effectively in a short time.[55] The short exposure time makes calendering an attractive alternative to sonication for CNT dispersion, since it is less likely to result in nanoparticle damage. Additionally, controllable size distribution of particles can be achieved by adjusting the gap between the rollers.[5]

The main concern with this technique as a CNT dispersion solution is that while the mini-

[49] Y. Y. Huang, T. P. J. Knowles, and E. M. Terentjev. *Adv. Mater.*, **21**: 3945–3948, 2009.
[50] K. L. Lu et al. *Carbon*, **34**: 814–816, 1996.
[51] J. Y. Huang, F. Ding, and B. I. Yakobson. *Phys. Rev. Lett.*, **100**: 035503, 2008.
[52] M. D. Rossell et al. *Carbon*, **61**: 404–411, 2013.
[53] A. Lucas et al. *J. Phys. Chem. C*, **113**: 20599–20605, 2009.
[54] J. S. Taurozzi, V. A. Hackley, and M. R. Wiesner. *NIST Special Publication*, **1200-2**: 1–15, 2012.
[55] J. H. Park et al. *Compos. Sci. Technol.*, **68**: 753–759, 2008.

mum gap between rollers is a few microns, comparable to lengths of CNTs, this is considerably bigger than CNT diameters. Consequently, although good dispersion using calendering has been achieved,[56,57] CNT bundles may not be broken down into individual nanotubes. Another complication arises from the need for a viscous initial material mixture: the technique cannot be applied therefore to CNTs embedded into thermoplastic polymers. This can be solved by mixing nanoparticles with the monomers, followed by *in situ* polymerisation.

Ball milling

In ball milling, materials are ground into very fine powder through impact and attrition of balls, which could be ceramic, flint pebbles, rubber, stainless steel, etc.[5] The technique is mostly used for grinding coal, pigments and ceramic, but has been applied to CNTs.[58,59]

Ball milling necessarily causes particle damage, but the appeal arises from the functionalisation of CNTs—as well as enhancement in dispersibility—which can aid bonding to polymers and impact electronic properties to suit application.[5,60]

Stir and extrusion

A good dispersion of MWCNTs within an epoxy polymer was obtained by intensive stirring (2000 rpm for 1 h), after initial dispersion of loosely bundled nanotubes in an ultrasonic bath.[61] MWCNTs dispersed in such a manner tend to rebundle, however, even after polymer curing.[62] Even more intense stirring (speeds of up to 10000 rpm) is required to disperse severely tangled MWCNTs.[5] Further, SWCNTs do not easily disperse through stirring.[5] Despite these limitations, the technique causes no damage to CNTs.

Extrusion relies on high shear flow created by rotating screws, and is a useful technique for CNT dispersion in thermoplastics. The technique does not break CNT bundles, however, producing a good dispersion of agglomerated nanotubes within the thermoplastic. For this reason, extrusion is used for composites with high CNT content.[63]

[56] F. H. Gojny et al. *Compos. Sci. Technol.*, **64**: 2363–2371, 2004.
[57] E. T. Thostenson and T.-W. Chou. *Carbon*, **44**: 3022–3029, 2006.
[58] J. Y. Huang, H. Yasuda, and H. Mori. *Chem. Phys. Lett.*, **303**: 130–134, 1999.
[59] Y. A. Kim et al. *Chem. Phys. Lett.*, **355**: 279–284, 2002.
[60] P. C. Ma, B. Z. Tang, and J.-K. Kim. *Chem. Phys. Lett.*, **458**: 166–169, 2008.
[61] J. Sandler et al. *Polymer*, **40**: 5967–5971, 1999.
[62] J. Li et al. *Adv. Funct. Mater.*, **17**: 3207–3215, 2007.
[63] T. Villmow et al. *Polymer*, **49**: 3500–3509, 2008.

2.2.2 Alignment solutions

The second important challenge in nanocomposite fabrication, after dispersion, is filler alignment. This factor has a key influence over composite mechanical and functional properties.[48] Fine tuning of properties therefore requires controllable alignment methods. This section outlines current alignment strategies.

Ex situ techniques

This group of techniques relate to the alignment of CNTs prior to embedding or polymerisation, usually upon growth.[48] Early success was reported by de Heer and coworkers, who produced sheets of highly aligned CNTs by drawing suspensions of arc discharge-grown 1–5 μm-long MWCNT through a ceramic filter with 0.2 μm-pores, followed by transfer onto a plastic substrate.[64] The most common route for achieving growth of aligned CNTs is through CVD growth on a substrate with patterned growth catalysts acting as a template.[48] Recently, e-beam evaporation was used to pattern iron catalyst rings to produce CNT forests through CVD growth, perpendicularly aligned to the silicon substrate.[24] Yet another method is through pulsed plasma enhanced CVD growth, which can result in highly aligned CNTs synthesised at low temperatures (400–450 °C).[65]

Force field techniques

Aligned CNT arrays were produce by Ajayan and coworkers simply by cutting thin slices of 50–200 nm width from a nanocomposite made by randomly dispersing MWCNTs in a liquid epoxy.[66] They found, however, that alignment of CNTs decreased with increasing slice width. Vigolo et al were able to produce ribbons of aligned PVA|CNT fibres of up to one metre in length by injecting a SWCNT dispersion into the polymer solution.[67] In this scheme, the shear forces at the tip of the syringe needle induced the alignment which was maintained by the viscous polymer.

The most common force field technique for alignment of CNTs within polymeric matrices is by uniaxial stretching.[68–71] Indeed, Ahir and coworkers found that CNT alignment could

[64] W. A. de Heer et al. *Science*, **268**: 845–847, 1995.
[65] M. Baro and A. R. Pal. *Plasma Chem. Plasma P.*, **35**: 247–257, 2015.
[66] P. M. Ajayan et al. *Science*, 1212–1212, 1994.
[67] B. Vigolo et al. *Science*, **290**: 1331–1334, 2000.
[68] L. Jin, C. Bower, and O. Zhou. *Appl. Phys. Lett.*, **73**: 1197–1199, 1998.
[69] K. Czaniková et al. *J. Nanophotonics*, **6**: 810707, 2011.
[70] S. Courty et al. *EPL*, **64**: 654, 2003.
[71] E. T. Thostenson and T.-W. Chou. *J. Phys. D*, **35**: L77, 2002.

be controlled by the extent of uniaxial strain.[72] Clearly, a further advantage is the simplicity of the technique. As of yet, there has not been substantial work reported on the significance of strain *rate*, needed to standardise the technique.

Magnetic field techniques

Magnetic fields were also exploited to achieve CNT alignment, firstly used by Kimura and coworkers, who applied a 10 T magnetic field to a dispersion of MWCNTs in unsaturated polyester and produced composites with anisotropic alignment.[73] Compared to epoxy|CNT composites synthesised in the absence of a magnetic field, Choi and coworkers reported an increase in thermal properties by 10% and in electrical properties by 35% along the field alignment direction.[74]

Electrospinning

Electrospinning is a fibre fabrication technique, where a continuous yarn is drawn from a syringe to a collector by the high voltage generated between between them (Figure 2.3).[75,76] The resulting fibres are mostly reported to be aligned, but using an additional electric field, alignment of the polymer *chains* has been achieved.[77,78] CNT polymer nanocomposites have also been fabricated using electrospinning, with some level of CNT alignment reported.[79–82]

Many polymeric systems have been successfully electrospun,[83] but understanding of how solution parameters and process variables influence the technique is limited; for instance, electrospinning of poly(ethylene oxide) requires solution viscosities (controlled by altering polymer concentration) of 1–20 poise,[84] while viscosities of 1.02–10.2 poise are required to electrospin cellulose acetate.[85] Finding parameters which will render a polymeric system electrospinnable usually requires tedious trial and error.[86]

[72] S. V. Ahir et al. *Phys. Rev. B*, **73**: 085420, 2006.
[73] T. Kimura et al. *Adv. Mater.*, **14**: 1380–1383, 2002.
[74] E. S. Choi et al. *J. Appl. Phys.*, **94**: 6034–6039, 2003.
[75] N. J. Pinto et al. *Appl. Phys. Lett.*, **83**: 4244–4246, 2003.
[76] M. Li et al. *Biomaterials*, **27**: 2705–2715, 2006.
[77] M. V. Kakade et al. *J .Am. Chem. Soc.*, **129**: 2777–2782, 2007.
[78] N. Kimura et al. *Macromol. Mater. Eng.*, **295**: 1090–1096, 2010.
[79] Y. Y. S. Huang et al. *Nanotechnology*, **23**: 105305, 2012.
[80] Y. Dror et al. *Langmuir*, **19**: 7012–7020, 2003.
[81] F. Ko et al. *Adv. Mater.*, **15**: 1161–1165, 2003.
[82] R. Sen et al. *Nano Lett.*, **4**: 459–464, 2004.
[83] Z.-M. Huang et al. *Comp. Sci. Technol.*, **63**: 2223–2253, 2003.
[84] H. Fong, I. Chun, and D. H. Reneker. *Polymer*, **40**: 4585–4592, 1999.
[85] H. Liu and Y.-L. Hsieh. *J. Polym. Sci. Part B*, **40**: 2119–2129, 2002.
[86] J. Sidaravicius et al. *J. Appl. Polym. Sci.*, **131**: , 2014.

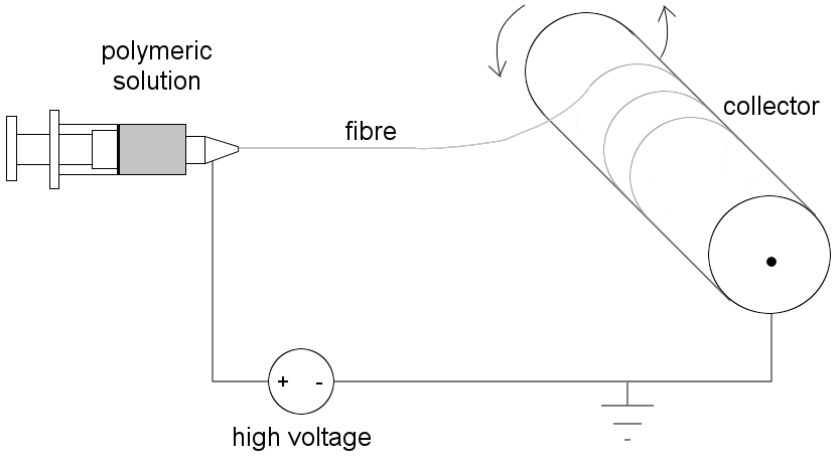

Figure 2.3: Experimental setup for electrospinning using a rotating drum collector.

2.2.3 CNT functionalisation

Functionalisation of CNTs refers to the incorporation of other molecules or chemical groups to the nanotubes with the aim of altering their individual properties or the properties of the final composite system. These can include amongst others tailoring of optical properties, facilitating dispersion within solvents or polymers, or enhancing the CNT-polymer interaction to increase load transfer.[69,87]

On the processing end, functionalisation can be categorised as covalent (or chemical) or non-covalent (or physical), each with very different results.[5] As pristine CNTs are chemically stable, covalent functionalisation involves defect sites, such as carbon vacancies or 'holes' lined with carboxyl groups, sp^3 hybridisation defects, or indeed the nanotube termini whose curvatures make them more reactive compared to sidewalls.[88] Though initial defects arise from growth, sp^3 sites are also induced precisely for covalent functionalisation. A common route for this is flourination of CNTs, which leaves C–F bonds throughout the sidewalls. These bonds are then used as substitution sites for further functionalisation e.g. with amino, alkyl and hydroxyl groups.[5,89,90] Covalent functionalisation produces very strong bonds, but has the disadvantage of perturbing the pristine CNT structure, including local deconjugation of π system which is responsible for many unique properties of nanotubes.[5]

Conversely, non-covalent functionalisation typically relies on the pristine π system to form interactions based on electrostatics, van der Waals forces, hydrophobic–hydrophillic

[87] P. L. Dickrell et al. *Tribol. Lett.*, **24**: 85–90, 2006.
[88] S. Banerjee, T. Hemraj-Benny, and S. S. Wong. *Adv. Mater.*, **17**: 17–29, 2005.
[89] J. L. Stevens et al. *Nano Lett.*, **3**: 331–336, 2003.
[90] Q.-H. Zhang and D.-J. Chen. *J. Mater. Sci.*, **39**: 1751–1757, 2004.

effects, and π effects.[91] The main interest of this form of functionalisation is that the physical properties of CNTs are not compromised.[92] Examples of non-covalent interactions are π–π interactions or π–π stacking, formed by two aromatic groups,[93] CH–π interactions involving a π system and a –CH bond,[94] lone pair (LP)–π interactions e.g. between water and CNTs,[95] and even Hydrogen bonding.[96] Compared to covalent bonding, these interactions are considerably weaker. A direct advantage of this is that interactions can be controlled and even reversed.[97,98]

To mention a few examples of non-covalent CNT functionalisation, Lee and coworkers addressed the insolubility of CNTs—which hinders solution-based CNT processes—by sonicating nanotubes with oligothiophene-terminated poly(ethylene glycol) (TN-PEG) molecules.[99] TN-PEG molecules were strongly adsorbed to CNT sidewalls through π–π interactions, and achieved considerably better solubility in water than commercial surfactants. Another approach to enhance solubility is functionalisation by polymer wrapping. Indeed, Baskaran and coworkers observed a high stability dispersion after functionalising MWCNTs with a wide range of commercial polymers, also concluding that polymer wrapping through CH–π interactions is a general phenomenon between CNTs and polymers.[100] Specific polymers were also found to enhance properties of CNTs: Curran et al reported an improvement in electrical properties of poly(p-phenylenevinylene-co-2,5-dioctyloxy-m-phenylenevinylene)|SWCNT complexes compared to the individual constituents.[101]

2.2.4 State-of-the-art polymer nanocomposites

This section reviews some of the advances made in the field of polymer nanocomposites and is split into two halves. The first half deals with polymer nanocomposites fabricated to improve the structural properties of the bulk materials, such as electrical, thermal and mechanical properties. The second half reviews those composites fabricated with the aim of introducing or enhancing functional properties, such as actuating and sensing properties.

[91] E. V. Anslyn and D. A. Dougherty. *Modern physical organic chemistry*. University Science Books, 2006.
[92] N. G. Sahoo et al. *Prog. Polym. Sci.*, **35**: 837–867, 2010.
[93] C. A. Hunter and J. K. M. Sanders. *J. Am. Chem. Soc.*, **112**: 5525–5534, 1990.
[94] M. Nishio, M. Hirota, and Y. Umezawa. *The CH/π interaction: evidence, nature, and consequences*. vol. 21 John Wiley & Sons, 1998.
[95] J. Ran and P. Hobza. *J. Chem. Theory Comput.*, **5**: 1180–1185, 2009.
[96] J. Robertson. *Mater. Today*, **7**: 46–52, 2004.
[97] S. L. Teh, D. Linton, and M. D. Dadmun. *Macromolecules*, **44**: 7737–7745, 2011.
[98] F. Ilhan, M. Gray, and V. M. Rotello. *Macromolecules*, **34**: 2597–2601, 2001.
[99] J. U. Lee et al. *Carbon*, **45**: 1051–1057, 2007.
[100] D. Baskaran, J. W. Mays, and M. S. Bratcher. *Chem. Mater.*, **17**: 3389–3397, 2005.
[101] S. A. Curran et al. *Adv. Mater.*, **10**: 1091–1093, 1998.

Structural composites

A promising class of polymer systems for the fields of tissue-engineering, drug-delivery, and even sensors and actuators is that of hydrogels. Possibly the biggest hinderance to application is the poor mechanical properties of these materials. Li and coworkers addressed this limitation through MWCNT incorporation.[102] Covalent CNT functionalisation with poly(acrylic acid) (PAA) both facilitated dispersion within the hydrogel and provided stronger interactions. Mechanical tests found an increase in tensile strength and strain of up to 3.9 and 3.2 times respectively when 1.4 wt% MWCNT-PAA was introduced to a polyacrylamide (PAM) matrix, compared to the pure PAM hydrogel. Moreover, they noted that the improvement in mechanical properties was dependent on the MWCNT content.[102]

The remarkable thermal conductivity of CNTs ($\sim$3000 $Wm^{-1}K^{-1}$), combined with the light weight and low cost of polymers, have led to considerable efforts undertaken towards synthesis of thermally conductive polymer nanocomposites, which would overcome associated limitations regarding reliability and functionality.[103] The principal obstacle in this field is the poor thermal conductivity of polymeric matrices, which typically lie within the 0.2–0.5 $Wm^{-1}K^{-1}$ range.[104] Two main criteria govern the thermal conductivity of polymer nanocomposites: CNT dispersion, and CNT-polymer interactions at the interface.[103] Zhang and coworkers achieved a high thermal conductivity in poly(vinylidene fluoride) (PVDF)|MWCNT composites by first non-covalently functionalising CNTs with polyvinylpyrrolidone (PVP), which wrapped around CNTs through CH–π interactions—predicted by Baskaran et al,[100] and observed through TEM.[104] This CNT modification allowed an efficient dispersion within the PVDF matrix, which created a denser CNT network structure characterised by SEM, and provided a 'soft' interface (decreased Young's modulus mismatch) between PVDF and PVP through hydrogen bonding, expected to minimise the thermal resistance, and, in turn, maximise the thermal conductivity. Indeed, they reported a gradual increase in thermal conductivity with increasing CNT (functionalised and pristine) content, with functionalised CNT filler resulting in the highest conductivity. Under optimal CNT and PVP content, composites exhibited thermal conductivities of 0.63 $WM^{-1}m^{-1}$, compared with 0.2 $WM^{-1}m^{-1}$ of pristine PVDF.[104] Similarly, Kim and coworkers reported an increasing thermal conductivity in polycarbonate (PC)|MWCNT composites with increasing CNT content. Additionally, it was observed that the length of CNTs also impacts the thermal conductivity, with higher conductivities achieved by longer CNTs.[105] These are promising findings for the tailoring of

[102] Z. Li et al. *Polymer*, **85**: 67–76, 2016.
[103] Z. Han and A. Fina. *Prog. Polym. Sci.*, **36**: 914–944, 2011.
[104] W.-B. Zhang et al. *Compos. Sci. Technol.*, **106**: 1–8, 2015.
[105] H. S. Kim et al. *Compos. Part B*, **79**: 505–512, 2015.

thermal properties in polymer nanocomposites.

Another field where polymer nanocomposites are considered promising systems is electromagnetic interference (EMI) shielding.[106–108] These systems rely on the well established correlation between EMI shielding effectiveness (SE) and electrical conductivity.[109] Indeed, a conductive network is formed when CNT content exceeds the percolation threshold within a polymer, which can strongly interact with EM waves. For many electronic applications, however, EMI shielding materials need to be electrically insulated; this is usually achieved by covering the EMI shield with high-resistance materials. Hayashida and coworkers investigated the SE and electrical conductivity of poly(methyl methacrylate) (PMMA)-grafted MWCNTs embedded in a PMMA matrix.[110] Covalent functionalisation of MWCNTs rendered them electrically-isolated, preventing percolation even at high CNT contents; this produced a composite with a volume resistivity as high as $1.3 \times 10^{15}\Omega$ cm, 14 orders of magnitude higher than PMMA|unfunctionalised MWCNTs. The composites transmitted EM waves in the 0.001–1 GHz frequency range, but produced good EMI shielding at high frequencies (30–300 GHz), showing that it is not the electrical conductivity of the bulk system, but that of the individual CNTs which induces EMI shielding.[110]

Functional composites

One of the more intriguing phenomenon often observed in CNT|polymer composites is actuation—the mechanical output upon external stimuli excitation. Research efforts have been undertaken to enhance the actuation behaviour of certain polymeric matrices through the presence of CNTs;[111,112] more innovative studies report on the actuating behaviour of composite systems which is absent in the individual constituents.[70,113] There have been numerous reports of this behaviour, but the community has not agreed on the underlying mechanism: this is preventing full exploitation of these so-called 'smart' composites, which could find immediate application in a myriad of fields, from sensors and actuators, to artificial muscles and neuroscience.[114–117]

[106]H. M. Kim et al. *Appl. Phys. Lett.*, **84**: 589–591, 2004.
[107]Y. Yang et al. *Nano Lett.*, **5**: 2131–2134, 2005.
[108]N. Li et al. *Nano Lett.*, **6**: 1141–1145, 2006.
[109]M. Yang, V. Koutsos, and M. Zaiser. *J. Phys. Chem. B*, **109**: 10009–10014, 2005.
[110]K. Hayashida and Y. Matsuoka. *Carbon*, **85**: 363–371, 2015.
[111]B. J. Landi et al. *Nano Lett.*, **2**: 1329–1332, 2002.
[112]H. Koerner et al. *Nat. Mater.*, **3**: 115–120, 2004.
[113]S. V. Ahir and E. M. Terentjev. *Nat. Mater.*, **4**: 491–495, 2005.
[114]R. Vaia. *Nature Mater.*, **4**: 429–430, 2005.
[115]R. H. Baughman. *Synth. Mater.*, **78**: 339–353, 1996.
[116]R. H. Baughman et al. *Science*, **284**: 1340–1344, 1999.
[117]R. H. Baughman. *Science*, **308**: 63–65, 2005.

Courty and coworkers reported on a novel nematic elastomer|CNT electro-actuator which produced a reversible and reproducible uniaxial stress of ∼1 kPa when the composite was excited by a constant electric field of ∼1 MV/m.[70] They proposed that the field produced a high torque in the nanotubes, which were oriented along the nematic director, causing them to rotate towards the field direction; in turn, the polymeric network is dragged with the CNTs, producing the measured stress.

Groundbreaking work by Ahir and coworkers in 2005 demonstrated the reversible photomechanical actuation behaviour of polydimethylsiloxane (PDMS)|MWCNT composites, capable of producing $>$ 40 kPa uniaxial stress.[113,114] Remarkably, the direction and extent of mechanical output upon IR radiation was dependent on the applied uniaxial strain upon fabrication. The critical strain was found to be 10%: strains below this resulted in expansive response, and above this in compressive response. Varying strain levels were found through wide-angle X-ray diffraction to control CNT alignment. It was stipulated that the net length of CNTs would decrease as absorbed photons generated kink-instabilities—the magnitude and direction of mechanical output was then explained as the averaging of the individual CNT response as a function of alignment.[113]

Photomechanical actuation was then reported for ethylene-vinyl acetate (EVA)|MWCNT composites, this time using visible light to excite the system.[69] The composites, formed into Braille elements using a punch and die mould, responded through a reversible height change of up 15.2% when irradiated by a blue diode, and up to 9.7% when a red diode was used, representing stresses of up to 18 kPa. The reproducibility was tested for over 100 cycles. The behaviour was tentatively attributed to CNTs absorbing light, converting it to heat and transferring it to stretched polymeric chains which consequently contract. To aid dispersion within the polymeric matrix, CNTs were non-covalently functionalised with cholesteryl 1-pyrenecarboxylate (PyChol) dispersant through sonication which enabled π–π interactions between the pyrene groups in PyChol and CNT sidewalls. Uniaxial alignment of CNTs was induced by straining the composite by 50%, and confirmed by SEM.[118]

Polymer nanocomposites as sensors are rather more advanced than the systems above, due to a well understood operation mechanism: specific stimuli causes the polymeric matrix to swell, increasing the distance between adjacent nanotubes and therefore reducing the tunnelling current.[119] Fan et al produced vapour-sensing thermoplastic polyurethane (TPU) multifilament|MWCNT composites able to distinguish between benzene, toluene, THF, ethanol, acetone and methanol solvent vapours at low concentrations (down to 0.5%); absorption of each analyte induced a specific change in the composite's electrical resistance.[120]

[118]K. Czaniková et al. *Sens. Actuators B*, **186**: 701–710, 2013.
[119]T. Villmow et al. *Mater. Today*, **14**: 340–345, 2011.
[120]Q. Fan et al. *Sens. Actuators B*, **156**: 63–70, 2011.

So and coworkers developed a flexible pressure sensing PDMS|SWCNT composite. Due to the high elasticity of the matrix, the structural flexibility of the sensor was maintained after repeated compression.[121] Similar sensors have also been reported for detection of liquids,[119] chemicals,[122] force,[123] and strain.[124]

[121]H.-M. So et al. *Mater. Res. Bull.*, **48**: 5036–5039, 2013.
[122]L. Han, A. L. Andrady, and D. S. Ensor. *Sens. Actuators B*, **186**: 52–55, 2013.
[123]M. Vatani, E. D. Engeberg, and J.-W. Choi. *Sens. Actuators A*, **195**: 90–97, 2013.
[124]N. Hu et al. *Carbon*, **48**: 680–687, 2010.

Bibliography

[1] L. V. Radushkevich and V. M. Lukyanovich. O strukture ugleroda, obrazujucegosja pri termiceskom razlozenii okisi ugleroda na zeleznom kontakte. *Zurn Fisic Chim*, **26**: 88–95, 1952.

[2] S. Iijima. Helical microtubules of graphitic carbon. *Nature*, **357**: 56–58, 1991.

[3] R. Saito, G. Dresselhaus, and M. S. Dresselhaus. *Physical properties of carbon nanotubes*. vol. 35 World Scientific, 1998.

[4] Z. W. Pan, S. S. Xie, B. H. Chang, C. Y. Wang, L. Lu, W. Liu, W. Y. Zhou, W. Z. Li, and L. X. Qian. Very long carbon nanotubes. *Nature*, **394**: 631–632, 1998.

[5] P.-C. Ma, N. A. Siddiqui, G. Marom, and J.-K. Kim. Dispersion and functionalization of carbon nanotubes for polymer-based nanocomposites: a review. *Composites Part A: Applied Science and Manufacturing*, **41**: 1345–1367, 2010.

[6] M.-F. Yu, O. Lourie, M. J. Dyer, K. Moloni, T. F. Kelly, and R. S. Ruoff. Strength and breaking mechanism of multiwalled carbon nanotubes under tensile load. *Science*, **287**: 637–640, 2000.

[7] G. R. Ahmed Jamal, M. Shamsul Arefin, and S. M. Mominuzzaman. "Empirical prediction of bandgap in semiconducting single-wall carbon nanotubes" in: *Electrical & Computer Engineering (ICECE), 2012 7th International Conference on*. IEEE 2012. 221–224

[8] J. Prasek, J. Drbohlavova, J. Chomoucka, J. Hubalek, O. Jasek, V. Adam, and R. Kizek. Methods for carbon nanotubes synthesis—review. *Journal of Materials Chemistry*, **21**: 15872–15884, 2011.

[9] T. Guo, P. Nikolaev, A. Thess, D. T. Colbert, and R. E. Smalley. Catalytic growth of single-walled manotubes by laser vaporization. *Chemical Physics Letters*, **243**: 49–54, 1995.

[10] M. L. Terranova, V. Sessa, and M. Rossi. The world of carbon nanotubes: an overview of CVD growth methodologies. *Chemical Vapor Deposition*, **12**: 315–325, 2006.

[11] D. Kim, S. H. Lim, A. J. Guilley, C. S. Cojocaru, J. E. Bourée, L. Vila, J. H. Ryu, K. C. Park, and J. Jang. Growth of vertically aligned arrays of carbon nanotubes for high field emission. *Thin Solid Films*, **516**: 706–709, 2008.

[12] M. J. Kim, J. H. Choi, J. B. Park, S. K. Kim, J.-B. Yoo, and C.-Y. Park. Growth characteristics of carbon nanotubes via aluminum nanopore template on Si substrate using PECVD. *Thin Solid Films*, **435**: 312–317, 2003.

[13] R. Martel, T. Schmidt, H. R. Shea, T. Hertel, and P. Avouris. Single-and multi-wall carbon nanotube field-effect transistors. *Applied Physics Letters*, **73**: 2447–2449, 1998.

[14] M. Endo, M. S. Strano, and P. M. Ajayan. "Potential applications of carbon nanotubes" in: *Carbon nanotubes*. Springer, 2007. 13–62

[15] S. J. Wind, J. Appenzeller, R. Martel, V. Derycke, and P. Avouris. Vertical scaling of carbon nanotube field-effect transistors using top gate electrodes. *Applied Physics Letters*, **80**: 3817–3819, 2002.

[16] A. Bachtold, P. Hadley, T. Nakanishi, and C. Dekker. Logic circuits with carbon nanotube transistors. *Science*, **294**: 1317–1320, 2001.

[17] A. Javey, J. Guo, D. B. Farmer, Q. Wang, E. Yenilmez, R. G. Gordon, M. Lundstrom, and H. Dai. Self-aligned ballistic molecular transistors and electrically parallel nanotube arrays. *Nano Letters*, **4**: 1319–1322, 2004.

[18] A. D. Franklin, S. O. Koswatta, D. B. Farmer, J. T. Smith, L. Gignac, C. M. Breslin, S.-J. Han, G. S. Tulevski, H. Miyazoe, W. Haensch, et al. Carbon nanotube complementary wrap-gate transistors. *Nano Letters*, **13**: 2490–2495, 2013.

[19] L.-M. Peng, Z. Zhang, and S. Wang. Carbon nanotube electronics: recent advances. *Materials Today*, **17**: 433–442, 2014.

[20] L. Ding, Z. Zhang, T. Pei, S. Liang, S. Wang, W. Zhou, J. Liu, and L.-M. Peng. Carbon nanotube field-effect transistors for use as pass transistors in integrated logic gates and full subtractor circuits. *ACS Nano*, **6**: 4013–4019, 2012.

[21] L. Ding, Z. Zhang, S. Liang, T. Pei, S. Wang, Y. Li, W. Zhou, J. Liu, and L.-M. Peng. CMOS-based carbon nanotube pass-transistor logic integrated circuits. *Nature Communications*, **3**: 677, 2012.

[22] B. Gao, A. Kleinhammes, X. P. Tang, C. Bower, L. Fleming, Y. Wu, and O. Zhou. Electrochemical intercalation of single-walled carbon nanotubes with lithium. *Chemical Physics Letters*, **307**: 153–157, 1999.

[23] M. Endo, C. Kim, K. Nishimura, T. Fujino, and K. Miyashita. Recent development of carbon materials for Li ion batteries. *Carbon*, **38**: 183–197, 2000.

[24] S. Ahmad, D. Copic, C. George, and M. De Volder. Hierarchical Assemblies of Carbon Nanotubes for Ultraflexible Li-Ion Batteries. *Advanced Materials*, **28**: 6705–6710, 2016.

[25] C. Niu, E. K. Sichel, R. Hoch, D. Moy, and H. Tennent. High power electrochemical capacitors based on carbon nanotube electrodes. *Applied Physics Letters*, **70**: 1480–1482, 1997.

[26] D. T. Pham, T. H. Lee, D. H. Luong, F. Yao, A. Ghosh, V. T. Le, T. H. Kim, B. Li, J. Chang, and Y. H. Lee. Carbon nanotube-bridged graphene 3D building blocks for ultrafast compact supercapacitors. *ACS Nano*, **9**: 2018–2027, 2015.

[27] E. Kymakis, I. Alexandrou, and G. A. J. Amaratunga. High open-circuit voltage photovoltaic devices from carbon-nanotube-polymer composites. *Journal of Applied Physics*, **93**: 1764–1768, 2003.

[28] S. Bhattacharyya, E. Kymakis, and G. A. J. Amaratunga. Photovoltaic properties of dye functionalized single-wall carbon nanotube/conjugated polymer devices. *Chemistry of Materials*, **16**: 4819–4823, 2004.

[29] Z. Li, P. P. Boix, G. Xing, K. Fu, S. A. Kulkarni, S. K. Batabyal, W. Xu, A. Cao, T. C. Sum, N. Mathews, et al. Carbon nanotubes as an efficient hole collector for high voltage methylammonium lead bromide perovskite solar cells. *Nanoscale*, **8**: 6352–6360, 2016.

[30] M. Mittal and A. Kumar. Carbon nanotube (CNT) gas sensors for emissions from fossil fuel burning. *Sensors and Actuators B: Chemical*, **203**: 349–362, 2014.

[31] J. Kong, N. R. Franklin, C. Zhou, M. G. Chapline, S. Peng, K. Cho, and H. Dai. Nanotube molecular wires as chemical sensors. *Science*, **287**: 622–625, 2000.

[32] A. Goldoni, R. Larciprete, L. Petaccia, and S. Lizzit. Single-wall carbon nanotube interaction with gases: sample contaminants and environmental monitoring. *Journal of the American Chemical Society*, **125**: 11329–11333, 2003.

[33] S. Mao, G. Lu, and J. Chen. Nanocarbon-based gas sensors: progress and challenges. *Journal of Materials Chemistry A*, **2**: 5573–5579, 2014.

[34] K. Besteman, J.-O. Lee, F. G. M. Wiertz, H. A. Heering, and C. Dekker. Enzyme-coated carbon nanotubes as single-molecule biosensors. *Nano letters*, **3**: 727–730, 2003.

[35] R. J. Chen, S. Bangsaruntip, K. A. Drouvalakis, N. W. S. Kam, M. Shim, Y. Li, W. Kim, P. J. Utz, and H. Dai. Noncovalent functionalization of carbon nanotubes for highly specific electronic biosensors. *Proceedings of the National Academy of Sciences of the United States of America*, **100**: 4984–4989, 2003.

[36] A. Star, E. Tu, J. Niemann, J.-C. P. Gabriel, C. S. Joiner, and C. Valcke. Label-free detection of DNA hybridization using carbon nanotube network field-effect transistors. *Proceedings of the National Academy of Sciences of the United States of America*, **103**: 921–926, 2006.

[37] S. Vemuru, R Wahi, S Nagarajaiah, and P. Ajayan. Strain sensing using a multiwalled carbon nanotube film. *The Journal of Strain Analysis for Engineering Design*, **44**: 555–562, 2009.

[38] E. Roh, B.-U. Hwang, D. Kim, B.-Y. Kim, and N.-E. Lee. Stretchable, Transparent, Ultrasensitive, and Patchable Strain Sensor for Human–Machine Interfaces Comprising a Nanohybrid of Carbon Nanotubes and Conductive Elastomers. *ACS Nano*, **9**: 6252–6261, 2015.

[39] B. Liu, E. M. Campo, and T. Bossing. *Drosophila* embryos as model to assess cellular and developmental toxicity of multi-walled carbon nanotubes (MWCNT) in living organisms. *PLOS ONE*, **9**: e88681, 2014.

[40] Y. Sato, A. Yokoyama, K.-i. Shibata, Y. Akimoto, S.-I. Ogino, Y. Nodasaka, T. Kohgo, K. Tamura, T. Akasaka, M. Uo, et al. Influence of length on cytotoxicity of multi-walled carbon nanotubes against human acute monocytic leukemia cell line THP-1 in vitro and subcutaneous tissue of rats in vivo. *Molecular BioSystems*, **1**: 176–182, 2005.

[41] H. Dumortier, S. Lacotte, G. Pastorin, R. Marega, W. Wu, D. Bonifazi, J.-P. Briand, M. Prato, S. Muller, and A. Bianco. Functionalized carbon nanotubes are non-cytotoxic and preserve the functionality of primary immune cells. *Nano Letters*, **6**: 1522–1528, 2006.

[42] S. Marchesan, K. Kostarelos, A. Bianco, and M. Prato. The winding road for carbon nanotubes in nanomedicine. *Materials Today*, **18**: 12–19, 2015.

[43] Z. Liu, S. Tabakman, K. Welsher, and H. Dai. Carbon nanotubes in biology and medicine: in vitro and in vivo detection, imaging and drug delivery. *Nano Research*, **2**: 85–120, 2009.

[44] V. Biju. Chemical modifications and bioconjugate reactions of nanomaterials for sensing, imaging, drug delivery and therapy. *Chemical Society Reviews*, **43**: 744–764, 2014.

[45] M. Yuksel, D. G. Colak, M. Akin, I. Cianga, M. Kukut, E. I. Medine, M. Can, S. Sakarya, P. Unak, S. Timur, et al. Nonionic, water self-dispersible âĂIJHairy-RodâĂİ poly (p-phenylene)-g-poly (ethylene glycol) copolymer/carbon nanotube conjugates for targeted cell imaging. *Biomacromolecules*, **13**: 2680–2691, 2012.

[46] H. Wang, Z. Wang, M. Ye, S. Zong, M. Li, P. Chen, X. Ma, and Y. Cui. Optically encoded nanoprobes using single walled carbon nanotube as the building scaffold for magnetic field guided cell imaging. *Talanta*, **119**: 144–150, 2014.

[47] J. N. Coleman, U. Khan, and Y. K. Gun'ko. Mechanical reinforcement of polymers using carbon nanotubes. *Advanced Materials*, **18**: 689–706, 2006.

[48] X.-L. Xie, Y.-W. Mai, and X.-P. Zhou. Dispersion and alignment of carbon nanotubes in polymer matrix: a review. *Materials Science and Engineering: R: Reports*, **49**: 89–112, 2005.

[49] Y. Y. Huang, T. P. J. Knowles, and E. M. Terentjev. Strength of nanotubes, filaments, and nanowires from sonication-induced scission. *Advanced Materials*, **21**: 3945–3948, 2009.

[50] K. L. Lu, R. M. Lago, Y. K. Chen, M. L. H. Green, P. J. F. Harris, and S. C. Tsang. Mechanical damage of carbon nanotubes by ultrasound. *Carbon*, **34**: 814–816, 1996.

[51] J. Y. Huang, F. Ding, and B. I. Yakobson. Dislocation dynamics in multiwalled carbon nanotubes at high temperatures. *Physical review letters*, **100**: 035503, 2008.

[52] M. D. Rossell, C. Kuebel, G. Ilari, F. Rechberger, F. J. Heiligtag, M. Niederberger, D. Koziej, and R. Erni. Impact of sonication pretreatment on carbon nanotubes: A transmission electron microscopy study. *Carbon*, **61**: 404–411, 2013.

[53] A. Lucas, C. Zakri, M. Maugey, M. Pasquali, P. v. d. Schoot, and P. Poulin. Kinetics of nanotube and microfiber scission under sonication. *The Journal of Physical Chemistry C*, **113**: 20599–20605, 2009.

[54] J. S. Taurozzi, V. A. Hackley, and M. R. Wiesner. Preparation of nanoparticle dispersions from powdered material using ultrasonic disruption. *NIST Special Publication*, **1200-2**: 1–15, 2012.

[55] J. H. Park, P. S. Alegaonkar, S. Y. Jeon, and J. B. Yoo. Carbon nanotube composite: Dispersion routes and field emission parameters. *Composites Science and Technology*, **68**: 753–759, 2008.

[56] F. H. Gojny, M. H. G. Wichmann, U. Köpke, B. Fiedler, and K. Schulte. Carbon nanotube-reinforced epoxy-composites: enhanced stiffness and fracture toughness at low nanotube content. *Composites Science and Technology*, **64**: 2363–2371, 2004.

[57] E. T. Thostenson and T.-W. Chou. Processing-structure-multi-functional property relationship in carbon nanotube/epoxy composites. *Carbon*, **44**: 3022–3029, 2006.

[58] J. Y. Huang, H. Yasuda, and H. Mori. Highly curved carbon nanostructures produced by ball-milling. *Chemical Physics Letters*, **303**: 130–134, 1999.

[59] Y. A. Kim, T. Hayashi, Y. Fukai, M. Endo, T. Yanagisawa, and M. S. Dresselhaus. Effect of ball milling on morphology of cup-stacked carbon nanotubes. *Chemical Physics Letters*, **355**: 279–284, 2002.

[60] P. C. Ma, B. Z. Tang, and J.-K. Kim. Conversion of semiconducting behavior of carbon nanotubes using ball milling. *Chemical Physics Letters*, **458**: 166–169, 2008.

[61] J. Sandler, M. S. P. Shaffer, T. Prasse, W. Bauhofer, K. Schulte, and A. H. Windle. Development of a dispersion process for carbon nanotubes in an epoxy matrix and the resulting electrical properties. *Polymer*, **40**: 5967–5971, 1999.

[62] J. Li, P. C. Ma, W. S. Chow, C. K. To, B. Z. Tang, and J.-K. Kim. Correlations between percolation threshold, dispersion state, and aspect ratio of carbon nanotubes. *Advanced Functional Materials*, **17**: 3207–3215, 2007.

[63] T. Villmow, P. Pötschke, S. Pegel, L. Häussler, and B. Kretzschmar. Influence of twin-screw extrusion conditions on the dispersion of multi-walled carbon nanotubes in a poly (lactic acid) matrix. *Polymer*, **49**: 3500–3509, 2008.

[64] W. A. de Heer, W. S. Bacsa, A. Chatelain, T. Gerfin, R. Humphrey-Baker, et al. Aligned carbon nanotube films: production and optical and electronic properties. *Science*, **268**: 845–847, 1995.

[65] M. Baro and A. R. Pal. Pulsed Plasma Assisted Growth of Vertically Aligned Carbon Nanotubes at Low Temperature on Mo Substrate. *Plasma Chemistry and Plasma Processing*, **35**: 247–257, 2015.

[66] P. M. Ajayan, O. Stephan, C. Colliex, D. Trauth, et al. Aligned carbon nanotube arrays formed by cutting a polymer resin-nanotube composite. *Science*, 1212–1212, 1994.

[67] B. Vigolo, A. Penicaud, C. Coulon, C. Sauder, R. Pailler, C. Journet, P. Bernier, and P. Poulin. Macroscopic fibers and ribbons of oriented carbon nanotubes. *Science*, **290**: 1331–1334, 2000.

[68] L. Jin, C. Bower, and O. Zhou. Alignment of carbon nanotubes in a polymer matrix by mechanical stretching. *Applied Physics Letters*, **73**: 1197–1199, 1998.

[69] K. Czaniková, I. Krupa, M. Ilčíková, P. Kasák, D. Chorvár, M. Valentin, M. Šlouf, J. Mosnáček, M. Mičušík, and M. Omastová. Photo-actuating materials based on elastomers and modified carbon nanotubes. *Journal of Nanophotonics*, **6**: 810707, 2011.

[70] S. Courty, J. Mine, A. R. Tajbakhsh, and E. M. Terentjev. Nematic elastomers with aligned carbon nanotubes: New electromechanical actuators. *Europhysics Letters*, **64**: 654, 2003.

[71] E. T. Thostenson and T.-W. Chou. Aligned multi-walled carbon nanotube-reinforced composites: processing and mechanical characterization. *Journal of physics D: Applied physics*, **35**: L77, 2002.

[72] S. V. Ahir, A. M. Squires, A. R. Tajbakhsh, and E. M. Terentjev. Infrared actuation in aligned polymer-nanotube composites. *Physical Review B*, **73**: 085420, 2006.

[73] T. Kimura, H. Ago, M. Tobita, S. Ohshima, M. Kyotani, M. Yumura, et al. Polymer composites of carbon nanotubes aligned by a magnetic field. *Advanced materials*, **14**: 1380–1383, 2002.

[74] E. S. Choi, J. S. Brooks, D. L. Eaton, M. S. Al-Haik, M. Y. Hussaini, H. Garmestani, D. Li, and K. Dahmen. Enhancement of thermal and electrical properties of carbon nanotube polymer composites by magnetic field processing. *Journal of Applied Physics*, **94**: 6034–6039, 2003.

[75] N. J. Pinto, A. T. Johnson Jr, A. G. MacDiarmid, C. H. Mueller, N. Theofylaktos, D. C. Robinson, and F. A. Miranda. Electrospun polyaniline/polyethylene oxide nanofiber field-effect transistor. *Applied Physics Letters*, **83**: 4244–4246, 2003.

[76] M. Li, Y. Guo, Y. Wei, A. G. MacDiarmid, and P. I. Lelkes. Electrospinning polyaniline-contained gelatin nanofibers for tissue engineering applications. *Biomaterials*, **27**: 2705–2715, 2006.

[77] M. V. Kakade, S. Givens, K. Gardner, K. H. Lee, D. B. Chase, and J. F. Rabolt. Electric Field Induced Orientation of Polymer Chains in Macroscopically Aligned Electrospun Polymer Nanofibers. *Journal of the American Chemical Society*, **129**: 2777–2782, 2007.

[78] N. Kimura, H.-K. Kim, B.-S. Kim, K.-H. Lee, and I.-S. Kim. Molecular Orientation and Crystalline Structure of Aligned Electrospun Nylon-6 Nanofibers: Effect of Gap Size. *Macromolecular Materials and Engineering*, **295**: 1090–1096, 2010.

[79] Y. Y. S. Huang, E. M. Terentjev, T. Oppenheim, S. P. Lacour, and M. E. Welland. Fabrication and electromechanical characterization of near-field electrospun composite fibers. *Nanotechnology*, **23**: 105305, 2012.

[80] Y. Dror, W. Salalha, R. L. Khalfin, Y. Cohen, A. L. Yarin, and E. Zussman. Carbon nanotubes embedded in oriented polymer nanofibers by electrospinning. *Langmuir*, **19**: 7012–7020, 2003.

[81] F. Ko, Y. Gogotsi, A. Ali, N. Naguib, H. Ye, G. L. Yang, C. Li, and P. Willis. Electrospinning of continuous carbon nanotube-filled nanofiber yarns. *Advanced Materials*, **15**: 1161–1165, 2003.

[82] R. Sen, B. Zhao, D. Perea, M. E. Itkis, H. Hu, J. Love, E. Bekyarova, and R. C. Haddon. Preparation of single-walled carbon nanotube reinforced polystyrene and polyurethane nanofibers and membranes by electrospinning. *Nano Letters*, **4**: 459–464, 2004.

[83] Z.-M. Huang, Y.-Z. Zhang, M. Kotaki, and S. Ramakrishna. A review on polymer nanofibers by electrospinning and their applications in nanocomposites. *Composites Science and Technology*, **63**: 2223–2253, 2003.

[84] H. Fong, I. Chun, and D. H. Reneker. Beaded nanofibers formed during electrospinning. *Polymer*, **40**: 4585–4592, 1999.

[85] H. Liu and Y.-L. Hsieh. Ultrafine fibrous cellulose membranes from electrospinning of cellulose acetate. *Journal of Polymer Science Part B: Polymer Physics*, **40**: 2119–2129, 2002.

[86] J. Sidaravicius, R. Rinkūnas, J. Jurksus, T. Lozovski, I. Heiskanen, and K. Backfolk. Predicting the electrospinnability of polymer solutions with electromechanical simulation. *Journal of Applied Polymer Science*, **131**: 2014.

[87] P. L. Dickrell, S. K. Pal, G. R. Bourne, C. Muratore, A. A. Voevodin, P. M. Ajayan, L. S. Schadler, and W. G. Sawyer. Tunable friction behavior of oriented carbon nanotube films. *Tribology Letters*, **24**: 85–90, 2006.

[88] S. Banerjee, T. Hemraj-Benny, and S. S. Wong. Covalent surface chemistry of single-walled carbon nanotubes. *Advanced Materials*, **17**: 17–29, 2005.

[89] J. L. Stevens, A. Y. Huang, H. Peng, I. W. Chiang, V. N. Khabashesku, and J. L. Margrave. Sidewall amino-functionalization of single-walled carbon nanotubes through fluorination and subsequent reactions with terminal diamines. *Nano Letters*, **3**: 331–336, 2003.

[90] Q.-H. Zhang and D.-J. Chen. Percolation threshold and morphology of composites of conducting carbon black/polypropylene/EVA. *Journal of Materials Science*, **39**: 1751–1757, 2004.

[91] E. V. Anslyn and D. A. Dougherty. *Modern physical organic chemistry*. University Science Books, 2006.

[92] N. G. Sahoo, S. Rana, J. W. Cho, L. Li, and S. H. Chan. Polymer nanocomposites based on functionalized carbon nanotubes. *Progress in Polymer Science*, **35**: 837–867, 2010.

[93] C. A. Hunter and J. K. M. Sanders. The Nature of π–π Interactions. *Journal of the American Chemical Society*, **112**: 5525–5534, 1990.

[94] M. Nishio, M. Hirota, and Y. Umezawa. *The CH/π interaction: evidence, nature, and consequences*. vol. 21 John Wiley & Sons, 1998.

[95] J. Ran and P. Hobza. On the nature of bonding in lone pair$\cdots$ π-electron complexes: CCSD (T)/complete basis set limit calculations. *Journal of Chemical Theory and Computation*, **5**: 1180–1185, 2009.

[96] J. Robertson. Realistic applications of CNTs. *Materials today*, **7**: 46–52, 2004.

[97] S. L. Teh, D. Linton, and M. D. Dadmun. Controlling Non-Covalent Interactions to Modulate the Dispersion of Fullerenes in Polymer Nanocomposites. *Macromolecules*, **44**: 7737–7745, 2011.

[98] F. Ilhan, M. Gray, and V. M. Rotello. Reversible side chain modification through noncovalent interactions."Plug and play" polymers. *Macromolecules*, **34**: 2597–2601, 2001.

[99] J. U. Lee, J. Huh, K. H. Kim, C. Park, and W. H. Jo. Aqueous suspension of carbon nanotubes via non-covalent functionalization with oligothiophene-terminated poly (ethylene glycol). *Carbon*, **45**: 1051–1057, 2007.

[100] D. Baskaran, J. W. Mays, and M. S. Bratcher. Noncovalent and nonspecific molecular interactions of polymers with multiwalled carbon nanotubes. *Chemistry of Materials*, **17**: 3389–3397, 2005.

[101] S. A. Curran, P. M. Ajayan, W. J. Blau, D. L. Carroll, J. N. Coleman, A. B. Dalton, A. P. Davey, A. Drury, B. McCarthy, S. Maier, et al. A composite from poly (m-phenylenevinylene-co-2, 5-dioctoxy-p-phenylenevinylene) and carbon nanotubes: a novel material for molecular optoelectronics. *Advanced Materials*, **10**: 1091–1093, 1998.

[102] Z. Li, M. Tang, J. Dai, T. Wang, and R. Bai. Effect of multiwalled carbon nanotube-grafted polymer brushes on the mechanical and swelling properties of polyacrylamide composite hydrogels. *Polymer*, **85**: 67–76, 2016.

[103] Z. Han and A. Fina. Thermal conductivity of carbon nanotubes and their polymer nanocomposites: A review. *Progress in Polymer Science*, **36**: 914–944, 2011.

[104] W.-B. Zhang, X.-L. Xu, J.-H. Yang, T. Huang, N. Zhang, Y. Wang, and Z.-W. Zhou. High thermal conductivity of poly (vinylidene fluoride)/carbon nanotubes nanocomposites achieved by adding polyvinylpyrrolidone. *Composites Science and Technology*, **106**: 1–8, 2015.

[105] H. S. Kim, J.-u. Jang, J. Yu, and S. Y. Kim. Thermal conductivity of polymer composites based on the length of multi-walled carbon nanotubes. *Composites Part B: Engineering*, **79**: 505–512, 2015.

[106] H. M. Kim, K. Kim, C. Y. Lee, J. Joo, S. J. Cho, H. S. Yoon, D. A. Pejaković, J.-W. Yoo, and A. J. Epstein. Electrical conductivity and electromagnetic interference shielding of multiwalled carbon nanotube composites containing Fe catalyst. *Applied Physics Letters*, **84**: 589–591, 2004.

[107] Y. Yang, M. C. Gupta, K. L. Dudley, and R. W. Lawrence. Novel carbon nanotube-polystyrene foam composites for electromagnetic interference shielding. *Nano letters*, **5**: 2131–2134, 2005.

[108] N. Li, Y. Huang, F. Du, X. He, X. Lin, H. Gao, Y. Ma, F. Li, Y. Chen, and P. C. Eklund. Electromagnetic interference (EMI) shielding of single-walled carbon nanotube epoxy composites. *Nano letters*, **6**: 1141–1145, 2006.

[109] M. Yang, V. Koutsos, and M. Zaiser. Interactions between polymers and carbon nanotubes: a molecular dynamics study. *The Journal of Physical Chemistry B*, **109**: 10009–10014, 2005.

[110] K. Hayashida and Y. Matsuoka. Electromagnetic interference shielding properties of polymer-grafted carbon nanotube composites with high electrical resistance. *Carbon*, **85**: 363–371, 2015.

[111] B. J. Landi, R. P. Raffaelle, M. J. Heben, J. L. Alleman, W. VanDerveer, and T. Gennett. Single wall carbon nanotube-Nafion composite actuators. *Nano Letters*, **2**: 1329–1332, 2002.

[112] H. Koerner, G. Price, N. A. Pearce, M. Alexander, and R. A. Vaia. Remotely actuated polymer nanocomposites—stress-recovery of carbon-nanotube-filled thermoplastic elastomers. *Nature materials*, **3**: 115–120, 2004.

[113] S. V. Ahir and E. M. Terentjev. Photomechanical actuation in polymer-nanotube composites. *Nature Materials*, **4**: 491–495, 2005.

[114] R. Vaia. Nanocomposites: Remote-controlled actuators. *Nature Materials*, **4**: 429–430, 2005.

[115] R. H. Baughman. Conducting polymer artificial muscles. *Synthetic metals*, **78**: 339–353, 1996.

[116] R. H. Baughman, C. X. Cui, A. A. Zakhidov, Z. Iqbal, and J. N. Barisci. Carbon nanotube actuators. *Science*, **284**: 1340–1344, 1999.

[117] R. H. Baughman. Playing nature's game with artificial muscles. *Science*, **308**: 63–65, 2005.

[118] K. Czaniková, N. Torras, J. Esteve, I. Krupa, P. Kasák, E. Pavlova, D. Raško, I. Chodák, and M. Omastová. Nanocomposite photoactuators based on an ethylene vinyl acetate copolymer filled with carbon nanotubes. *Sensors and Actuators B: Chemical*, **186**: 701–710, 2013.

[119] T. Villmow, S. Pegel, A. John, R. Rentenberger, and P. Pötschle. Liquid sensing: smart polymer/CNT composites. *Materials Today*, **14**: 340–345, 2011.

[120] Q. Fan, Z. Qin, T. Villmow, J. Pionteck, P. Pötschke, Y. Wu, B. Voit, and M. Zhu. Vapor sensing properties of thermoplastic polyurethane multifilament covered with carbon nanotube networks. *Sensors and Actuators B: Chemical*, **156**: 63–70, 2011.

[121] H.-M. So, J. W. Sim, J. Kwon, J. Yun, S. Baik, and W. S. Chang. Carbon nanotube based pressure sensor for flexible electronics. *Materials Research Bulletin*, **48**: 5036–5039, 2013.

[122] L. Han, A. L. Andrady, and D. S. Ensor. Chemical sensing using electrospun polymer/carbon nanotube composite nanofibers with printed-on electrodes. *Sensors and Actuators B: Chemical*, **186**: 52–55, 2013.

[123] M. Vatani, E. D. Engeberg, and J.-W. Choi. Force and slip detection with direct-write compliant tactile sensors using multi-walled carbon nanotube/polymer composites. *Sensors and Actuators A: Physical*, **195**: 90–97, 2013.

[124] N. Hu, Y. Karube, M. Arai, T. Watanabe, C. Yan, Y. Li, Y. Liu, and H. Fukunaga. Investigation on sensitivity of a polymer/carbon nanotube composite strain sensor. *Carbon*, **48**: 680–687, 2010.

Chapter 3

Synchrotron radiation and NEXAFS spectroscopy

3.1 Synchrotron radiation

When charged particles are accelerated in a curved path, the centripetal force on the particles causes intense electromagnetic radiation, which ranges from the infrared to the hard X-ray regions of the spectrum, and whose power is given by equation 3.1:[1]

$$P = \frac{8.86 \times 10^{-5}\, E_{\text{ring}}^4\, I_{\text{ring}}}{\rho}, \tag{3.1}$$

where P is the power in MW, 8.86×10^{-5} is the radiation constant in m/GeV^3, E_{ring} is the energy in the ring in GeV, I_{ring} is the current in the ring in A, and ρ is the radius of the ring curvature in m.

When first observed in synchrotrons and other particle accelerators, this radiation was considered a nuisance for high-energy and particle physics studies, resulting in a major energy loss from the orbiting beams.[2] Gradually, the unavoidable radiation was 'parasitically' exploited as a tool to investigate many aspects of condensed matter—this is now referred to as *first generation sources*.[3] Growing interest led to development of storage rings (described later in the chapter), which form the basis of all synchrotron facilities today. The first facilities dedicated solely to the production of synchrotron radiation, *second generation sources*, were built in mid-1970s, and radiation was produced by bending magnets and wigglers. The first

[1] H. Wiedemann. *Particle accelerator physics*. Springer, 2015.

[2] S. Mobilio and A. Balerna. "Introduction to the main properties of Synchrotron Radiation" in: *CONFERENCE PROCEEDINGS-ITALIAN PHYSICAL SOCIETY*. vol. 82 Editrice Compositori; 1999 2003. 1–24

[3] G. V. Marr. *Handbook on Synchrotron Radiation: Vacuum Ultraviolet and Soft X-ray Processes*. Elsevier, 2013.

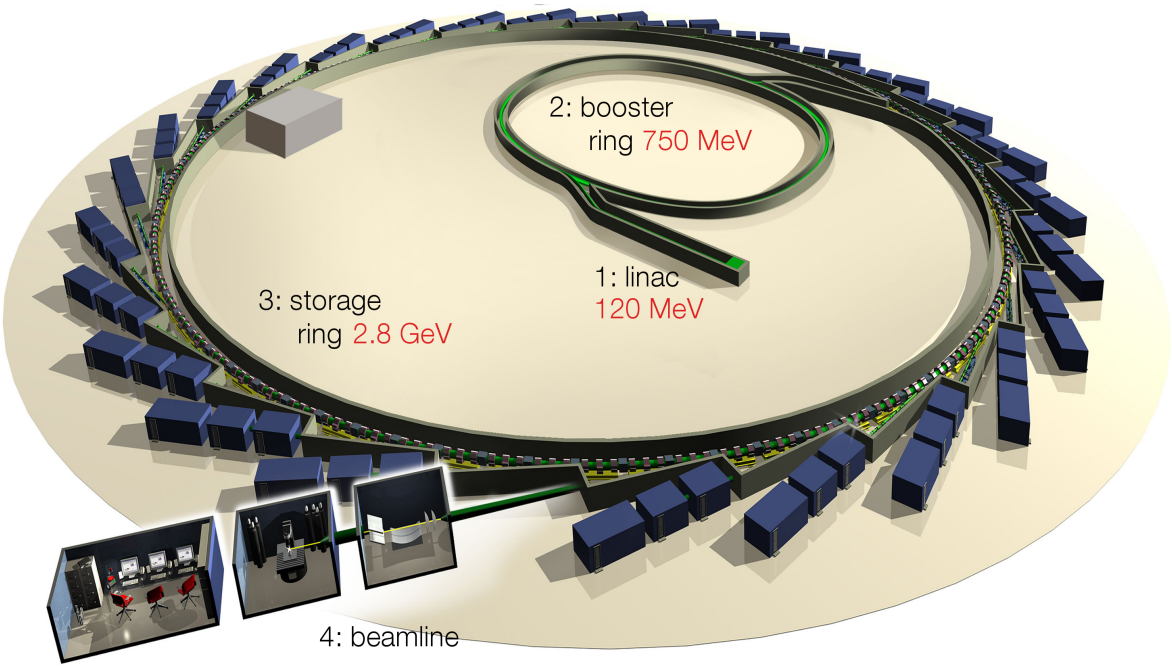

Figure 3.1: Generic synchrotron with the four main components, and corresponding beam energies, highlighted. Electrons from an electron gun are accelerated in the linear accelerator ('linac') and injected into the booster ring. The beam energy increases within the booster ring until it reaches the storage ring energy; at that point, the beam is injected into the storage ring. The beam travels around the storage ring, producing radiation injected into each beamline. Adapted from http://www.lightsources.org/imagebank/image/dls008.

of these sources was the Synchrotron Radiation Source (SRS) at the Daresbury Laboratory, UK. Improvements and optimisation of wrigglers, and introduction of undulators marked the start of *third generation sources*. Following the model of the National Synchrotron Light Source (NSLS, see below), these facilities specialise in either vacuum-ultraviolet, IR, and soft X-rays, or hard X-rays.

3.2 Synchrotron components

Synchrotrons are described by four main components, as depicted in Figure 3.1: linear accelerator (or linac), booster ring, storage ring, and beamlines. Specifications in this chapter are given for the National Synchrotron Light Source (NSLS) in Brookhaven National Laboratory, and the NIST beamline U7A, where all XAS measurements reported in this thesis were acquired.

3.2.1 Linear accelerator

The electron beam that eventually produces synchrotron radiation is generated in a linear accelerator, or *linac*, emitted from a 100 keV triode electron gun, pulsed at 94.6 ns, the booster revolution. A large potential difference provides the initial acceleration; energy is added as the beam passes through a radio frequency cavity. Electrons form bunches as they absorb radiowaves, with sizes related to the radio system wavelength. The linac at NSLS produces bunches of 120 MeV, which are then injected into the booster ring.

3.2.2 Booster ring

The purpose of the booster ring is to achieve the required electron energies (750 MeV at NSLS) before injecting the beam into the storage ring. Acceleration is achieved through similar RF systems as in the linac. Being a circular accelerator, with bending magnets defining electron trajectories, the beam gains more energy each time electrons pass through the RF system, which causes further bunching. The bending magnets cause the beam to produce radiation, according to equation 3.1, which is the desired outcome in the storage ring described below. Within the booster ring, however, this radiation is a nuisance, but it is not considerable compared to the energy gain each time electrons pass through the radio frequency accelerating cavities.

3.2.3 Storage ring

When the beam in the booster ring has gained the required energy, it is injected into the storage ring. The beam travels around the ring, generating (almost) linearly polarised synchrotron radiation as it passes through bending magnets and insertion devices (magnetic structures that produce higher brilliance and better beam quality—the two basic kinds are known as wigglers and undulators), with a final RF system compensating for this energy loss.[4]

NSLS makes use of two storage rings: the X-ray and the VUV (vacuum ultraviolet) storage rings, dedicated to the production of hard X-rays (stored electron beam energy of 2.80 GeV) and vacuum-ultraviolet, IR, and soft X-rays (stored electron beam energy of 808 MeV) respectively.

[4] G. Hähner. *Chem. Soc. Rev.*, **35**: 1244–1255, 2006.

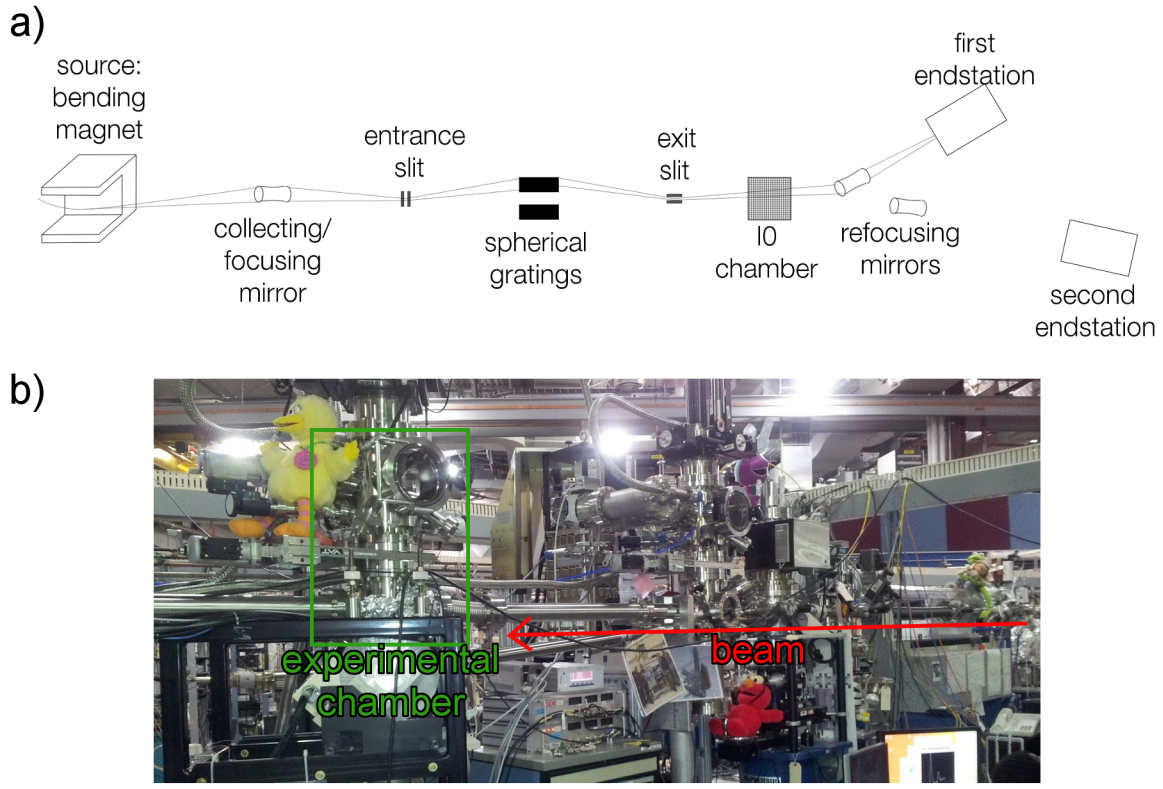

Figure 3.2: a) Optics in beamline U7A; b) Beam path and experimental chamber in U7A

3.2.4 Beamlines

Following synchrotron radiation production in the storage rings, extra beam processing occurs in beamlines, which will be specialised for particular techniques. When the beamline source is a bending magnet—producing the full light spectrum—energy selection occurs in the beamline through a monochromator, which diffracts the radiation. Many monochromator designs exist, each being optimal for a range of energies. Initially U7A employed a toroidal grating monochromator (TGM) design, popular in the 1980's. Although it provided high throughput, the design suffered from optical aberrations, and resolving power was limited by imperfections in the manufacturing of the toroidal figure.[5]

In 1987, Chen described a new monochromator design based on cylindrical optical elements;[6] this became known as the spherical grating monochromator (SGM), and its popularity grew owing to the simplicity of the design, and the resulting high photon energy resolution. The monochromator at U7A was altered in 1995 based on the SGM design, with a single toroidal mirror before the entrance slit in place of the standard Kirkpatrick-Beaz

[5]S. L. Hulbert. "The revitalized NSLS VUV ring" in: *AIP CONFERENCE PROCEEDINGS*. IOP INSTITUTE OF PHYSICS PUBLISHING LTD 2000. 397–404

[6]C. T. Chen. *Nucl. Instrum. Methods A*, **256**: 595–604, 1987.

Table 3.1: Beam parameters at beamline U7A, NSLS, BNL.

Radiation source	Bending magnet
Pressure conditions	UHV ($\sim 10^{-9}$ torr)
Beam energy	180–1100 eV[a]
	400–1600 eV[b]
Beam diameter	~2 mm
Sampling depth	~10 nm[c]
	~100 nm[d]

[a] 600 lines/mm grating.

[b] 1200 lines/mm grating.

[c] Electron yield.

[d] Fluorescence yield.

collecting and focusing mirror pair in the original design:[7] the new design was dubbed the 'toroidal mirror spherical grating monochromator' (TSGM), and offered identical resolution to the standard SGM design, without the need to replace other beamline elements other than the optics. This design has two available gratings: 600 lines/mm and 1200 lines/mm, offering energy ranges of 180–1100 eV and 400–1600 eV respectively (Table 3.1).

As shown in Figure 3.2, beamline U7A has two available endstations in series, served by movable toroidal refocusing mirrors. The first endstation—operated by NIST and Dow Chemical Co—is dedicated to NEXAFS spectroscopy, and features a detector for partial electron yield and fluorecence yield modes with *in situ* capabilities, as well as a novel hyperspectral imaging spectrometer (LARIAT—Large-Area Rapid Imaging Analysis Tool, Synchrotron Research Inc.). The second endstation is operated by the Department of Chemistry in BNL and University of Michigan, and is dedicated to soft X-ray photochemistry; this endstation was not used in the work detailed in this thesis, and will not be further discussed.

3.3 NEXAFS spectroscopy

Near edge X-ray absorption fine structure (NEXAFS) spectroscopy was developed in the 1980's primarily to determine molecular structure of bound low-Z organic systems.[8] Since then, it has been used for the study of many other materials.[4] The technique probes the absorption cross-section of a system by exciting core electrons to *unoccupied* molecular

[7] S. L. Hulbert and G. P. Williams. *Synchrotron Radiat. News*, **10**: 16–21, 1997.

[8] J. Stöhr. *NEXAFS Spectroscopy*. Springer, 2003.

states; a complementary technique is X-ray emission spectroscopy (XES), which illustrates the local partial densities of *occupied* electronic states.[9]

Offering unique insight into chemical and electronic structures, oxidation states, and molecular orientation, this technique has proved an invaluable tool in the study of biomolecules,[10] solid state physics,[11] materials science,[12] catalysis,[13] batteries,[14] and many others. The popularity of this technique is increasing also with developments in hyperspectral detectors,[15] and considerable improvements in *ab initio* theoretical methods.[16]

3.3.1 NEXAFS principles

When an X-ray of energy equal or higher to an atom's electron binding energy is impinged on this atom, the photon is absorbed by a bound core electron, which is excited to an unfilled state, simultaneously generating a core hole. Core holes are highly energetic and unstable, with lifetimes $\sim$ 1 femtosecond.[17] The core hole decays through one of two mechanisms: the emission of an Auger electron, or the emission of a fluorescence photon. Both these events can be measured—Auger emission is highly surface sensitive while fluorescence yield is more bulk sensitive—and provide a measure of X-ray absorption.

The probability of interaction between bound core electrons in a material and incident photons via photoabsorption is measured as the X-ray absorption cross section σ_x, which, derived from Fermi's golden rule, is defined as the ratio of number of electrons excited per unit time to number of incident photons per unit time per unit area:

$$\sigma_x = \frac{4\pi^2 e^2}{m^2 c\omega} |\langle f | \boldsymbol{e} \cdot \boldsymbol{p} | i \rangle|^2 \Psi_f(E) \delta(E_f - E_i - \hbar\omega), \tag{3.2}$$

where $\hbar$ is the reduced Plank constant, e and m are the charge and mass of electrons, c is the speed of light, $\boldsymbol{e}$ is the unit vector, $\boldsymbol{p}$ is the sum of the linear momentum operators, $|i\rangle$ and $|f\rangle$ are the initial and final states, $\Psi_f(E)$ is the set of final state eigenvectors, E_f and E_i are the final and initial state energies, and $\hbar\omega$ is the photon energy.[8]

Experimentally, NEXAFS spectra, which represent σ_x as a function of photon energy,[18]

[9] U. Bergmann and P. Glatzel. *Photosynth. Res.*, **102**: 255–266, 2009.
[10] N. T. Samuel et al. *J. Electron. Spectrosc. Relat. Phenom.*, **152**: 134–142, 2006.
[11] O. Seifarth et al. *J. Vac. Sci. Technol. B*, **27**: 271–276, 2009.
[12] B. Ravel and E. A. Stern. *J. Phys. IV*, **7**: 1223–1224, 1997.
[13] Y. Joseph et al. *Phys. Chem. Chem. Phys.*, **2**: 5314–5319, 2000.
[14] C. F. Petersburg et al. *J. Synchrotron Radiat.*, **16**: 610–615, 2009.
[15] J. E. Baio et al. *Anal. Chem.*, **85**: 4307–4310, 2013.
[16] D. Prendergast and G. Galli. *Phys. Rev. Lett.*, **96**: 215502, 2006.
[17] F. De Groot and A. Kotani. *Core level spectroscopy of solids*. CRC press, 2008.
[18] J. Penner-Hahn. "X-ray Absorption Spectroscopy" in: *Comprehensive Coordination Chemistry {II}* ed. by J. A. McCleverty and T. J. Meyer. vol. 2 Oxford: Pergamon, 2003. 159 –186

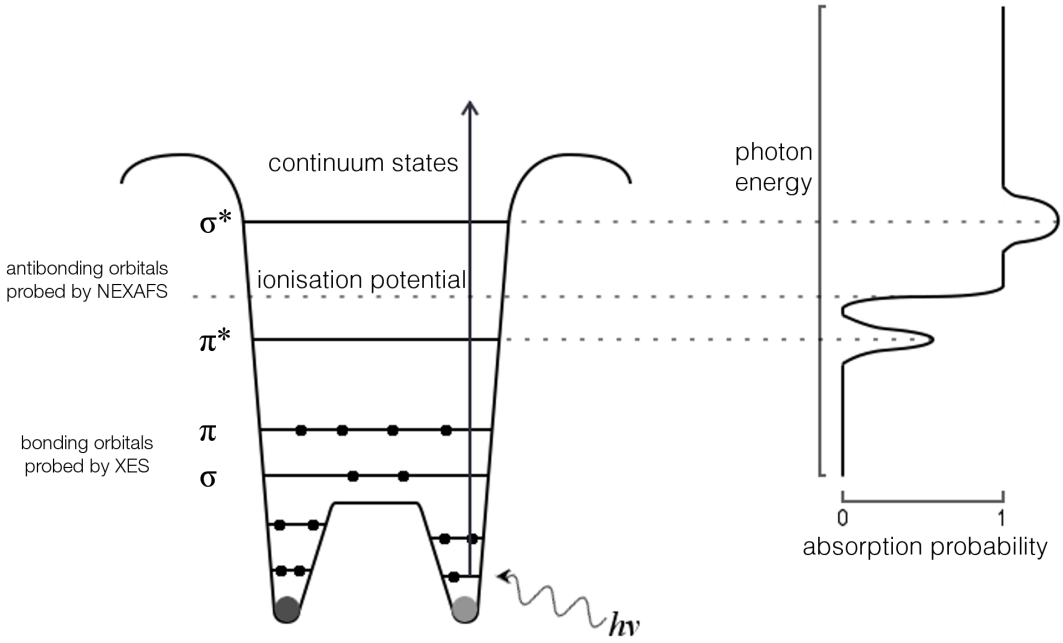

Figure 3.3: NEXAFS spectra reflect the molecular antibonding orbitals of π^* and σ^* symmetries.

can be collected by selecting energies of impinging photons with a monochromator and measuring either electron or fluorescence yield emitted by the sample. These spectra resemble a step function, where little absorption occurs until the photon energy reaches the ionisation potential, at which point there is a considerable increase in absorption. Resonant features superimposed onto the step function occur when the photon energy equals the energy difference between the 1s (in the case of *K*-edges) and unoccupied molecular antibonding states (Figure 3.3), labelled π^* or σ^* according to symmetry.[4] This affords NEXAFS not only chemical sensitivity, but the ability to distinguish orbital hybridisation, e.g. C–C, C=C, C≡C.

For macromolecules, NEXAFS spectra is often interpreted via a building block approach, also called 'fingerprinting', where larger molecules are seen as assemblies of diatomic building blocks with characteristic spectral resonances.[8] This is particularly useful for the study of composite systems, whose NEXAFS will primarily be a linear combination of spectra from individual composite constituents. Equally important, when composite spectra are not linear combinations, they offer a window into the interactions taking place in the system.[19]

An important aspect in the analysis of NEXAFS spectra is the angular dependence of resonances. Indeed, when molecules have a natural alignment, this can be deduced from

[19] A. D. Winter et al. "Noncovalent Interactions in Polymer Nanocomposites" in: *New Horizons in Nanoscience and Engineering* ed. by D. L. Andrews and J. G. Grote. Bellingham, Washington: SPIE Press, 2015. chap. 4, 147–190

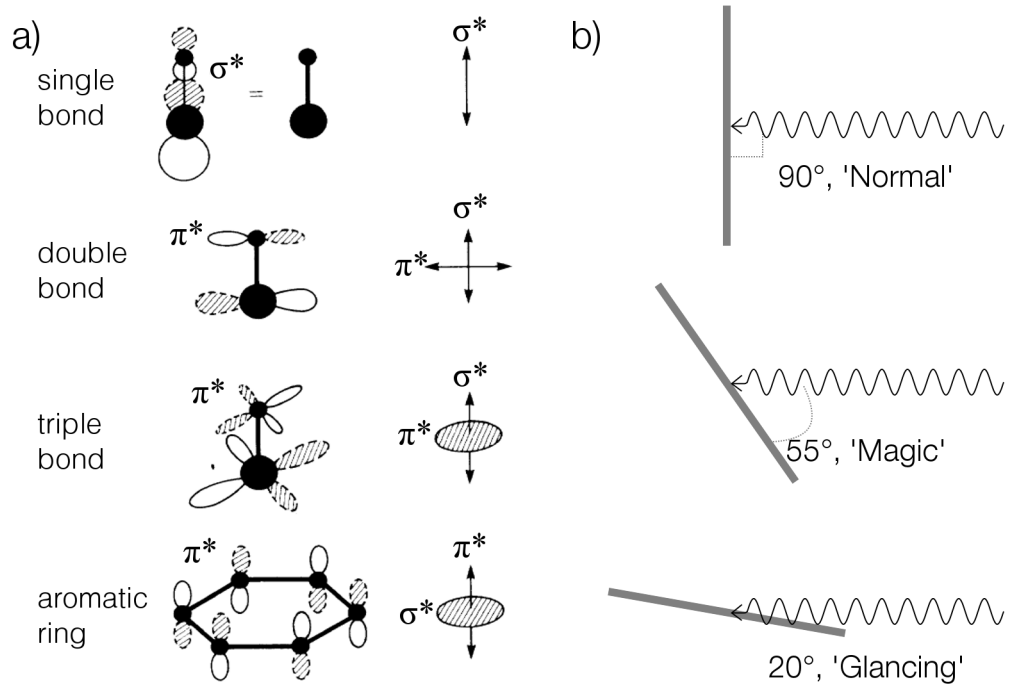

Figure 3.4: a) Classification of molecular orbitals as either 'vectors' or 'planes'. Adapted figure from Stöhr *et al*.[20] with permission. Copyright 2016 by the American Physical Society. b) Angles of orbitals in a) are probed by tilting the experimental stage, typically acquiring NEXAFS spectra at 'normal', 'magic', and 'glancing' incidences.

angle-resolved spectra, typically acquired by tilting the sample stage. The intensity of a resonance is dependent on the angle between the transition vector $\langle f | \boldsymbol{e} \cdot \boldsymbol{p} | i \rangle$ (equation 3.2) and the X-ray electric field vector $\boldsymbol{E}$.[21] For instance, intensity of $\pi^*_{C=C}$ resonances in in-plane aligned carbon nanotubes increases as the angle between the incoming beam and the substrate decreases.[22]

Bending magnets produce linearly horizontally polarised radiation, characterised by the unit vector $\boldsymbol{e}$. By classing the orbitals in groups of molecules as either 'vectors' or 'planes' (Figure 3.4), the angular dependence of each is given by equations 3.3 and 3.4:[8]

$$I_v \propto |\langle f | \boldsymbol{e} \cdot \boldsymbol{p} | i \rangle|_v^2 = \cos^2 \delta, \tag{3.3}$$

$$I_p \propto |\langle f | \boldsymbol{e} \cdot \boldsymbol{p} | i \rangle|_p^2 = \cos^2 \varepsilon, \tag{3.4}$$

where δ and ε are the angles between $\boldsymbol{E}$ and vector direction, and plane normal respectively. Resolving into polar and azimuthal angles of the molecular orbitals, geometrical arrangement

[21] H. Ade and S. Urquhart. "NEXAFS spectroscopy and microscopy of natural and synthetic polymers" in: *Chemical Applications of Synchrotron Radiation, Part I: Dynamics and VUV Spectroscopy* ed. by T.-K. Sham. World Scientific, 2002. chap. 6, 285–355

[22] L. Fleming et al. *J. Vac. Sci. Technol. B*, **22**: 2000–2004, 2004.

of small molecules can be quantitatively derived.[20,23] Experimentally, this is achieved by tilting the sample stage and acquiring spectra at 'normal', 'magic', and 'glancing' incidence angles, as shown in Figure 3.4.

For systems where the preferred alignment of a component (nanoparticle, functional group, etc) needs to be determined, a complementary method to vary the angle between $\langle f | \boldsymbol{e} \cdot \boldsymbol{p} | i \rangle$ and $\boldsymbol{E}$ is to measure NEXAFS with a chosen direction in the sample plane both parallel and perpendicular to $\boldsymbol{E}$—this methodology is also followed in other characterisation techniques that exploit beam polarisation, such as polarised Raman spectroscopy.[24] This is particularly useful when both orientation and alignment need ellucidating. Analysis of spectral intensities acquired this way is usually aided by the dichroic ratio.

$$D_R = \frac{I_{\parallel} - I_{\perp}}{I_{\parallel} + I_{\perp}}. \tag{3.5}$$

Dichroic ratios defined as in 3.5 vary between -1 and 1, with -1 indicating perfect alignment along the chosen direction (parallel to $\boldsymbol{E}$), 1 indicating perfect alignment perpendicular to the chosen direction, and 0 reflecting completely random orientation.

3.3.2 Calibration and post-processing

Prior to analysis of NEXAFS spectra, a few key steps must be followed to enable accurate comparisons between acquisitions. The first procedure is normalisation of spectra to correct for intensity fluctuations, a function of both time and photon energy. These arise from beam instabilities in the ring, as well as dynamics of beamline optical elements.[8] A common method to compensate for these variations is normalisation with a reference grid.

At U7A, a clean gold mesh is placed in the beam path between the last optical element and the sample, and the drain current is measured (figure 3.5a); both sample and grid signals reflect the same beam- and optics-fluctuations. The ratio of the two signals, therefore, cancels out the term related to these variations and serves as a normalised sample signal.

Secondly, there is a degree of uncertainty in the measured impinging photon energy arising from instrumental variability, so the energy must be calibrated. Although the energy shift is usually small, it can lead to erroneous interpretation of NEXAFS if uncalibrated; the $\sigma^*_{\mathrm{C-H}}$ resonance in *trans*-1,4-polyisoprene, for instance, appears at 297.18 eV, but shifts to 287.15 eV in the *cis* configuration.[25]

[20] J. Stöhr and D. A. Outka. *Phys. Rev. B*, **36**: 7891, 1987.
[23] D. A. Outka et al. *J. Chem. Phys.*, **88**: 4076–4087, 1988.
[24] S. Abbasi, P. J. Carreau, and A. Derdouri. *Polymer*, **51**: 922–935, 2010.
[25] O. Dhez, H. Ade, and S. G. Urquhart. *J. Electron Spectrosc. Relat. Phenom.*, **128**: 85–96, 2003.

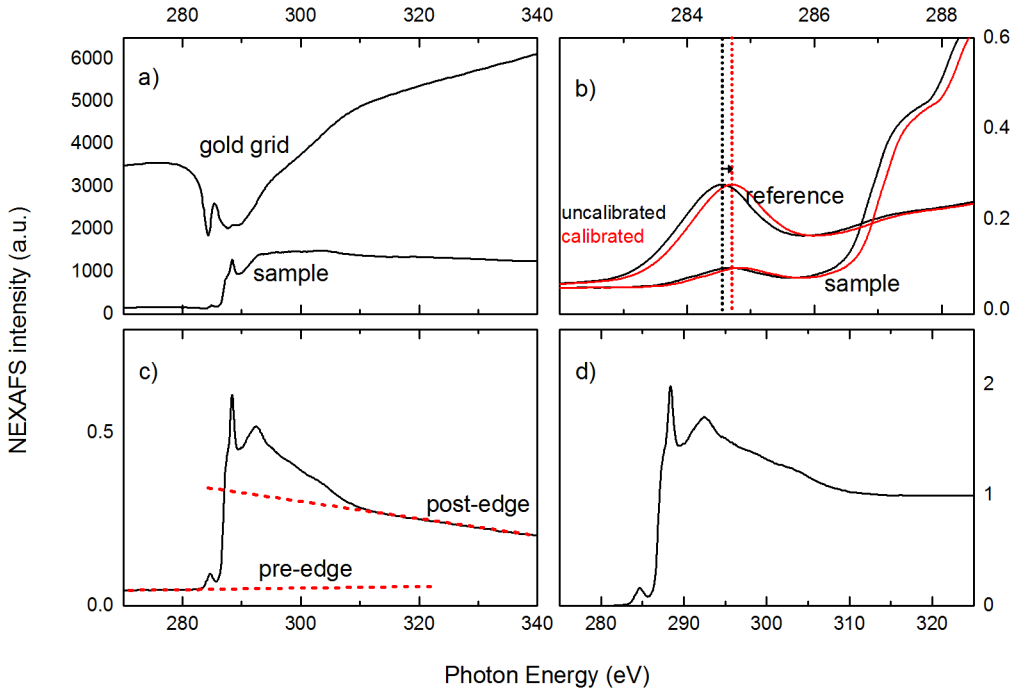

Figure 3.5: Post-processing routines. a) Normalisation of PEY signal to gold mesh; b) calibration with respect to carbon mesh reference; c) background subtraction; d) normalised, calibrated, and background-subtracted NEXAFS spectrum.

To calibrate, NEXAFS spectrum of a known standard (carbon mesh at U7A) is collected in tandem with the sample. The required shift is then applied to the reference and sample spectra simultaneously (Figure 3.5b).

NEXAFS spectra is not only a function of the X-ray absorption coefficient of the sample, but also of the number of photons impinging on the sample surface. To facilitate comparative analysis, the spectral background can be subtracted. This effectively normalises spectra to one incident photon, or one absorbing atom. If energy calibration ensures reliable interpretation of energy variations, background subtraction ensures reliable interpretation of intensity variations.

Background subtraction is achieved using the Athena software package,[26] by selecting a pre-edge and a post-edge line to produce a unit step jump (Figure 3.5c). The choice of these lines is somewhat arbitrary, but it is important that firstly, they do not distort the NEXAFS features of interest, and secondly, they are chosen consistently for every spectrum in a sample set. Figure 3.5d shows a representative normalised, calibrated, and background-subtracted NEXAFS spectrum, ready for analysis.

[26]B. Ravel and M. Newville. *J. Synchrotron Radiat.*, **12**: 537–541, 2005.

3.4 Related NEXAFS research

NEXAFS spectroscopy has been extensively used in the study of polymers and nanoparticles i.e. isolated PNC components. However, perhaps due to the complexity of PNC systems, there are very few published reports where fully assembled PNCs are investigated through NEXAFS. Nevertheless, the same principles are followed across the different materials, and are used in the following chapters which deal with particular PNC systems primarily through NEXAFS spectroscopy.

The sensitivity to chemical environment afforded by NEXAFS has been exploited to elucidate composition and orientation in a wide range of polymeric systems. This has enabled the creation of calibrated libraries of polymer NEXAFS signatures, invaluable for the fingerprinting method.[25,27] Precise orientation of individual molecules has been determined through derivations from equations 3.3 and 3.4, but is less feasible for complex polymer systems with multiple degrees of spatial freedom. Nevertheless, robust orientation characterisation has been achieved for conjugated polymers, such as pentacene and poly(3-hexyl thiophene) (P3HT), enabling also predictions regarding aromatic non-covalent interactions.[28]

Samant and coworkers found uniaxial alignment of buffed polyimide chains along the buffing direction, as well as alignment of π systems perpendicular to chain orientation.[29] Wallace and coworkers furthered this early research to investigate chain relaxation rate differences between polymer bulk and surface, arguing that as thinner devices are fabricated in a shift to 2D material systems, polymers adopt surface-like behaviour.[30] By simultaneously measuring NEXAFS fluorescence and electron yield (probing the first 200 nm and 2 nm respectively), they obtained reasonable bulk and surface absorption cross-sections. Their approach was then to monitor the progression of 'orientational factor' of phenyl rings in strained polystyrene (measured as Dichroic ratios, equation 3.5) as a function of time. They concluded that chain relaxation occurs significantly faster in the surface, compared with bulk relaxation.

Hemraj-Benny and coworkers demonstrated the value of NEXAFS spectroscopy for investigation of nanomaterials, highlighting the ability to determine defects, surface impurities, and alignment.[31] In particular, they monitored both functional impurity groups introduced to CNTs during wet-air oxidation and sidewall-functionalisation, and electronic structure

[27] B. Watts et al. *J. Chem. Phys.*, **134**: 024702, 2011.

[28] D. M. DeLongchamp, E. K. Lin, and D. A. Fischer. "Near-Edge X-Ray Absorption Fine Structure (NEXAFS) Spectroscopy" in: *Organic Field-Effect Transistors*. CRC Press, 2007. 277–299

[29] M. G. Samant et al. *Macromolecules*, **29**: 8334–8342, 1996.

[30] W. E. Wallace et al. *Macromolecules*, **34**: 5081–5082, 2001.

[31] T. Hemraj-Benny et al. *Small*, **2**: 26–35, 2006.

disruption, through fingerprinting and building block analysis.[32]

In their analysis of self-assembled single-walled carbon nanotubes, Fleming *et al* confirmed CNT orientation within the substrate plane by acquiring spectra at three incident angles, where they observed that $\pi^*_{C=C}$ intensities increased as the incidence angle decreased.[22] Additionally, by acquiring spectra both with CNT direction both parallel and perpendicular to the beam polarisation, they reported a significant intensity variation in $\pi^*_{C=C}$ resonance at 90°. This effect confirms that, as well as being oriented along the substrate plane, CNTs assembled into aligned arrays. In this scheme, π^* orbitals along the CNT sidewalls were only accessible the beam in the perpendicular orientation.

On similar lines, Varol and coworkers investigated SiO_2 | styrene–butadiene rubber (SBR) PNCs using angle-resolved NEXAFS spectroscopy, and observed prominent dichroism in $\pi^*_{C=C}$ resonances when SBR chains had been functionalised with silanol groups. [33] They attributed the pronounced angular dependence to an ordering of C=C in SBR chains, leading to an enhanced adhesion to glass surfaces.

The work presented in the following chapters investigates PNC systems primarily with NEXAFS spectroscopy expanding on methods and arguments described here. The resulting publications serve to fill the above-mentioned gap in the literature pertaining to NEXAFS and PNCs.

[32] S. Banerjee et al. *ChemPhysChem*, **5**: 1416–1422, 2004.
[33] H. S. Varol et al. *Macromolecules*, **48**: 7929–7937, 2015.

Bibliography

[1] H. Wiedemann. *Particle accelerator physics*. Springer, 2015.

[2] S. Mobilio and A. Balerna. "Introduction to the main properties of Synchrotron Radiation" in: *CONFERENCE PROCEEDINGS-ITALIAN PHYSICAL SOCIETY*. vol. 82 Editrice Compositori; 1999 2003. 1–24

[3] G. V. Marr. *Handbook on Synchrotron Radiation: Vacuum Ultraviolet and Soft X-ray Processes*. Elsevier, 2013.

[4] G. Hähner. Near edge X-ray absorption fine structure spectroscopy as a tool to probe electronic and structural properties of thin organic films and liquids. *Chemical Society Reviews*, **35**: 1244–1255, 2006.

[5] S. L. Hulbert. "The revitalized NSLS VUV ring" in: *AIP CONFERENCE PROCEEDINGS*. IOP INSTITUTE OF PHYSICS PUBLISHING LTD 2000. 397–404

[6] C. T. Chen. Concept and design procedure for cylindrical element monochromators for synchrotron radiation. *Nuclear Instruments and Methods in Physics Research Section A: Accelerators, Spectrometers, Detectors and Associated Equipment*, **256**: 595–604, 1987.

[7] S. L. Hulbert and G. P. Williams. New experimental facilities at the national synchrotron light source VUV ring. *Synchrotron Radiation News*, **10**: 16–21, 1997.

[8] J. Stöhr. *NEXAFS Spectroscopy*. Springer, 2003.

[9] U. Bergmann and P. Glatzel. X-ray emission spectroscopy. *Photosynthesis research*, **102**: 255–266, 2009.

[10] N. T. Samuel, C.-Y. Lee, L. J. Gamble, D. A. Fischer, and D. G. Castner. NEXAFS characterization of DNA components and molecular-orientation of surface-bound DNA oligomers. *Journal of Electron Spectroscopy and Related Phenomena*, **152**: 134–142, 2006.

[11] O. Seifarth, J. Dabrowski, P. Zaumseil, S. Müller, D. Schmeißer, H. J. Müssig, T. Schroeder, et al. On the band gaps and electronic structure of thin single crystalline praseodymium oxide layers on Si(111). *Journal of Vacuum Science & Technology. B, Microelectronics and Nanometer Structures*, **27**: 271–276, 2009.

[12] B. Ravel and E. A. Stern. Temperature and polarization dependent XANES measurements on single crystal $PbTiO_3$. *Le Journal de Physique IV*, **7**: 1223–1224, 1997.

[13] Y. Joseph, M. Wühn, A. Niklewski, W. Ranke, W. Weiss, C. Wöll, and R. Schlögl. Interaction of ethylbenzene and styrene with iron oxide model catalyst films at low coverages: A NEXAFS study. *Physical Chemistry Chemical Physics*, **2**: 5314–5319, 2000.

[14] C. F. Petersburg, R. C. Daniel, C. Jaye, D. A. Fischer, and F. M. Alamgir. Soft X-ray characterization technique for Li batteries under operating conditions. *Journal of Synchrotron Radiation*, **16**: 610–615, 2009.

[15] J. E. Baio, C. Jaye, D. A. Fischer, and T. Weidner. Multiplexed Orientation and Structure Analysis by Imaging Near-Edge X-ray Absorption Fine Structure (MOSAIX) for Combinatorial Surface Science. *Analytical Chemistry*, **85**: 4307–4310, 2013.

[16] D. Prendergast and G. Galli. X-ray absorption spectra of water from first principles calculations. *Physical review letters*, **96**: 215502, 2006.

[17] F. De Groot and A. Kotani. *Core level spectroscopy of solids*. CRC press, 2008.

[18] J. Penner-Hahn. "X-ray Absorption Spectroscopy" in: *Comprehensive Coordination Chemistry {II}* ed. by J. A. McCleverty and T. J. Meyer. vol. 2 Oxford: Pergamon, 2003. 159 –186

[19] A. D. Winter, E. Larios, C. Jaye, C. Weiland, E. Principe, M. Omastová, and E. M. Campo. "Noncovalent Interactions in Polymer Nanocomposites" in: *New Horizons in Nanoscience and Engineering* ed. by D. L. Andrews and J. G. Grote. Bellingham, Washington: SPIE Press, 2015. chap. 4, 147–190

[20] J. Stöhr and D. A. Outka. Determination of molecular orientations on surfaces from the angular dependence of near-edge x-ray-absorption fine-structure spectra. *Physical Review B*, **36**: 7891, 1987.

[21] H. Ade and S. Urquhart. "NEXAFS spectroscopy and microscopy of natural and synthetic polymers" in: *Chemical Applications of Synchrotron Radiation, Part I: Dynamics and VUV Spectroscopy* ed. by T.-K. Sham. World Scientific, 2002. chap. 6, 285–355

[22] L. Fleming, M. D. Ulrich, K. Efimenko, J. Genzer, A. S. Y. Chan, M. T. E, S. J. Oh, and J. E. Rowe. Near-edge absorption fine structure and UV photoemission spectroscopy studies of aligned single-walled carbon nanotubes on Si (100) substrates. *Journal of Vacuum Science & Technology B: Microelectronics and Nanometer Structures*, **22**: 2000–2004, 2004.

[23] D. A. Outka, J. Stöhr, J. P. Rabe, and J. D. Swalen. The orientation of Langmuir-Blodgett monolayers using NEXAFS. *The Journal of Chemical Physics*, **88**: 4076–4087, 1988.

[24] S. Abbasi, P. J. Carreau, and A. Derdouri. Flow induced orientation of multiwalled carbon nanotubes in polycarbonate nanocomposites: Rheology, conductivity and mechanical properties. *Polymer*, **51**: 922–935, 2010.

[25] O. Dhez, H. Ade, and S. G. Urquhart. Calibrated NEXAFS spectra of some common polymers. *Journal of Electron Spectroscopy and Related Phenomena*, **128**: 85–96, 2003.

[26] B. Ravel and M. Newville. Athena, Artemis, and Hephaestus. *Journal of synchrotron radiation*, **12**: 537–541, 2005.

[27] B. Watts, S. Swaraj, D. Nordlund, J. Lüning, and H. Ade. Calibrated NEXAFS spectra of common conjugated polymers. *The Journal of Chemical Physics*, **134**: 024702, 2011.

[28] D. M. DeLongchamp, E. K. Lin, and D. A. Fischer. "Near-Edge X-Ray Absorption Fine Structure (NEXAFS) Spectroscopy" in: *Organic Field-Effect Transistors*. CRC Press, 2007. 277–299

[29] M. G. Samant, J. Stöhr, H. R. Brown, T. P. Russell, J. M. Sands, and S. K. Kumar. NEXAFS studies on the surface orientation of buffed polyimides. *Macromolecules*, **29**: 8334–8342, 1996.

[30] W. E. Wallace, D. A. Fischer, K. Efimenko, W.-L. Wu, J. Genzer, et al. Polymer chain relaxation: surface outpaces bulk. *Macromolecules*, **34**: 5081–5082, 2001.

[31] T. Hemraj-Benny, S. Banerjee, S. Sambasivan, M. Balasubramanian, D. Fischer, G. Eres, A. A. Puretzky, D. B. Geohegan, D. H. Lowndes, W. Han, J. A. Misewich, and S. S. Wong. Near-Edge X-ray Absorption Fine Structure Spectroscopy as a Tool for Investigating Nanomaterials. *Small*, **2**: 26–35, 2006.

[32] S. Banerjee, T. Hemraj-Benny, M. Balasubramanian, D. Fischer, J. A. Misewich, and S. S. Wong. Surface chemistry and structure of purified, ozonized, multiwalled carbon nanotubes probed by NEXAFS and vibrational spectroscopies. *ChemPhysChem*, **5**: 1416–1422, 2004.

[33] H. S. Varol, M. A. Sánchez, H. Lu, J. E. Baio, C. Malm, N. Encinas, M. R. B. Mermet-Guyennet, N. Martzel, D. Bonn, M. Bonn, et al. Multiscale Effects of Interfacial Polymer Confinement in Silica Nanocomposites. *Macromolecules*, **48**: 7929–7937, 2015.

Chapter 4

Electrospun PDMS–PMMA|MWCNT composites

4.1 Introduction

Alignment of CNTs—of key importance in nanocomposites for the efficient translation of properties from the nano to the macroscale—is usually achieved through post-processing techniques using electrical,[1,2] magnetic,[3] or mechanical forces.[4–7] It is very difficult to achieve uniform CNT alignment through these techniques, however, with a small bundle size. For this reason, electrospinning is gaining popularity as a CNT nanocomposite synthesis technique, as it achieves nanoparticle alignment within the fibres; macroscopic alignment is not achieved, however, since the fibres themselves are randomly distributed. Recent advances in electrospinning have also achieved fibre alignment, through the use of a collector consisting of two pieces of electrically conductive substrates, resulting in uniaxially aligned fibres stretched to span across the gap of these substrates.[8,9] Although these are promising advances for nanocomposite synthesis, interfacial interactions between matrix and filler promoted during electrospinning have not been discussed, and electrospinning dynamics have not been elucidated.[10]

PDMS, a polysiloxane derivative, is a widely used polymer for soft lithography, lab-on-a-

[1] M. R. Diehl et al. *Angew. Chem. Int. Ed.*, **41**: 353–356, 2002.
[2] J. Chung et al. *Langmuir*, **20**: 3011–3017, 2004.
[3] J. Hone et al. *Appl. Phys. Lett.*, **77**: 666–668, 2000.
[4] T. Hertel, R. Martel, and P. Avouris. *J. Phys. Chem. B*, **102**: 910–915, 1998.
[5] L. Jin, C. Bower, and O. Zhou. *Appl. Phys. Lett.*, **73**: 1197–1199, 1998.
[6] K. Jiang, Q. Li, and S. Fan. *Nature*, **419**: 801–801, 2002.
[7] M. D. Lay, J. P. Novak, and E. S. Snow. *Nano Lett.*, **4**: 603–606, 2004.
[8] D. Li, Y. Wang, and Y. Xia. *Nano Lett.*, **3**: 1167–1171, 2003.
[9] M. V. Kakade et al. *J .Am. Chem. Soc.*, **129**: 2777–2782, 2007.
[10] J. Sidaravicius et al. *J. Appl. Polym. Sci.*, **131**: , 2014.

chip devices, and flexible electronics. Its attractive properties include strong water repellency, high flexibility, low glass transition temperature and low surface energy. However, the material has a relatively high cost, poor cohesiveness and film-forming property. Conversely, PMMA, a polycrylate derivative, is a low cost polymer with good cohesiveness and excellent film-forming properties. In this regard, since the difference in materials is so great, PDMS–PMMA blends are more likely to obtain the merits of the individual components.[11] Despite the well-known phase segregation in these blends,[12] the tribological properties of these polymers have been extensively studied for application in the fields of microfluidic devices and bioMEMS/NEMS systems.[13] Additionally in the context of biology, electrospun PDMS–PMMA fibres have been assembled into nanofibrous membranes enabling protein growth.[14] The technological importance of PDMS drives interest in fibre production by electrospinning, and PMMA is an effective carrier polymer to electrospin PDMS, providing chain entanglement needed for fibre production.[14]

This chapter discusses the effects of as-grown MWCNTs bonding on a PDMS–PMMA polymer matrix extruded by electrospinning and collected on a rotating drum.[15] Surface states of composites with untreated CNTs of different dimensions are studied and compared with pristine polymeric blends. This property ensemble is of great importance in the study of CNT composites, where sophisticated conformational bonding has been reported by way of 'polymer wrapping,' and supramolecular chemistry provides multiple bonding possibilities at the nanotube-polymer interface.[16,17] NEXAFS analysis is performed in a building-block model, were spectral assignments for composite constituents are discussed first, and correlated with spectral signatures of final composites.

4.2 Experimental

4.2.1 Materials and reagents

The precursor for electrospinning contained PDMS Sylgard 184 silicone elastomer from Dow Corning with a molecular weight of 60000 (Figure 4.1a) and PMMA purchased from Sigma Aldrich with an average molecular weight of 996000 (Figure 4.1b). The solvents were dimethylformamide (DMF) and tetrahydrofuran (THF), both from Sigma Aldrich. Two

[11] J. Chen and J. A. Gardella. *Macromolecules*, **31**: 9328–9336, 1998.
[12] H. Chen et al. *J. Macromol. Sci., Pure Appl. Chem.*, **46**: 83–89, 2009.
[13] N. S. Tambe and B. Bhushan. *Ultramicroscopy*, **105**: 238–247, 2005.
[14] D. Yang et al. *Biomacromolecules*, **10**: 3335–3340, 2009.
[15] A. D. Winter et al. *Langmuir*, **29**: 15822–15830, 2013.
[16] D. Baskaran, J. W. Mays, and M. S. Bratcher. *Chem. Mater.*, **17**: 3389–3397, 2005.
[17] A. Llanes-Pallas et al. *J. Am. Chem. Soc.*, **133**: 15412–15424, 2011.

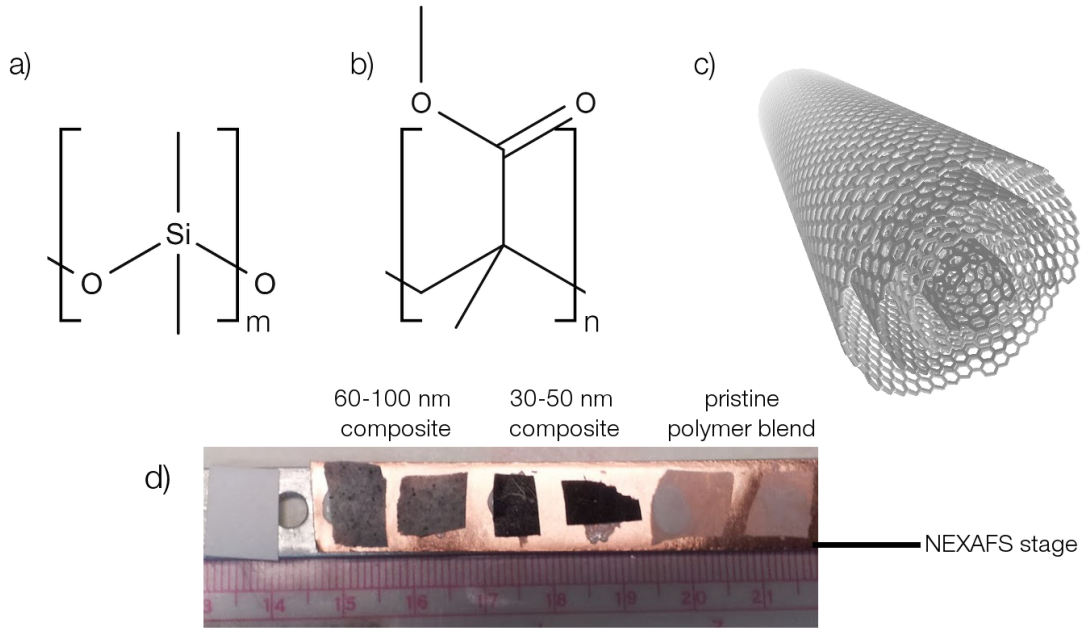

Figure 4.1: Nanocomposite components. a) PDMS, b) PMMA, c) MWCNTs of two diameters—30–50 nm and 60–100 nm. d) Electrospun composites mounted on the NEXAFS stage with collection direction at orthogonal angles.

types MWCNTs were purchased from Nanostructured & Amorphous Materials, Inc: 30–50 nm diameter with 0.5–2 μm length, and 60–100 nm diameter with 5–15 μm length (Figure 4.1c). MWCNTs were synthesised by catalytic CND growth, yielding nanotubes with 95 wt% purity upon acid treatment.

A solution prepared from 2.04 g of PMMA, 10 ml of DMF, and 10 ml of THF, which were mixed at 50 °C for 1 hour under constant magnetic stirring. Upon cooling, 2.02 ml of Sylgard 184 and 0.2 ml of PDMS curing agent were added to the mixture.[14] Finally, two types of unmodified MWCNTs were added under further magnetic stirring to produce two composite samples.

4.2.2 Electrospinning

Electrospinning (aided by a syringe pump and a power supply) was conducted at room temperature (8 kV, 5 cm emitter-collector distance) onto a rotating drum under a white lamp to assist residual solvent evaporation.[18] As a result, dry mats were easily peeled from the collector, avoiding stiction. Following this procedure, three mats were electrospun: PDMS–PMMA|MWCNT$_{30–50nm}$, PDMS–PMMA|MWCNT$_{60–100nm}$, and pristine PDMS–PMMA (Figure

[18]Y. Liu et al. *Macromolecules*, **44**: 4439–4444, 2011.

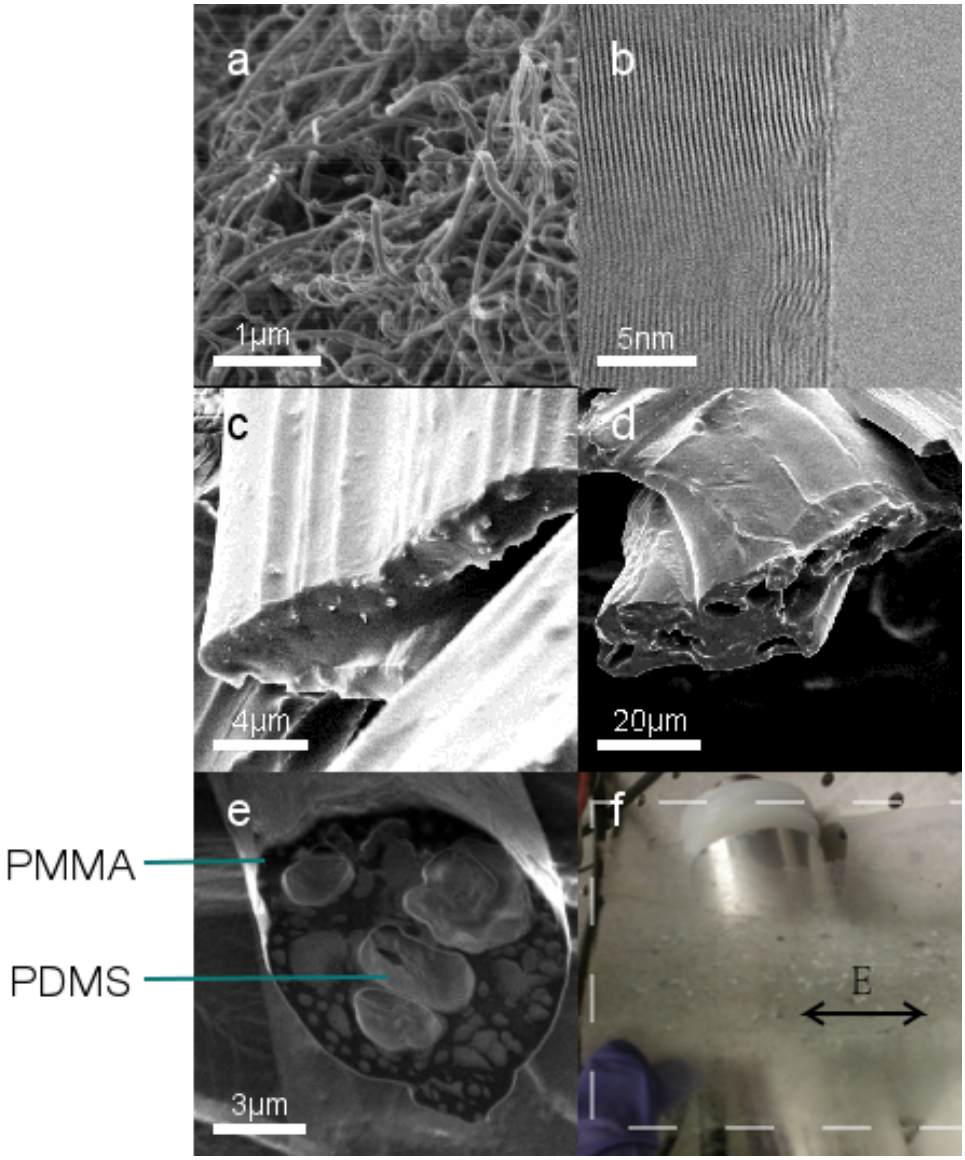

Figure 4.2: *a)* SEM image of 60–100 nm MWCNTs; *b)* TEM micrograph of 60–100 nm MWCNTs; *c)* and *d)* SEM side views of 60–100 nm composite fibres, where different areas show either well-aligned CNTs along the surface of the fibre, or a local absence of CNTs; *e)* Cross-sectional SEM image of 60–100 nm composite fibre revealing phase separation upon focus ion beam milling; *f)* 60–100 nm composite mat, where *E* indicates the collection direction, and the mat perimeter has been traced by a dashed white line.

4.1d).

4.2.3 NEXAFS spectroscopy

Carbon K-edge NEXAFS spectra were collected at NIST beamline U7A (National Synchrotron Light Source, Brookhaven National Laboratory) in partial electron yield mode, with a hori-

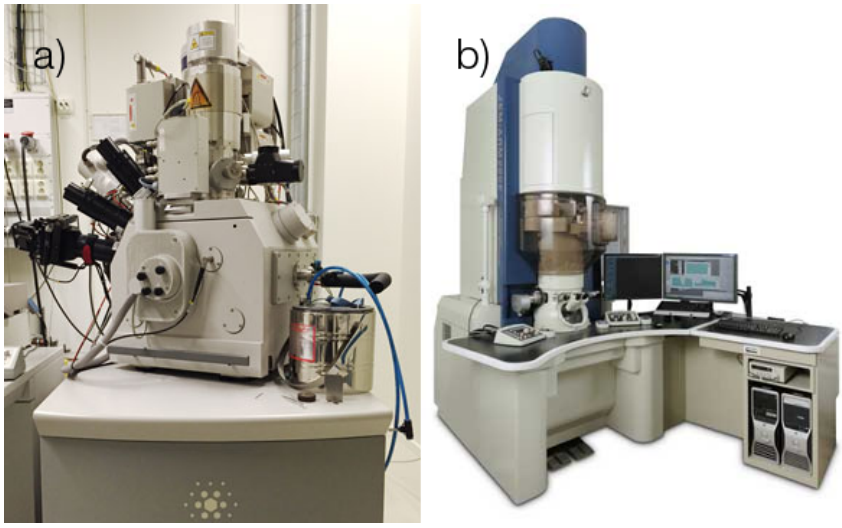

Figure 4.3: a) FEI-235 Strata Scanning Electron Microscope; b) JEOL JEMARM 200F Transmission Electron Microscope.

zontally polarised beam of 2 mm diameter incident spot size. Monochromator grating was set at 600 lines/mm, with 30 μm × 30 μm slits. A floodgun operating at 60 μA prevented surface charging of polymeric samples. For Dichroic analysis, samples were mounted with electrospun fibre direction both parallel and perpendicular to the electric field (Figure 4.1d), and spectra were collected at three incidence angles: 'normal' (90°), 'magic' (55°), and 'glancing' (20°). Repeated scans were conducted at three different locations on the composites to examine chemical homogeneity.

4.2.4 Scanning and Transmission Electron Microscopy

SEM images were acquired at 5 keV on a FEI-235 Strata on SE mode (Figure 4.3a). Some mats were Au-coated to prevent electron charge build up, and Filler 2 was imaged without coating. Focus ion beam milling facilitated cross-section inspection. TEM images were acquired in a JEOL JEM-2010F field-emission operated at 200 kV, and a JEOL JEMARM 200F electron microscope (Figure 4.3b). STEM images were simultaneously recorded in both the high-angle anular dark-field (HAADF) and bright-field (BF) modes at 80 kV. Probe correction was performed with a CEOS corrector obtaining a 12-fold Ronchigram with a flat area of 40 mrad. Images were registered with a condenser lens aperture of 30 μm (convergence angle 25 mrad), and HAADF collection angle ranged from 45 to 180 mrad. Spot size used was 35 pA.

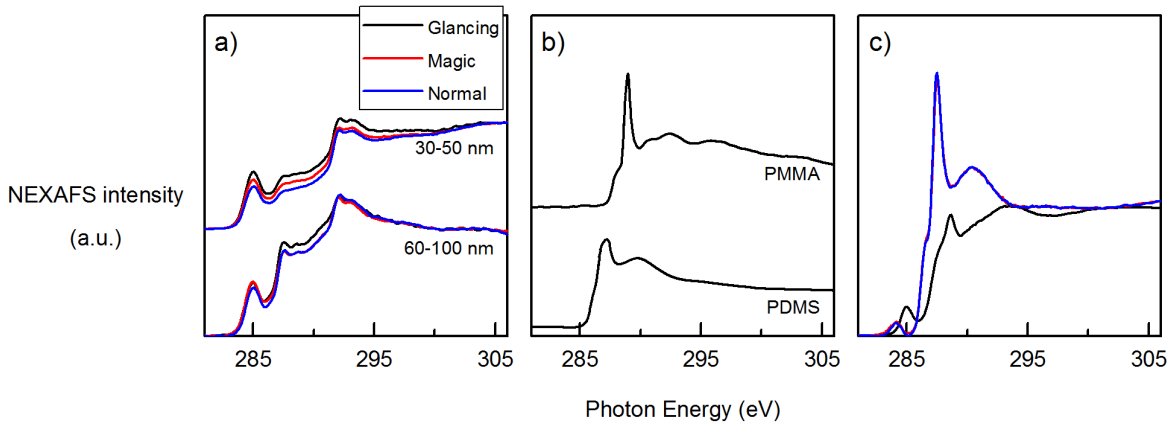

Figure 4.4: Carbon K-edge NEXAFS spectra of composite constituents. *a)* MWCNT of both diameters at normal, magic, and glancing incidences; *b)* standard calibrated spectra of PDMS and PMMA as reported by Efimenko[23] and Dhez[24] respectively; *c)* spectra at normal, magic, and glancing incidences of pristine PDMS–PMMA blend. Apparent 'shift' at glancing incidence possibly a reflection of phase segregation.

4.3 Spectral analysis

4.3.1 Spectral identification

Carbon K-edge NEXAFS spectra of drop-casted MWCNTs of two diameter ranges (Figure 4.4a) show prominent resonances corresponding to $1s \rightarrow \pi^*_{C=C}$ and $1s \rightarrow \sigma^*_{C-C}$ at 285 and 292 eV respectively, in good agreement with experimental and theoretical reports in the literature.[19–22] Levels in the energy range of 287–290 eV indicate the presence of impurity groups e.g. C–H, C–O, C=O, pendent from outer nanotube walls—these are clearly more prominent in larger MWCNTs. For aligned CNTs, intensities of resonances corresponding to $1s \rightarrow \pi^*_{C=C}$ and $1s \rightarrow \sigma^*_{C-C}$ are expected to show opposing trends with incidence angle. Spectra in Figure 4.4a were acquired from dropcasted MWCNTs, however, so no alignment is expected. Some angular intensity variation is seen, particularly from 30–50 nm CNTs, but this likely arises from natural bundling in the suspension before dropcasting.

Reported resonances for pristine PDMS and PMMA, adapted from Efimenko and Dhez respectively,[23,24] are shown in Figure 4.4b. Both polymers share a common $1s \rightarrow \sigma^*_{C-H}$

[19] T. Hemraj-Benny et al. *Small*, **2**: 26–35, 2006.
[20] E. Najafi et al. *Small*, **4**: 2279–2285, 2008.
[21] V. Lee et al. *J. Phys. Chem. Lett.*, **1**: 1247–1253, 2010.
[22] B. J. Schultz et al. *Nature Commun.*, **2**: 372, 2011.
[23] K. Efimenko, W. E. Wallace, and J. Genzer. *J. Colloid Interface Sci.*, **254**: 306–315, 2002.
[24] O. Dhez, H. Ade, and S. G. Urquhart. *J. Electron Spectrosc. Relat. Phenom.*, **128**: 85–96, 2003.

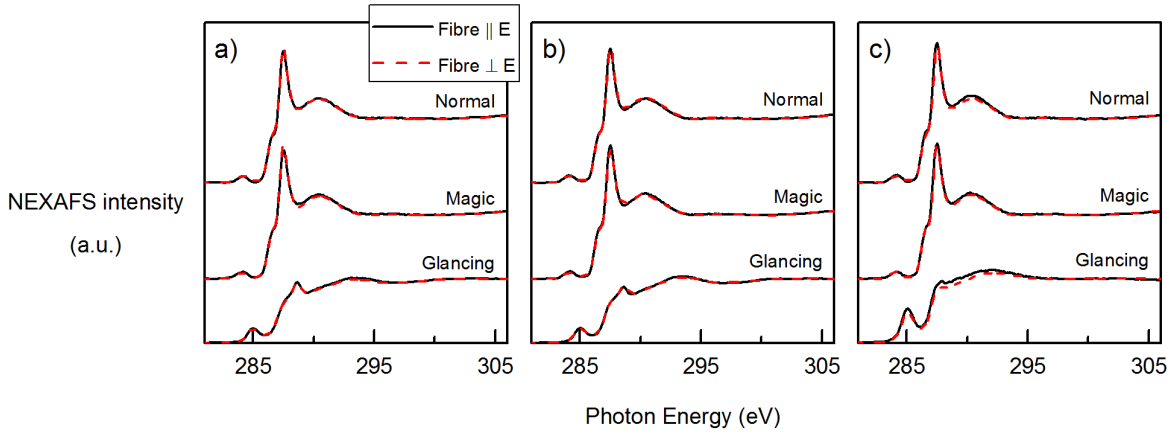

Figure 4.5: Carbon K-edge NEXAFS spectra acquired at normal, magic, and glancing incidences, with fibre direction both parallel and perpendicular to the electric field **E** of *a)* pristine PDMS–PMMA blend, *b)* 30–50 nm composite, and *c)* 60–100 nm composite.

transition at 287.5 eV, seen as a shoulder in PMMA, which also appears in CNT spectra as impurities. In particular, PDMS is characterised by a broad $1s \rightarrow \sigma^*_{C-Si}$ at 290 eV, whilst PMMA has a sharp $1s \rightarrow \pi^*_{C=O}$ and a broad $1s \rightarrow \sigma^*_{C-C}$ transition at 288 eV and 292 eV respectively.

Figure 4.5 shows spectra of the pristine PDMS–PMMA blend and both composite systems at normal, magic and glancing incidences, acquired both with fibre direction parallel and perpendicular to the electric field. Spectra of pristine PDMS–PMMA blend (Figure 4.4c) are not linear combinations of individual polymer spectra, as one might expect. In fact, spectra acquired at normal and magic incidence resemble the spectral fingerprint of PDMS (based on resonance energy positions), whilst, at glancing incidence angle, blend spectrum resembles PMMA more closely. Since all blend spectra show a slight shoulder preceding the sharp peak at 287.5 eV (288.5 eV in glancing spectrum), it can also be argued that spectra are dominated by PMMA, with an energy shift at glancing incidence which needs to be explained. This will be addressed later in this chapter. Either way, the clear angular phenomenon is likely arising from phase separation.[25] Indeed, SEM confirms this typical phase separation (Figure 4.2e), where PDMS—shown as brighter contrast due to the higher atomic weight of silicon—forms islands surrounded by PMMA background.

A brief note should be mentioned about the small pre-edge features observed in spectra of pristine blends centred around 284 eV. These resonances correspond to $1s \rightarrow \pi^*_{C=C}$ transitions, which are seen prominently in CNT spectra (Figure 4.4a), however the polymeric system contains no C=C πbonds. Although UV irradiation and ozone exposure of PDMS could result in a signal below the absorption edge (attributed to second-order oxygen harmonics),[23]

[25] M. Harris, G. Appel, and H. Ade. *Macromolecules*, **36**: 3307–3314, 2003.

processing of the films under study only involved exposure to lamp irradiation in air to promote solvent evaporation, suggesting the observed features most likely arise from surficial carbonaceous impurities.

4.3.2 Alignment, homogeneity, molecular conformation

Spectra of composites were acquired with the collection direction both parallel and perpendicular to the electric field vector **E**, by mounting samples with collection direction at 90° (Figure 4.1d). For a perfectly aligned array of CNTs within the matrix, parallel spectra should show minimal π^* and maximum σ^* intensities at normal incidence, and vice versa in perpendicular spectra.[26] This is due to the electron excitation expected to go as $\mathbf{E} \cdot \mathbf{n}$, where **n** is directed along the orbital—normal to the surface of the nanotube for π^* orbitals.[26] Here, however, there are no significant intensity differences between parallel and perpendicular spectra. Although this would suggest the CNTs are not aligned, SEM very clearly shows CNTs aligned in the fibre direction (Figure 4.2c); the reason this is not reflected in the composite spectra is that the polymeric fibres are not uniformly aligned. As mentioned earlier, fibre alignment in electrospinning could be achieved with an additional field,[8,9] but this was not implemented during the synthesis of these systems.

At normal and magic incidences, spectra of composite systems are very similar to those of the pristine blend (Figure 4.5b and c) i.e. there is no spectral indication of CNT presence at these angles. Again, similarly to pristine blend, spectra at glancing incidence are significantly different—following the prior discussion, this is expected as the effect is attributed to polymeric phase segregation. At glancing incidence, however, effects of CNTs can be observed, and more so for 60–100 nm composite, where spectra show a significant increase in $1s \rightarrow \pi^*_{C=C}$ intensity.

It is worth mentioning that, although polymeric phase segregation is evident in SEM (Figure 4.2c), NEXAFS spectra acquired from three different locations in both composites (Figure 4.6) reveal little spectral variation, suggesting electrospinning renders good chemical homogeneity—at least at the μm length scale.

As described above, one interpretation of the clear spectral change at glancing incidence is that the synchrotron beam probes mostly PDMS at normal and magic angles whilst probing mostly PMMA at glancing, consistent with cross-sectional SEM (Figure 4.2e). By this interpretation, we would conclude that CNTs are confined within the PMMA phase, as spectral evidence of CNTs is only observed at glancing incidence. This can be confirmed through interfacial energy considerations by calculating the wetting coefficient w_a, as described by

[26] L. Fleming et al. *J. Vac. Sci. Technol. B*, **22**: 2000–2004, 2004.

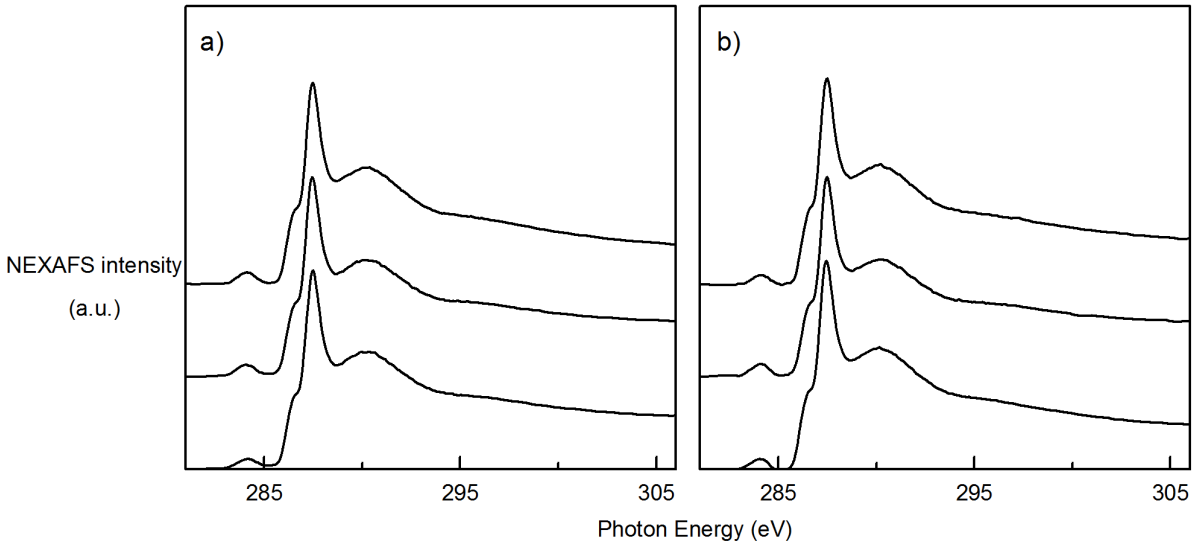

Figure 4.6: The lack of spectral variation in NEXAFS acquisitions from three different locations in a) 30–50 nm MWCNT composite and b) 60–100 nm MWCNT composite indicates good chemical homogeneity.

equation 4.1.[27]

$$w_a = \frac{\gamma_{\text{CNT–PDMS}} - \gamma_{\text{CNT–PMMA}}}{\gamma_{\text{PDMS–PMMA}}}. \tag{4.1}$$

Here, CNTs are predicted to be localised within PMMA phase if $w_a > 1$, at interphase for $-1 < w_a < 1$. and within the PDMS phase if $w_a < 1$. Interfacial energies were calculated by both the harmonic (equation 4.2) and geometric (equation 4.3) mean equations.

$$\gamma_{12} = \gamma_1 + \gamma_2 - 4\left[\frac{\gamma_1^d \gamma_2^d}{\gamma_1^d + \gamma_2^d} + \frac{\gamma_1^p \gamma_2^p}{\gamma_1^p + \gamma_2^p}\right], \tag{4.2}$$

$$\gamma_{12} = \gamma_1 + \gamma_2 - 2\left[\sqrt{\gamma_1^d \gamma_2^d} + \sqrt{\gamma_1^p \gamma_2^p p}\right], \tag{4.3}$$

where γ_1 and γ_2 are surface energies of components 1 and 2, and the superscripts 'd' and 'p' denote the disperse and the polar parts of surface energies. From the literature, $\gamma_{\text{PDMS}} = 20.4\ \text{mJ m}^{-2}$ ($\gamma^d_{\text{PDMS}} = 19.5$ and $\gamma^p_{\text{PDMS}} = 0.9$),[28] $\gamma_{\text{PMMA}} = 41.1\ \text{mJ m}^{-2}$ ($\gamma^d_{\text{PMMA}} = 29.0$ and $\gamma^p_{\text{PMMA}} = 12.1$),[29] and $\gamma_{\text{CNT}} = 45.3\ \text{mJ m}^{-2}$ ($\gamma^d_{\text{CNT}} = 18.6$ and $\gamma^p_{\text{CNT}} = 26.7$).[30]

[27] A. Göldel, G. Kasaliwal, and P. Pötschke. *Macromol. Rapid Commun.*, **30**: 423–429, 2009.

[28] J. Brandup, E. H. Immergut, and E. A. Grulke. *Polymer handbook*. vol. 89 Wiley, New York, 1989. 213

[29] S. Wu. "Calculation of interfacial tension in polymer systems" in: *Journal of Polymer Science Part C: Polymer Symposia*. vol. 34 1 Wiley Online Library 1971. 19–30

[30] S. Nuriel et al. *Chem. Phys. Lett.*, **404**: 263–266, 2005.

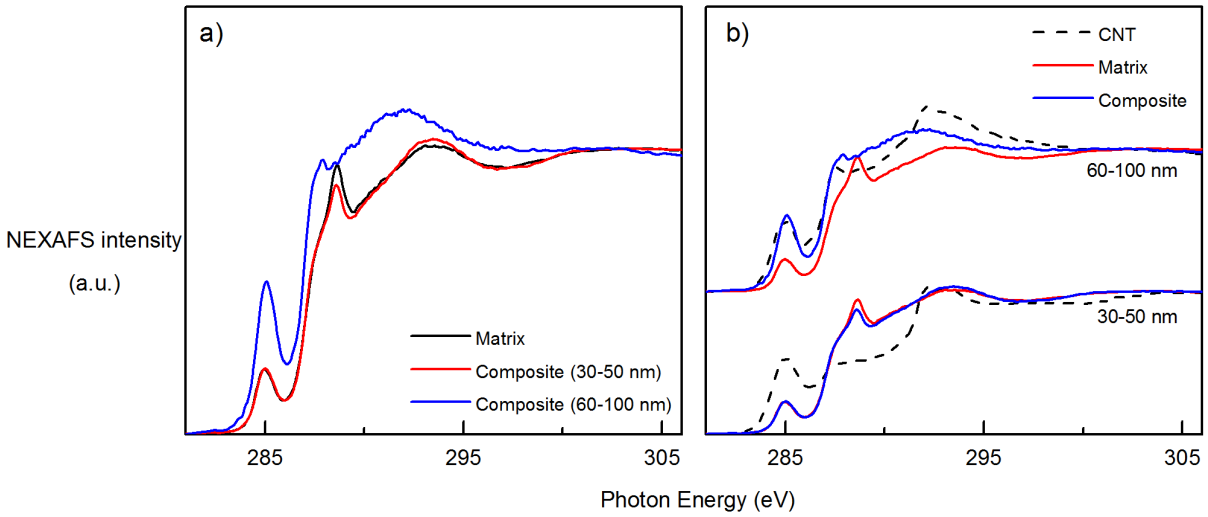

Figure 4.7: Analysis of composite spectra at glancing incidence reveals polymer–CNT interactions.

Computed with the harmonic mean equation (equation 4.2), interfacial energies of PDMS–PMMA, CNT–PDMS, and CNT–PMMA are 11.51, 24.14, and 7.77 mJ m^{-2} respectively, which results in a wetting coefficient $w_a = 1.42$. Likewise, using the geometric mean equation (equation 4.3), interfacial energies are 7.34, 17.8, and 4.0 mJ m^{-2}, which results in $w_a = 1.88$. Both methodologies reveal that CNTs are indeed confined within the PMMA phase. This further supports the argument that spectra of the blend at normal and magic incidences are dominated by PDMS, whilst at glancing incidence the signature is of mostly of PMMA.

Analysis of composite spectra exclusively acquired at glancing incidence (Figure 4.7) reveals polymer–CNT interactions. Indeed, these interactions result in spectra which are not linear combinations of individual components, and this is most notably seen for 60–100 nm composite (Figure 4.7a)—this is addressed in the bonding schemes proposed below. Whilst the considerable increase in $1s \rightarrow \pi^*_{C=C}$ resonance intensity at 285 eV is simply indicative of CNT presence, the new spectral signature in the energy range of 287–290 eV may reveal the chemical groups involved in the interfacial interactions; namely, C–H, C–O and C=O—either impurities in CNTs, or pendant groups in the polymers.

4.4 Non-covalent interaction models

Next, two possible models of interaction are proposed (depicted in Figure 4.8), both of a non-covalent nature since composite synthesis is energetically too low to promote covalent bonding. The first of these schemes involves hydrogen bonding—an electrostatic dipole-dipole interaction—between electronegative moeties in the polymer chains and Hydrogen atoms bound to other electronegative atoms (e.g. Oxygen) as impurities in CNT walls.

Common impurities in CVD-grown CNTs include 1 mol% carboxyl groups (OH–C=O). Since the NEXAFS spectrum of 60–100 nm MWCNTs showed higher impurity states than the smaller diameter CNTs, this bonding scheme would explain the greater interactions observed in composites with 60–100 nm MWCNTs (Figure 4.4a).

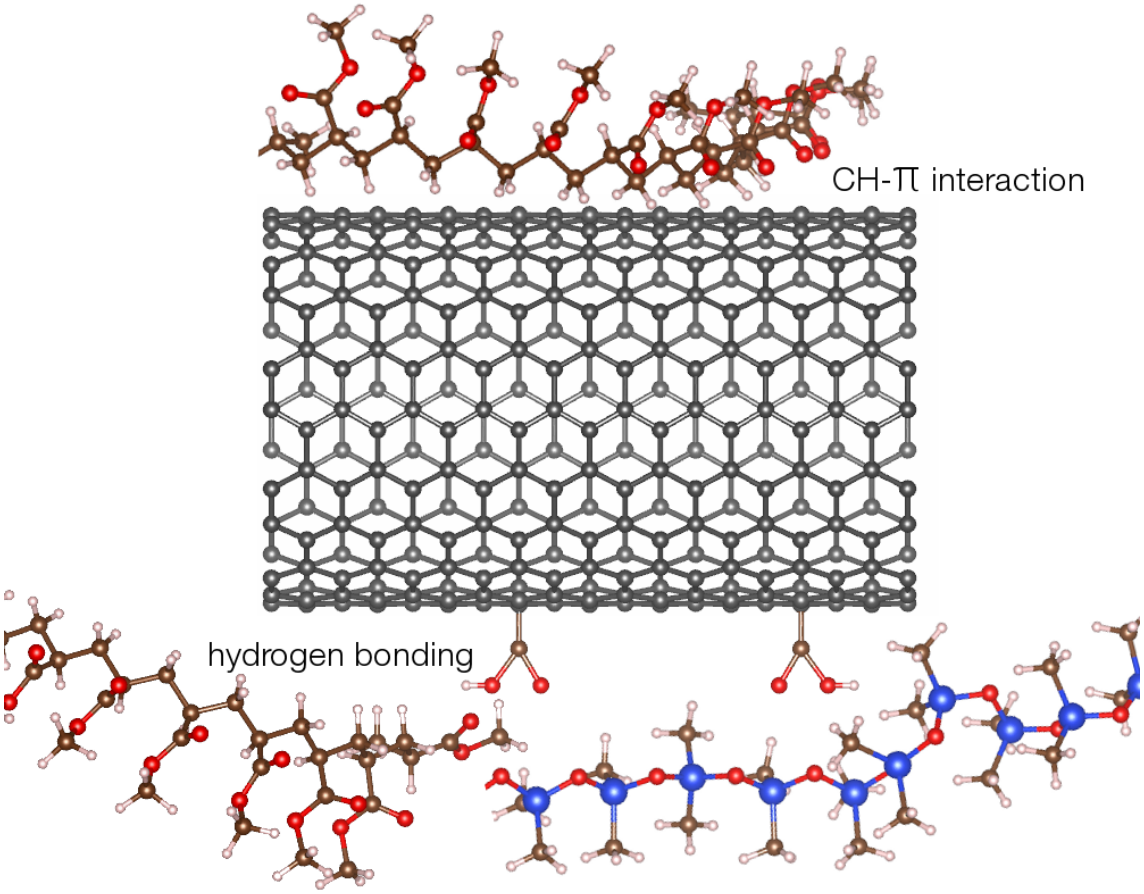

Figure 4.8: Both CH—π interactions and Hydrogen bonding through impurities are viable adhesion mechanisms.

The second interaction model involves CH—π interactions, which occur between aliphatic –CH moeties in polymer chains and aromatic π systems in CNT walls. This mode of adsorption was first reported by Andretti and coworkers in 1979,[31] but the nature of these interactions is still subject of dispute. Initial reports classified CH—π interactions as soft acid/soft base interactions;[32] later publications considered them to be weak hydrogen bonds.[33] More recent work noted that unlike hydrogen bonds, CH—π interactions have a major contribution

[31]G. D. Andreetti, R. Ungaro, and A. Pochini. *J. Chem. Soc. Chem. Commun.*, **22**: 1005–1007, 1979.

[32]G. Klopman. *Chemical Reactivity and Reaction Paths*. New York: Wiley-Interscience, 1974.

[33]M. Nishio, M. Hirota, and Y. Umezawa. *The CH/π interaction: evidence, nature, and consequences*. vol. 21 John Wiley & Sons, 1998.

from dispersion forces, as well as an electrostatic component.[34] Despite this disagreement, it has been established that these interactions are indeed weak, with the enthalpy of a single CH$-\pi$ interaction being less than 1 kcal mol^{-1},[35] although the total energy is significantly increased through cooperative multiple interactions.[34] Further, it was recently demonstrated that the electrostatic contribution of CH$-\pi$ interactions can be modulated by increasing the acidity of the CH moeities.[36]

As CNT diameters increase and the curvature reduces, graphitic walls resemble graphene more closely. Conversely, with increased curvature, resulting from decreasing diameters, π systems become more distorted. This suggests that nanotubes with larger diameters are more prone to CH$-\pi$ interactions, explaining the more notable spectral effects in Figure 4.7. Additionally, the energy region of 287-290 eV, whch shows the most spectral variation in composites, is where CH$-\pi$ interactions have been identified in NEXAFS.[37]

4.5 Linear combination analysis

Linear combination analysis (LCA) is a standard approach to fitting unknown data through a least-squares minimisation procedure. Within the field of XAS and synchrotron techniques, LCA is widely employed to investigate reaction dynamics and identify chemical intermediates.[38–40] The technique generates the best possible linear combination fit (LCF) for a target spectrum from a library of strandard reference spectra through iteration of equations 4.4 and 4.5, where $\mu_i(E)$ are the n known standards with weights w_i, and $\mu_{\text{exp}}(E)$ is the experimental spectrum. The algorithm iterates until the R-factor is minimised, and the resulting LCF is described by the weights assigned to each standard.

$$\mu_{\text{LCF}}(E) = \sum_{i=1}^{n} w_i \mu_i(E), \tag{4.4}$$

$$R_{\text{factor}} = \frac{\sum(\mu_{\text{exp}}(E) - \mu_{\text{LCF}}(E))^2}{\sum \mu_{\text{exp}}(E)^2} \tag{4.5}$$

As a NEXAFS data treatment, LCA has aided in the identification of oxidation states of metals such as cobalt and gold, by progressive fits of time-resolved acquisitions.[38–40]

[34] G. Aragay et al. *Molecules*, **20**: 16672–16686, 2015.

[35] I. Fleming. *Molecular Orbitals and Organic Chemical Reactions*. 2nd ed. John Wiley & Sons Ltd: London, UK, 2009.

[36] E. Jiménez-Moreno et al. *Angew. Chem.*, **127**: 4418–4422, 2015.

[37] N. Kocharova et al. *Langmuir*, **24**: 3235–3243, 2008.

[38] M. C. Urbina et al. *J. Phys. Chem. C*, **112**: 11102–11108, 2008.

[39] M. Bonne et al. *Chem. Commun.*, **47**: 1509–1511, 2011.

[40] M. F. Lengke et al. *Environ. Sci. Technol.*, **40**: 6304–6309, 2006.

More sophisticated LCA curation from hyperspectral acquisitions permitted reconstruction of chemical 3D topographic maps of composite electrodes down to the nanometre scale.[41]

Here, LCA is explored for static systems in the building-block context in which NEXAFS is usually described, where the composite spectrum $\mu_{\text{composite}} = w_1\mu_{\text{filler}} + w_2\mu_{\text{matrix}} + w_3\mu_{\text{interaction}}$, in an effort towards isolating $\mu_{\text{interaction}}$. This approach would result in the construction of a library of interactions as a function of chemistry and processing in the spirit of the Materials Genome Initiative.[42]

In the case of the composites under study in this chapter, a discrepancy in the LCF and the data indicates interaction between the polymer and carbon nanotubes. As a first approximation, an LCF can be obtained using the spectra of PDMS–PMMA blend and CNTs as standards:

$$\mu_{\text{composite}}(E) = w_1\mu_{\text{MWCNT}}(E) + w_2\mu_{\text{matrix}}(E). \tag{4.6}$$

Considering first 30–50 nm MWCNT composite, Figure 4.9a shows that a good fit was obtained using the polymer and CNTs as standards (weights shown in Table 4.1), although it did not exactly reproduce the experimental data. The fit assigns the greatest weight to the polymer, as is expected because the differences between the polymer and composite spectra are relatively small, and the residual (difference between data and fit) is insignificant. This is not the case with composites containing 60–100 nm MWCNTs, which are considered next.

Table 4.1: LCF weights for initial linear combination of composites using equation 4.6.

Standard	Weight[a]	Weight[b]
PDMS–PMMA	0.897	0.705
MWCNTs	0.103	0.295

[a] 30–50 nm MWCNT composite, *R*-factor = 0.0004.

[b] 60–100 nm MWCNT composite, *R*-factor = 0.0130.

Once again, the initial fit is obtained from PDMS–PMMA and spectra of 60–100 nm MWCNTs, following equation 4.6. The LCF is shown alongside experimental data in Figure 4.9c and resulting weights are given in Table 4.1. This time, a poor LCF is obtained, with a significant residual produced (Figure 4.9d), suggesting the matrix–filler interaction—absent from the standards—plays a prominent role in the spectrum. This residual is clearly related to the new term in equation 4.7.

[41] F. Meirer et al. *J. Synchrotron Radiat.*, **18**: 773–781, 2011.

[42] A. Jain et al. *APL Mater.*, **1**: 011002, 2013.

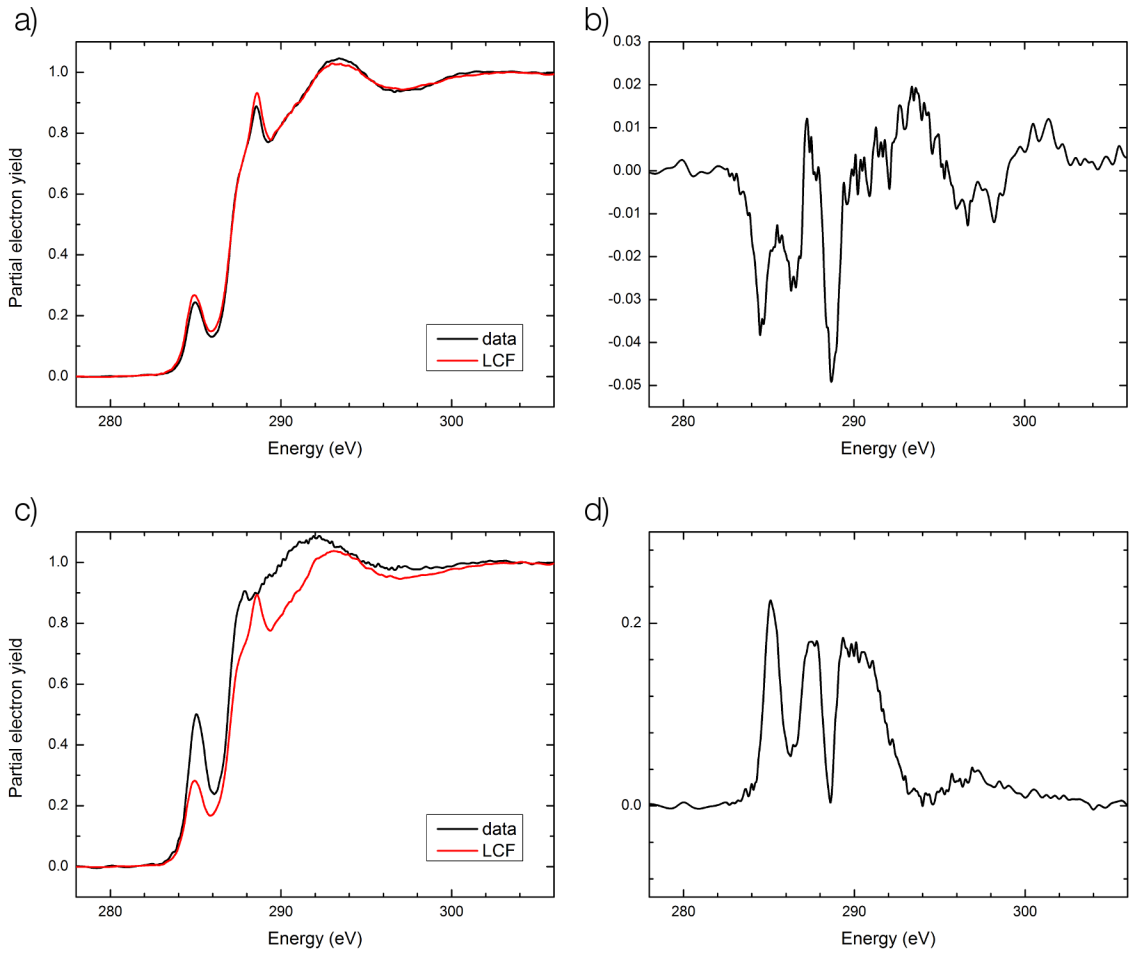

Figure 4.9: Initial linear combination fits of a) 30–50 nm MWCNT composite, obtained from spectra of polymer and CNT and b) its LCF residual, and of c) 60–100 nm MWCNT composite and d) its residual.

$$\mu_{\text{composite}}(E) = w_1\mu_{\text{MWCNT}}(E) + w_2\mu_{\text{matrix}}(E) + w_3\mu_{\text{interaction}}(E) \tag{4.7}$$

However, the residual cannot be meaningfully used as a third standard (representing the interaction) as is: assigned weights to matrix and filler spectra in the initial fit, which define the residual, are likely to be incorrect since the algorithm considered those two standards alone (equation 4.6). Spectral features in the residual therefore need to be decoupled to increase their degree of freedom.

Indeed, *a priori* knowledge of the system chemistry allows meaningful fitting of Lorentzians to the residual, each assigned to electronic transitions (Figure 4.10a). These individual resonances can now be appended as standards to obtain a new LCF. The fit is improved by an order of magnitude (Figure 4.10b, weights in Table 4.2). In addition to the possible electronic transitions given in Table 4.2, resonances in the energy range 287–290 eV may

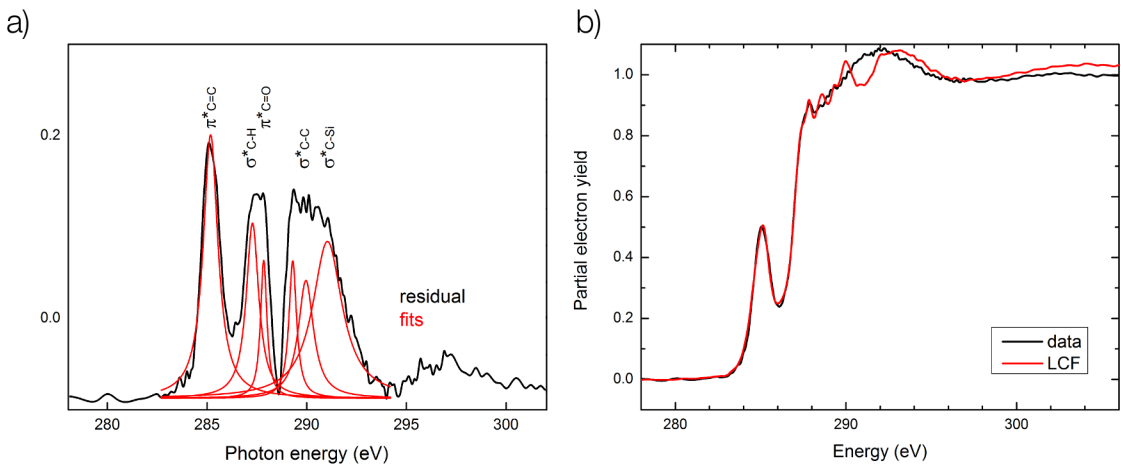

Figure 4.10: a) Five separate emissions deduced from LCF residual of 60–100 nm MWCNT composite; b) LCF obtained using fitted Lorentzians in addition to spectra of polymer and 60–100 nm MWCNTs.

also be indicative of CH—π interactions, one of the interaction models predicted earlier.[37]

This methodology has several limitations. The CNT standard is not directly representative of CNTs in composites for two reasons. Firstly, CNTs were dropcasted onto silicon, so any spectral feature related to orientation in the composite spectra is absent in the CNT spectrum. Secondly, CNTs in the composite are embedded in the polymer and therefore have significantly less accessibility than those in the drop-casted sample. Another limitation of this method is that any impurities in the samples are treated as real features by the algorithm and will be used to obtain a linear combination fit. This can be observed by comparing spectra of PDMS–PMMA, CNTs, and composites: emissions at 285 eV are attributed $1s \rightarrow \pi^*_{C=C}$ transitions but are present in the pure polymer blend. The LCA algorithm will therefore assign a greater weight to the CNTs to achieve a better fit at these energies.

Further, the algorithm as implemented in the Athena software package here begins to deteriorate, as the sum of the weights is not unity despite this restriction being explicit in the software. CNTs are still attributed a larger weight than expected with knowledge of their real weight percentage within composites. With a more robust implementation of LCA and a comprehensive library of standards (including angle-resolved acquisitions), this methodology may elucidate the fundamental interactions at the interface.

Table 4.2: LCF weights for 60–100 nm MWCNT composite. Fitted Lorentzians are referred to by their energy positions. *R*-factor = 0.0011.

Standard	Possible transitions	Weight
PDMS–PMMA	—	0.602
MWCNTs	—	0.436
285.2 eV	$1s \rightarrow \pi^*_{C=C}$	0.217
287.3 eV	$1s \rightarrow \sigma^*_{C-H}$	0.178
287.8 eV	$1s \rightarrow \pi^*_{C=O}$	0.221
289.3 eV	$1s \rightarrow \sigma^*_{C-C}$	0.187
290.0 eV	$1s \rightarrow \sigma^*_{C-C}$	0.367
291.0 eV	$1s \rightarrow \sigma^*_{C-Si}$	0.000

4.6 Summary

NEXAFS spectra revealed a complex interplay of intensities in phase-separated composites with strong orientational effects from unmodified MWCNTs. Filler alignment was observed in SEM images of individual fibres, making electrospinning a viable alignment solution in the synthesis of polymeric nanocomposites. Originally introduced as electrospinning carrier, phase segregation resulted in PMMA as a principle actor in filler adhesion. Intensity variations in spectra acquired at 20° suggested greater interactions in composites with larger CNTs, and promoted two conformational noncovalent bonding models. Both CH$-\pi$ and hydrogen models evidence increased interactions with larger MWCNTs having increased availability of π systems as well as impurity-related oxidized states.

Transient, compressive radial stress through the spinneret during electrospinning could enhance CNT-polymer interactions and, through local CNT deformations, promote mechanical interlocking. Effects of the specific role of electrospinning on CNT-polymer interactions are the subject of ongoing research.

Following the modified LCA procedure, information can be drawn from the relative importance of components in tandem with chemical data, and some of the most prominent bonding involved at the interface can be inferred. This is a first approach to quantifying and labelling interactions from experimental findings, and has several limitations. Conformational effects in nanocomposites may reduce availability of states, including those involved in crucial interactions; the library of standards for LCA may be lacking. This issue can be alleviated by extending the analysis to cover a suitable range of angle-resolved acquisitions,

or, alternatively, through less complex case studies.

Bibliography

[1] M. R. Diehl, S. N. Yaliraki, R. A. Beckman, M. Barahona, and J. R. Heath. Self-assembled, deterministic carbon nanotube wiring networks. *Angewandte Chemie International Edition*, **41**: 353–356, 2002.

[2] J. Chung, K.-H. Lee, J. Lee, and R. S. Ruoff. Toward large-scale integration of carbon nanotubes. *Langmuir*, **20**: 3011–3017, 2004.

[3] J. Hone, M. C. Llaguno, N. M. Nemes, A. T. Johnson, J. E. Fischer, D. A. Walters, M. J. Casavant, J. Schmidt, and R. E. Smalley. Electrical and thermal transport properties of magnetically aligned single wall carbon nanotube films. *Applied Physics Letters*, **77**: 666–668, 2000.

[4] T. Hertel, R. Martel, and P. Avouris. Manipulation of individual carbon nanotubes and their interaction with surfaces. *The Journal of Physical Chemistry B*, **102**: 910–915, 1998.

[5] L. Jin, C. Bower, and O. Zhou. Alignment of carbon nanotubes in a polymer matrix by mechanical stretching. *Applied physics letters*, **73**: 1197–1199, 1998.

[6] K. Jiang, Q. Li, and S. Fan. Nanotechnology: spinning continuous carbon nanotube yarns. *Nature*, **419**: 801–801, 2002.

[7] M. D. Lay, J. P. Novak, and E. S. Snow. Simple route to large-scale ordered arrays of liquid-deposited carbon nanotubes. *Nano Letters*, **4**: 603–606, 2004.

[8] D. Li, Y. Wang, and Y. Xia. Electrospinning of polymeric and ceramic nanofibers as uniaxially aligned arrays. *Nano Letters*, **3**: 1167–1171, 2003.

[9] M. V. Kakade, S. Givens, K. Gardner, K. H. Lee, D. B. Chase, and J. F. Rabolt. Electric Field Induced Orientation of Polymer Chains in Macroscopically Aligned Electrospun Polymer Nanofibers. *Journal of the American Chemical Society*, **129**: 2777–2782, 2007.

[10] J. Sidaravicius, R. Rinkūnas, J. Jurksus, T. Lozovski, I. Heiskanen, and K. Backfolk. Predicting the electrospinnability of polymer solutions with electromechanical simulation. *Journal of Applied Polymer Science*, **131**: 2014.

[11] J. Chen and J. A. Gardella. Solvent effects on the surface composition of poly (dimethylsiloxane)-co-polystyrene/polystyrene blends. *Macromolecules*, **31**: 9328–9336, 1998.

[12] H. Chen, X. Deng, X. Hou, R. Luo, and B. Liu. Preparation and Characterization of PDMS-PMMA Interpenetrating Polymer Networks with Indistinct Phase Separation. *Journal of Macromolecular Science, Part A: Pure and Applied Chemistry*, **46**: 83–89, 2009.

[13] N. S. Tambe and B. Bhushan. Micro/nanotribological characterization of PDMS and PMMA used for BioMEMS/NEMS applications. *Ultramicroscopy*, **105**: 238–247, 2005.

[14] D. Yang, X. Liu, Y. Jin, Y. Zhu, D. Zeng, X. Jiang, and H. Ma. Electrospinning of poly (dimethylsiloxane)/poly (methyl methacrylate) nanofibrous membrane: Fabrication and application in protein microarrays. *Biomacromolecules*, **10**: 3335–3340, 2009.

[15] A. D. Winter, E. Larios, F. M. Alamgir, C. Jaye, D. A. Fischer, and E. M. Campo. Near-edge x-ray absorption fine structure studies of electrospun poly (dimethylsiloxane)/poly (methyl methacrylate)/multiwall carbon nanotube composites. *Langmuir*, **29**: 15822–15830, 2013.

[16] D. Baskaran, J. W. Mays, and M. S. Bratcher. Noncovalent and nonspecific molecular interactions of polymers with multiwalled carbon nanotubes. *Chemistry of Materials*, **17**: 3389–3397, 2005.

[17] A. Llanes-Pallas, K. Yoosaf, H. Traboulsi, J. Mohanraj, T. Seldrum, J. Dumont, A. Minoia, R. Lazzaroni, N. Armaroli, and D. Bonifazi. Modular engineering of H-bonded supramolecular polymers for reversible functionalization of carbon nanotubes. *Journal of the American Chemical Society*, **133**: 15412–15424, 2011.

[18] Y. Liu, S. Chen, E. Zussman, C. S. Korach, W. Zhao, and M. Rafailovich. Diameter-dependent modulus and melting behavior in electrospun semicrystalline polymer fibers. *Macromolecules*, **44**: 4439–4444, 2011.

[19] T. Hemraj-Benny, S. Banerjee, S. Sambasivan, M. Balasubramanian, D. Fischer, G. Eres, A. A. Puretzky, D. B. Geohegan, D. H. Lowndes, W. Han, J. A. Misewich, and S. S. Wong. Near-Edge X-ray Absorption Fine Structure Spectroscopy as a Tool for Investigating Nanomaterials. *Small*, **2**: 26–35, 2006.

[20] E. Najafi, D. H. Cruz, M. Obst, A. P. Hitchcock, B. Douhard, J.-J. Pireaux, and A. Felten. Polarization Dependence of the C 1s X-ray Absorption Spectra of Individual Multi-Walled Carbon Nanotubes. *Small*, **4**: 2279–2285, 2008.

[21] V. Lee, C. Park, C. Jaye, D. A. Fischer, Q. Yu, W. Wu, Z. Liu, J. Bao, S.-S. Pei, C. Smith, P. Lysaght, and S. Banerjee. Substrate hybridization and rippling of graphene evidenced by near-edge X-ray absorption fine structure spectroscopy. *The Journal of Physical Chemistry Letters*, **1**: 1247–1253, 2010.

[22] B. J. Schultz, C. J. Patridge, V. Lee, C. Jaye, P. S. Lysaght, C. Smith, J. Barnett, D. A. Fischer, D. Prendergast, and S. Banerjee. Imaging local electronic corrugations and doped regions in graphene. *Nature communications*, **2**: 372, 2011.

[23] K. Efimenko, W. E. Wallace, and J. Genzer. Surface modification of Sylgard-184 poly (dimethyl siloxane) networks by ultraviolet and ultraviolet/ozone treatment. *Journal of colloid and interface science*, **254**: 306–315, 2002.

[24] O. Dhez, H. Ade, and S. G. Urquhart. Calibrated NEXAFS spectra of some common polymers. *Journal of Electron Spectroscopy and Related Phenomena*, **128**: 85–96, 2003.

[25] M. Harris, G. Appel, and H. Ade. Surface morphology of annealed polystyrene and poly (methyl methacrylate) thin film blends and bilayers. *Macromolecules*, **36**: 3307–3314, 2003.

[26] L. Fleming, M. D. Ulrich, K. Efimenko, J. Genzer, A. S. Y. Chan, M. T. E, S. J. Oh, and J. E. Rowe. Near-edge absorption fine structure and UV photoemission spectroscopy studies of aligned single-walled carbon nanotubes on Si (100) substrates. *Journal of Vacuum Science & Technology B: Microelectronics and Nanometer Structures*, **22**: 2000–2004, 2004.

[27] A. Göldel, G. Kasaliwal, and P. Pötschke. Selective Localization and Migration of Multiwalled Carbon Nanotubes in Blends of Polycarbonate and Poly (styrene-acrylonitrile). *Macromolecular rapid communications*, **30**: 423–429, 2009.

[28] J. Brandup, E. H. Immergut, and E. A. Grulke. *Polymer handbook*. vol. 89 Wiley, New York, 1989. 213

[29] S. Wu. "Calculation of interfacial tension in polymer systems" in: *Journal of Polymer Science Part C: Polymer Symposia*. vol. 34 1 Wiley Online Library 1971. 19–30

[30] S. Nuriel, L. Liu, A. H. Barber, and H. D. Wagner. Direct measurement of multiwall nanotube surface tension. *Chemical Physics Letters*, **404**: 263–266, 2005.

[31] G. D. Andreetti, R. Ungaro, and A. Pochini. Crystal and molecular structure of cyclo {quater [(5-t-butyl-2-hydroxy-1, 3-phenylene) methylene]} toluene (1:1) clathrate. *Journal of the Chemical Society, Chemical Communications*, **22**: 1005–1007, 1979.

[32] G. Klopman. *Chemical Reactivity and Reaction Paths*. New York: Wiley-Interscience, 1974.

[33] M. Nishio, M. Hirota, and Y. Umezawa. *The CH/π interaction: evidence, nature, and consequences*. vol. 21 John Wiley & Sons, 1998.

[34] G. Aragay, D. Hernández, B. n. Verdejo, E. C. Escudero-Adán, M. Martínez, and P. Ballester. Quantification of CH-π Interactions Using Calix [4] pyrrole Receptors as Model Systems. *Molecules*, **20**: 16672–16686, 2015.

[35] I. Fleming. *Molecular Orbitals and Organic Chemical Reactions*. 2nd ed. John Wiley & Sons Ltd: London, UK, 2009.

[36] E. Jiménez-Moreno, A. M. Gómez, A. Bastida, F. Corzana, G. Jiménez-Oses, J. Jiménez Barbero, and J. L. Asensio. Modulating Weak Interactions for Molecular Recognition: A Dynamic Combinatorial Analysis for Assessing the Contribution of Electrostatics to the Stability of CH–π Bonds in Water. *Angewandte Chemie*, **127**: 4418–4422, 2015.

[37] N. Kocharova, J. Leiro, J. Lukkari, M. Heinonen, T. Skála, F. Šutara, M. Skoda, and M. Vondrácek. Self-assembled carbon nanotubes on gold: polarization-modulated infrared reflection-absorption spectroscopy, high-resolution X-ray photoemission spectroscopy, and near-edge x-ray absorption fine structure spectroscopy study. *Langmuir*, **24**: 3235–3243, 2008.

[38] M. C. Urbina, S. Zinoveva, T. Miller, C. M. Sabliov, W. T. Monroe, and C. S. S. R. Kumar. Investigation of Magnetic Nanoparticle-Polymer Composites for Multiple-controlled Drug Delivery. *The Journal of Physical Chemistry C*, **112**: 11102–11108, 2008.

[39] M. Bonne, D. Sellam, J.-P. Dacquin, A. F. Lee, K. Wilson, L. Olivi, A. Cognigni, P. Marécot, S. Royer, and D. Duprez. A general route to synthesize supported isolated oxide and mixed-oxide nanoclusters at sizes below 5 nm. *Chemical Communications*, **47**: 1509–1511, 2011.

[40] M. F. Lengke, B. Ravel, M. E. Fleet, G. Wanger, R. A. Gordon, and G. Southam. Mechanisms of gold bioaccumulation by filamentous cyanobacteria from gold (III)-chloride complex. *Environmental science & technology*, **40**: 6304–6309, 2006.

[41] F. Meirer, J. Cabana, Y. Liu, A. Mehta, J. C. Andrews, and P. Pianetta. Three-dimensional imaging of chemical phase transformations at the nanoscale with full-field transmission X-ray microscopy. *Journal of synchrotron radiation*, **18**: 773–781, 2011.

[42] A. Jain, S. P. Ong, G. Hautier, W. Chen, W. D. Richards, S. Dacek, S. Cholia, D. Gunter, D. Skinner, G. Ceder, and K. A. Persson. Commentary: The Materials Project: A materials genome approach to accelerating materials innovation. *APL Materials*, **1**: 011002, 2013.

Chapter 5

EVA|MWCNT composites: Thermoactive behaviour

5.1 Introduction

The direct conversion of thermal or optical energy to mechanical energy is critically important, offering desirable advantages over electrically driven actuators, such as remote controllability, wireless actuation, low noise, and electromechanical decoupling,[1] attracting interest from a myriad of fields, from ultrafast optical switches in MOEMS to artificial muscles for human implants.[2,3] However, this behaviour has only been observed for a few material systems.[4–6]

Recently, carbon nanotubes have shown to exhibit active properties when embedded in polymeric matrices, and large, fast, and reversible mechanical actuation has been reported.[7–10] 'Smart' behaviour in polymer nanocomposites has only been studied at the macroscale, however, and the development and deployment of smart devices is hindered by a lack of understanding of the underlying mechanisms. Although tentative explanations have been proposed, there is currently no unified molecular model for this behaviour.[10–12]

Despite this lack of understanding, it has been experimentally shown that nanofiller

[1] S. Lu and B. Panchapakesan. *Nanotechnology*, **18**: 305502, 2007.
[2] R. H. Baughman et al. *Science*, **284**: 1340–1344, 1999.
[3] L. Ionov. *J. Mater. Chem.*, **20**: 3382–3390, 2010.
[4] K. Takagi et al. *J. Am. Ceram. Soc.*, **87**: 1477–1482, 2004.
[5] P. M. Hogan, A. R. Tajbakhsh, and E. M. Terentjev. *Phys. Rev. E*, **65**: 041720, 2002.
[6] J. Suski et al. *Sens. Actuators A*, **24**: 221–225, 1990.
[7] H. Koerner et al. *Nat. Mater.*, **3**: 115–120, 2004.
[8] S. V. Ahir and E. M. Terentjev. *Nat. Mater.*, **4**: 491–495, 2005.
[9] J. Loomis et al. *Nanotechnology*, **23**: 045501, 2012.
[10] K. Czaniková et al. *J. Nanophotonics*, **6**: 810707, 2011.
[11] S. V. Ahir and E. M. Terentjev. *Phys. Rev. Lett.*, **96**: 133902–133904, 2006.
[12] R. Vaia. *Nature Mater.*, **4**: 429–430, 2005.

alignment is crucial for the final mechanical output. Indeed, in the case of MWCNT|PDMS nanocomposites, Ahir and coworkers demonstrated that the level of CNT alignment defines whether the response is contractive or expansive.[8] Although the previous chapter highlighted the viability of electrospinning for achieving alignment and dispersion in polymer nanocomposites, the range of polymers reported to have been electrospun is limited. For this reason, alternative, more universal synthesis techniques must be discussed. This chapter reports on the *in situ* temperature-resolved NEXAFS of photo- and thermoactive ethylene vinyl acetate (EVA)|MWCNT composites, with the aim of correlating spectral observations to macroscopic active behaviour.[13] Nanofiller dispersion is assisted by noncovalent functionalisation of CNTs with a novel dispersant, and alignment is promoted through application of uniaxial strain during composite fabrication.

5.2 Experimental

5.2.1 Materials and reagents

Commercial ethylene vinyl acetate copolymer (Evatane 28025, Arkema, France)—shown in Figure 5.1a—containing 28 wt% vinyl acetate, and chloroform ($CHCl_3$, Mikochem, Slovakia) were used as matrix and solvent, respectively. MWCNTs with diameters of 60–100 nm and lengths of 5–15 μm were purchased from Nanostructured & Amorphous Materials, Inc (Houston, Texas, USA), and dispersion was achieved through cholesteryl 1-pyrenecarboxylate (PyChol), a novel dispersant whose synthesis is described elsewhere.[10]

5.2.2 Nanocomposite fabrication

Following previously reported procedures,[10] a 1:5 weight ratio of MWCNT/PyChol was dispersed in 100 ml of chloroform, and sonicated for 1 hour under magnetic stirring with a Hielscher 400 S sonicator at an amplitude of 20% (∼35 μm, ∼60 Wcm^{-2}) and continuous operation mode i.e. 100% duty cycle. This resulted in noncovalent functionalisation of MWCNTs with PyChol molecules through π–π interactions between the pyrene groups in the dispersant and the CNT graphitic walls (Figure 5.1b). Cholesteryl groups in PyChol were designed to act as 'spacers' and prevent π–π interactions amongst adjacent CNTs, assisting dispersion. Following sonication, 10 g of EVA were added, and the final solution was magnetically stirred for several hours. The solution was subsequently poured into a Teflon-coated Petri dish and dried at laboratory temperature for 12 hours prior to gradual

[13] A. D. Winter et al. *J. Phys. Chem. C*, **118**: 3733–3741, 2014.

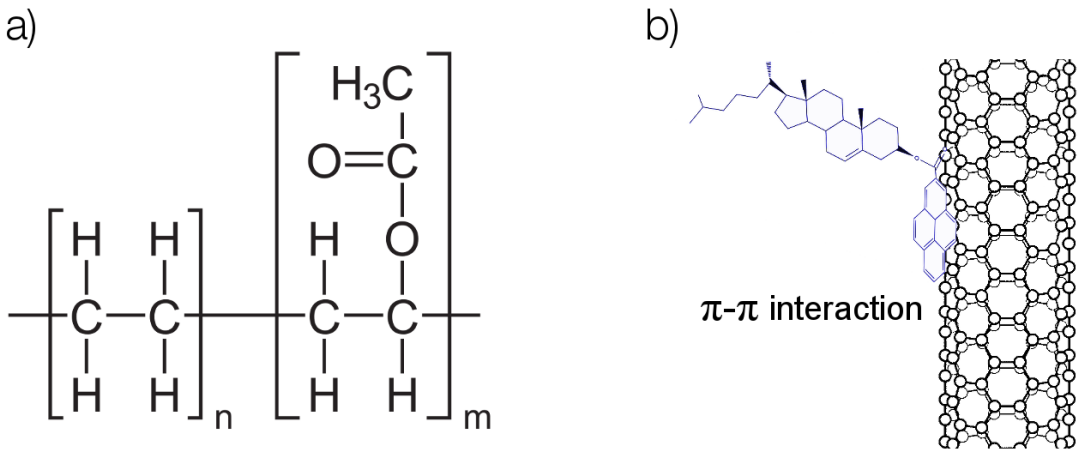

Figure 5.1: a) EVA block copolymer; b) noncovalent functionalisation of MWCNTs with PyChol through π-π interactions.

oven drying at 40, 60 and 70 °for several hours. Finally, composites were placed in a vacuum oven for 6 hours at 70 °C. Composite films were then compression-moulded in a laboratory press (Fontijne SRA 100, The Netherlands) for 15 min under a pressure of 2.5 MPa and a temperature of 80 °C. The pressed composite samples were strained up to 50% at 50 °C for 20 min using a custom-made stretching apparatus. Subsequently, the stretched samples were cooled in ice water to fix the orientation of CNTs. Two EVA|MWCNT (0.7 wt%) composites were prepared following this procedure: one unstrained, and one with 50% strain. Pristine PyChol, EVA, and dropcast MWCNTs were also used for building-block NEXAFS analysis.

5.2.3 *In situ* temperature-resolved NEXAFS spectroscopy

Carbon *K*-edge spectra were collected at the NIST beamline U7A (NSLS, BNL) in partial electron yield (PEY) mode using a horizontally polarised beam, with an energy resolution of ~0.1 eV and a spot size of 2 mm × 2 mm. Sample charging was prevented via the use of an electron floodgun operating at 60 μA.

For *in situ* temperature studies, samples were secured with a vauum-safe epoxy (Torr-seal) on a tantalum metal plate inserted on a customised heating stage (Figure 5.2). The stage angle was controlled by a goniometer, and the termperature was controlled by a voltage supply. Temperature oscillations were observed as ± 1.5 °C of the set point. Genzer and co-workers have published more exhaustive details on the *in situ* capabilities of the beamline.[14] The strained composite was mounted with the strain direction perpendicular to the beam polarisation. Spectra were acquired at magic angle (55°) by sequentially running

[14] J. Genzer et al. *Langmuir*, **16**: 1993–1997, 2000.

Figure 5.2: Samples mounted on heating stage for NEXAFS characterisation.

macros that controlled the coordinates of the stage and specified the energy parameters. The temperature sequence was 30, 35, 38, 42, and 48 °C.

The PEY signals were normalised to the incident beam intensity using the photoemission signal from a freshly evaporated gold mesh located along the incident beam path. Spectra were energy-calibrated using the photoemission current from an amorphous carbon mesh also located along the path of the incident beam. Spectra were calibrated and normalised using standard routines from the Athena software package.[15]

5.3 Spectral identification

NEXAFS spectra of composites (0% and 50% strain) and individual constituents (pristine EVA, MWCNT, PyChol dispersant) were acquired at room temperature at magic incidence (50°), and are plotted in Figure 5.3. All resonances and attributed electronic transitions are presented in Table 5.1. Both PyChol dispersant and MWCNTs share resonance at 285 eV, corresponding to $1s \rightarrow \pi^*_{C=C}$ transitions in pyrene groups in PyChol, and graphitic walls in MWCNTs. PyChol shows an additional $\pi^*_{C=C}$ resonance at 284.2 eV. A similar feature is observed in EVA, attributed to surficial carbonaceous impurities—the same impurities were observed in pristine PDMS-PMMA blends in Chapter 4.

It is clear that the NEXAFS spectrum of unstrained composite is a linear combination of the individual constituents' spectral fingerprints. Remarkably, strained composite is spectrally quite different. These differences are attributed to conformational effects, since the chemistry in both systems is identical. Firstly, the lower-energy $1s \rightarrow \pi^*_{C=C}$ transition resonance at 284.2 eV (originating from PyChol) is not visible in the strained composite. This feature is probably

[15] B. Ravel and M. Newville. *J. Synchrotron Radiat.*, **12**: 537–541, 2005.

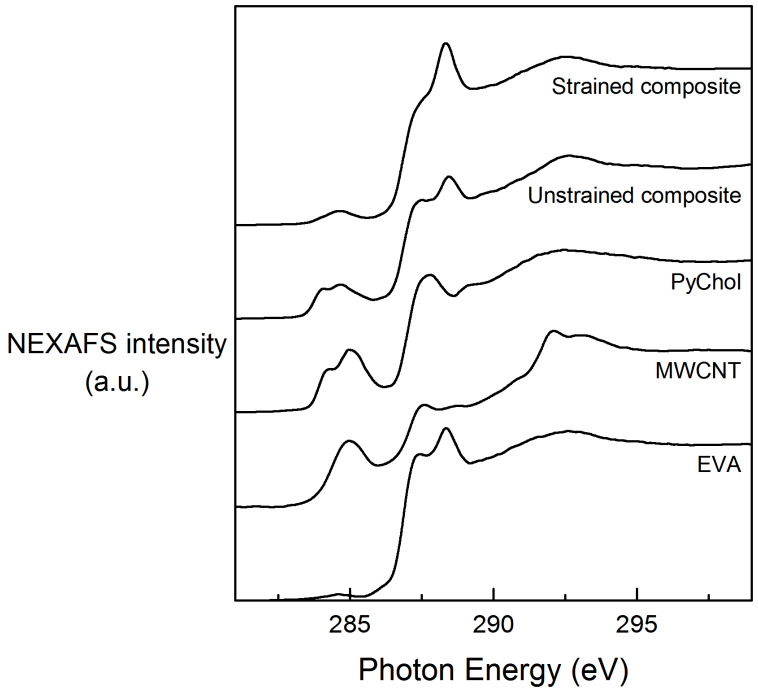

Figure 5.3: Carbon *K*-edge NEXAFS spectra of composites and constituents.

arising from the C=C bond within the cholesteryl group in PyChol, which has more degrees of freedom (the pyrene group is bound to CNT graphitic walls), and therefore can be dragged as the system is uniaxially strained, becoming inaccessible to the beam. Indeed, the difference in energy between this feature and the main $\pi^*_{C=C}$ resonance is indicative of a different chemical environment:[16] whilst both transitions indicate the presence of sp^2 hybridised carbon atoms, absorbing atoms in the benzene-like pyrene group and in the cholesteryl group are bound to different structures. Note that the apparent reduction in $\pi^*_{C=C}$ intensity at 285 eV is partially explained by the absence of this lower-energy resonance, as both features—when present—are convoluted producing a higher overall intensity. Further intensity decrease could result from CNT alignment, where a higher amount of π^* vectors (normal to the CNT surface) are rendered parallel to the incoming electric field: the resulting overlap between the polarised electric field (parallel to CNT surface) and the π system is decreased owing to the orbital geometry of the latter, thus diminishing the $\pi^*_{C=C}$ intensity detected by NEXAFS.

Secondly, the resonance at 289.1 eV, attributed to $1s \rightarrow \pi^*_{C=O}$ transitions, is significantly more intense in the strained composite spectrum, causing the σ^*_{C-H} resonance at 287.7 eV to appear as a shoulder. This is likely to be caused by an enhanced alignment of C=O

[16] G. Hähner. *Chem. Soc. Rev.*, **35**: 1244–1255, 2006.

Table 5.1: NEXAFS resonances from Figure 5.3 and their attributed electronic transitions.

Energy (eV)	Transition
284.2	$1s \rightarrow \pi^*_{C=C}$ [a]
285.0	$1s \rightarrow \pi^*_{C=C}$ [b]
287.7	$1s \rightarrow \sigma^*_{C-H}$
289.1	$1s \rightarrow \pi^*_{C=O}$
292.0	$1s \rightarrow \sigma^*_{C-C}$

[a] Emission from cholesteryl group in PyChol.

[b] Emission from CNTs and pyrene group in PyChol.

groups from EVA chains around CNTs, whose alignment is the primary goal of straining the composite.

5.4 Nanoparticle dispersion and alignment

Molecular homogeneity within composites was confirmed by acquiring NEXAFS spectra at different sample locations (Figure 5.4), which do not reveal any significant spectral variation. Although this is not a direct measure of filler dispersion, as the beam diameter is 2 mm, it demonstrates consistent composite chemistry achieved by sonication of nanotubes and noncovalent functionalisation with PyChol at this lengthscale, as well as homogeneous strain.

As mentioned earlier, composites were strained to 50% to achieve CNT alignment. The polarisation dependence of intensities of CNT Raman bands is well established;[17] to assess the degree of strain-induced alignment, polarised Raman spectra of both composites were acquired with strain direction parallel and perpendicular to beam polarisation vector (Figure 5.5). Spectra show typical D and G bands at 1336 and 1858 cm^{-1}, commonly interpreted as indicative of disorder or damage, and graphitic sp^2 crystallinity in CNTs, respectively.[18] The additional bands in composite spectra at 1302 and 1439 cm^{-1} have been attributed to CH_2 twisting and scissoring vibrational modes in EVA.[19] Intensity ratios of $D_{\parallel}/D_{\perp}$ and $G_{\parallel}/G_{\perp}$ of 1 are expected for complete CNT isotropy; increasing ratios indicate increased anisotropy, or alignment.[20]

[17] R. Saito et al. *Phys. Rev. B*, **57**: 4145, 1998.

[18] M. S. Dresselhaus et al. *Nano Lett.*, **10**: 751–758, 2010.

[19] M. Shimoyama et al. *Vib. Spectrosc.*, **14**: 253–259, 1997.

[20] S. Abbasi, P. J. Carreau, and A. Derdouri. *Polymer*, **51**: 922–935, 2010.

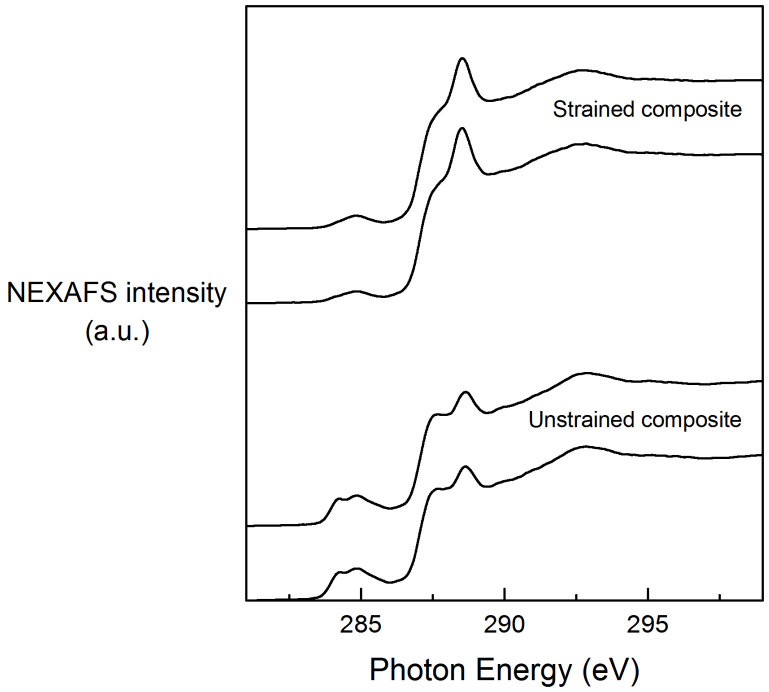

Figure 5.4: NEXAFS acquisitions of composites from two different locations in samples shows molecular homogeneity.

Table 5.2: Polarised Raman spectroscopy ratios indicate increased alignment in strain composite.

Composite	$D_{\parallel}/D_{\perp}$	$G_{\parallel}/G_{\perp}$
Unstrained	1.10	1.10
Strained	1.37	1.34

Intensities in unstrained composite spectrum yield $D_{\parallel}/D_{\perp}$ and $G_{\parallel}/G_{\perp}$ ratios of 1.1 (Table 5.2), suggesting, as expected, very little alignment. An increased alignment was indeed achieved in strained composite. In fact, the ratios are comparable to the alignment achieved by micro-injection compression moulding reported by Abbasi and coworkers.[20]

5.5 Actuation: Temperature-resolved NEXAFS analysis

In situ temperature-resolved NEXAFS spectra of EVA|MWCNT composites offer insights into the molecular phenomena which ultimately give rise to macroscopic actuation. Spectral acquisitions recorded at increasing composite temperature show a synchronous intensity

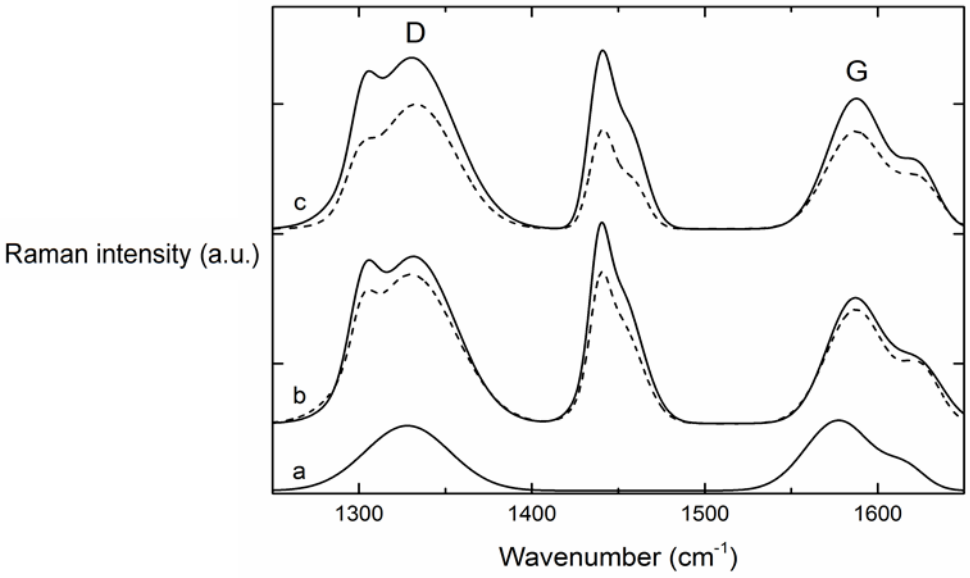

Figure 5.5: a) Raman spectra from drop-casted MWCNTs on Si; polarised Raman spectra of b) unstrained and c) strained composites, acquired with strain direction parallel (solid line) and perpendicular (dashed line) to the electric field.

interplay, where $\pi^*_{C=C}$ intensities increase and $\pi^*_{C=O}$ intensities decrease (Figure 5.6). Further, the magnitude of this effect is considerably larger in strained composite, consistent with macroscopic observations:[10] this suggests that CNT alignment is a key factor during actuation.

Using similar arguments as earlier, the temperature variation used here (30–48 °C) will not affect the composite chemistry (reported values for transition T_g and melting temperature T_m for EVA are -28 and 83 °C respectively);[21] the seemingly coupled intensity interplay can therefore be attributed to conformational effects.

Further investigation of temperature-derived trends is possible by plotting the relative intensity changes for both $\pi^*_{C=C}$ and $\pi^*_{C=O}$ resonances with respect to room temperature, calculated here as $(I_t - I_{RT})/I_{RT}$ (Figure 5.7). These intensities have been corrected for the background carbonaceous impurities in EVA (Figure 5.3), and the error bars represent the error propagation associated with this correction and other post-processing. The trends are reasonably linear, and the coupling between intensity temperature variation trends (T_v) can be described by equation 5.1.

$$T_{V(C=C)} = -x T_{V(C=O)} \tag{5.1}$$

[21] J. Komornicki et al. *J. Adhes. Sci. Technol.*, **6**: 293–305, 1992.

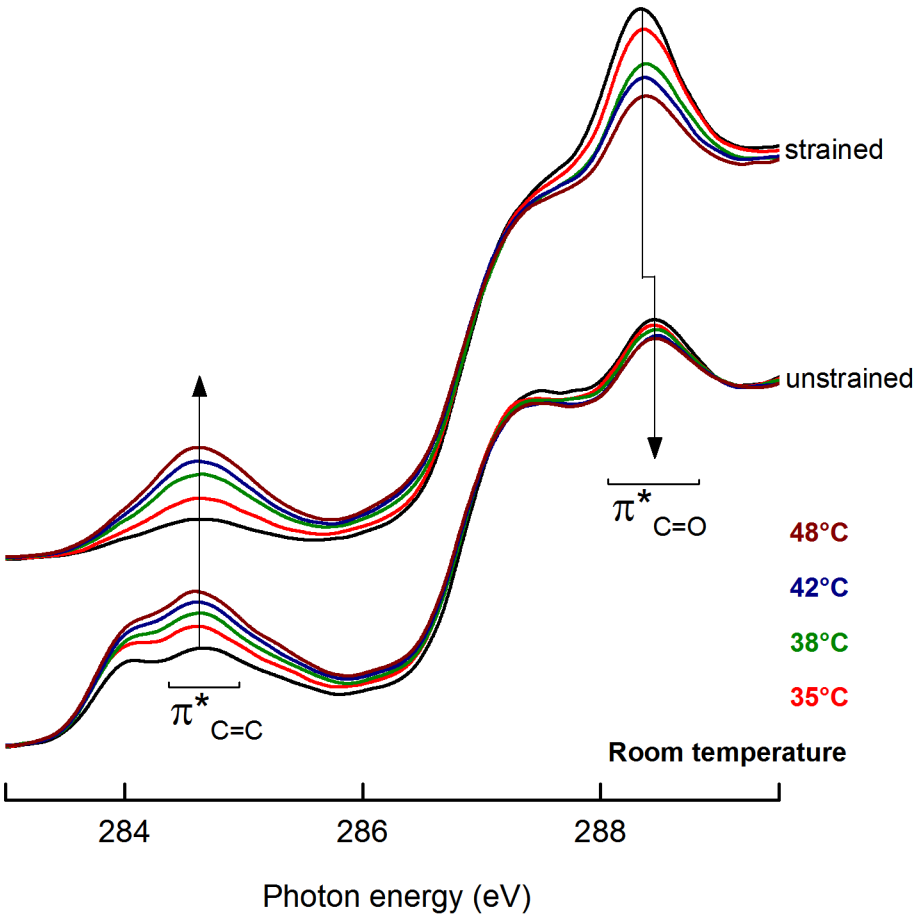

Figure 5.6: Synchronous intensity interplays observed for $\pi^*_{C=C}$ and $\pi^*_{C=O}$ in *in situ* temperature-resolved NEXAFS spectra.

$$T_{V(strained)} = y\,T_{V(unstrained)} \tag{5.2}$$

With this description, $\pi^*_{C=C}$ and $\pi^*_{C=O}$ intensities in strained composite are coupled by a factor of 10 ($x_{strained} = 10$). Unstrained composites show a coupling twice as weak, with $x_{unstrained} = 5$. Additionally, comparing T_v of either $\pi^*_{C=C}$ or $\pi^*_{C=O}$ in both composites (equation 5.2) reveals a greater sensitivity to temperature in strained system, with $y_{C=C} = 7$ and $y_{C=O} = 4$.

Raman and NEXAFS spectroscopies confirm that the applied uniaxial strain aligns both CNTs and polymeric chains, and this is expected to enhance actuation. Indeed, aligned CNTs provide more direct conductivity pathways across the entire composite thickness, and

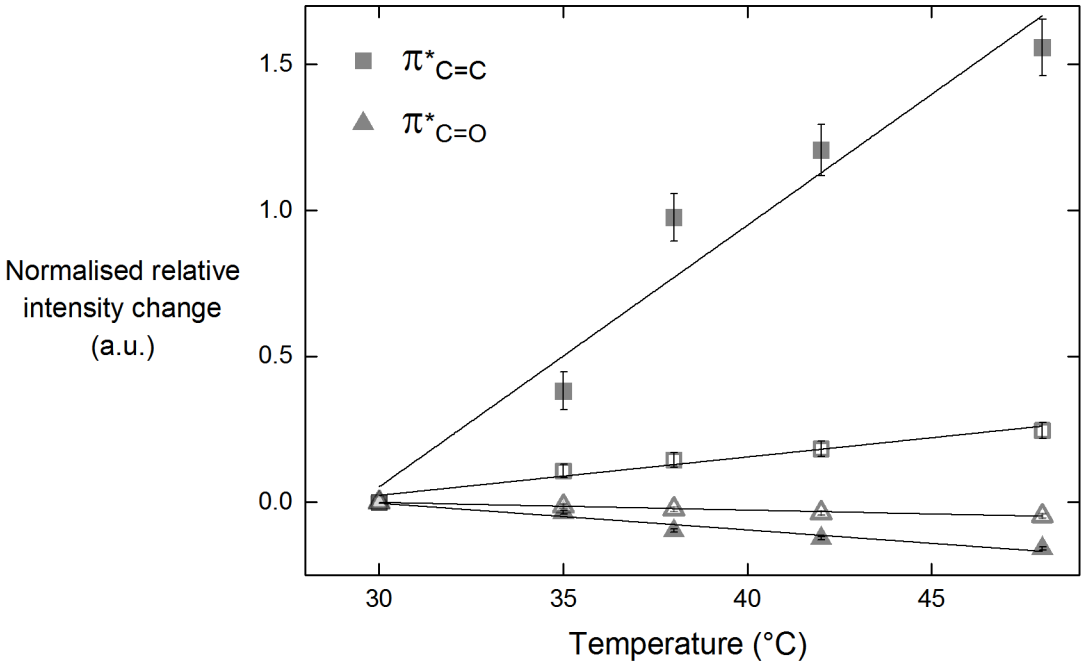

Figure 5.7: Relative intensity changes of $\pi^*_{C=C}$ and $\pi^*_{C=O}$ resonances show linear trends ($y = mx + c$), where m and c are 0.089 and -2.64, -0.0091 and 0.27, 0.0131 and -0.37, and -0.0026 and 0.078 for $\pi^*_{C=C}$ strained, $\pi^*_{C=O}$ strained, $\pi^*_{C=C}$ unstrained, and $\pi^*_{C=O}$ unstrained respectively. Filled symbols correspond to strained composite, empty symbols to unstrained composite.

therefore thermal conductivity is expected to increase,[22] and this could directly enhance the macroscopic response.[10] As proposed earlier, temperature dependent intensities are reflections of molecular conformational phenomena, since the temperature variations are too small to result in chemical changes. To further this argument, NEXAFS spectra of strained composite were acquired at normal, magic and glancing incidences at both extreme temperatures: room temperature (30 °C) and 48 °C (Figure 5.8). The most apparent difference between these two points lies in the $\pi^*_{C=O}$ resonance.

At room temperature, both $\pi^*_{C=C}$ and $\pi^*_{C=O}$ resonances display an intensity angular dependence. Although the variation in $\pi^*_{C=C}$ is small, it further confirms the strain-induced CNT alignment. It is, however, the $\pi^*_{C=O}$ intensity variation that is more revealing. It suggests a preferred orientation of C=O pendant groups in EVA relative to nanotube axis.

The angular-dependence of $\pi^*_{C=C}$ resonances is still observed at 48 °C, when the system is active, but absolute intensities are higher under all incidence angles. Conversely, $\pi^*_{C=O}$ resonances no longer show angular dependence, indicating a transition to isotropic dis-

[22] A. M. Marconnet et al. *ACS Nano*, **5**: 4818–4821, 2011.

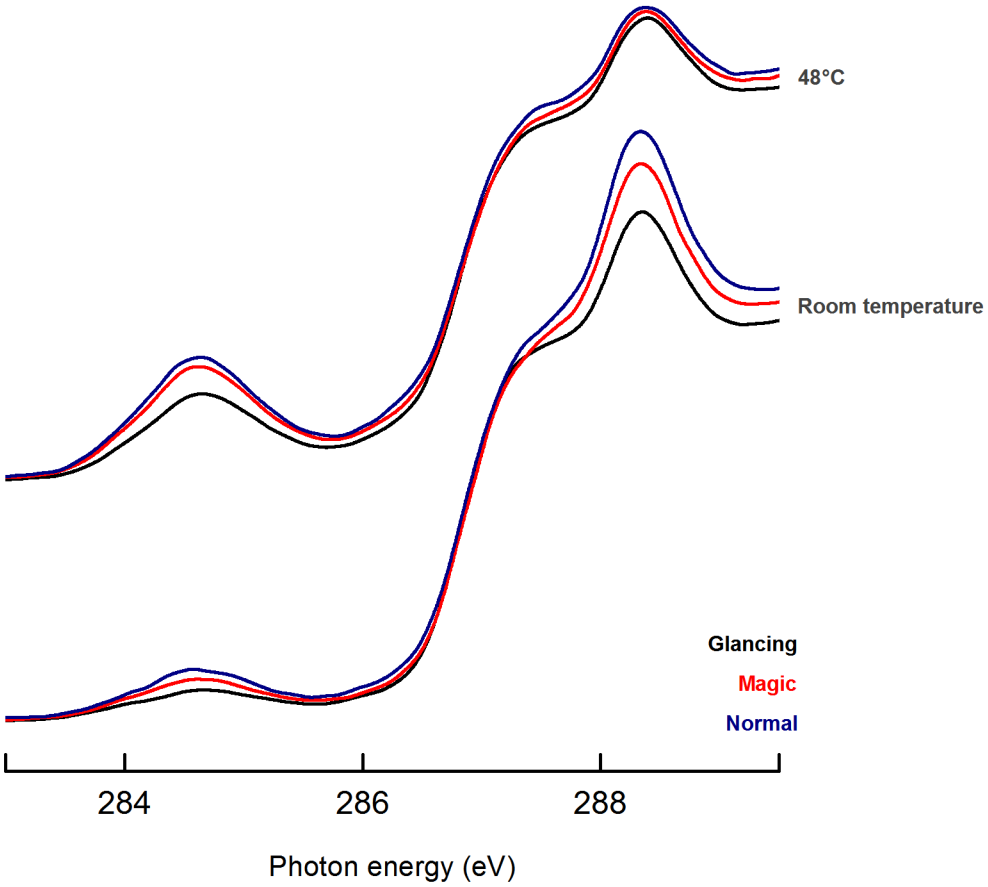

Figure 5.8: Angular dependency of $\pi^*_{C=O}$ intensities in strained composite at room temperature is lost at 48 °C, indicating a transition from anisotropic to isotropic configuration of C=O groups.

tribution. These observations may be explained by CNTs experiencing torsional perturbations with increasing temperature whilst maintaining their overall alignment.[8,11]

5.6 Actuation model

In the proposed model in Figure 5.9, CNTs are assumed to lie preferentially on the xy plane and the beam is incident on the z axis with its polarisation vector along the x axis. Note that PyChol is not included in the discussion as its role is purely as dispersant; indeed, active behaviour has been observed in systems where chemical dispersants were not used.[8]

In the relaxed state, EVA chains are appended to aligned CNTs through CH—π interac-

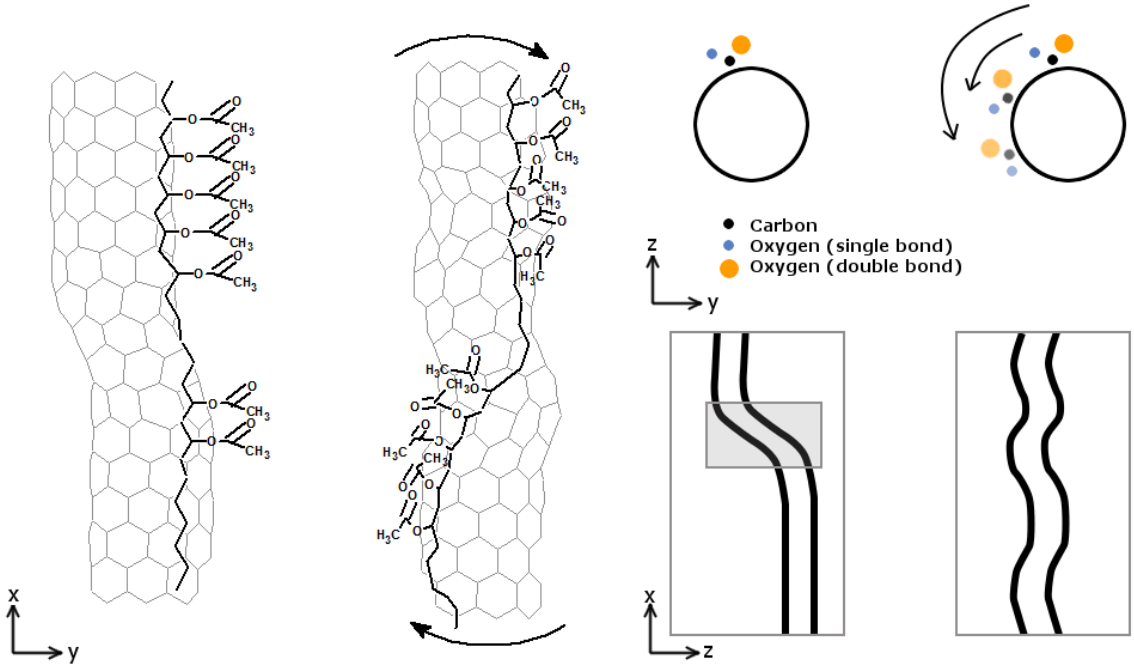

Figure 5.9: In this proposed model, carbon nanotubes experience a torsion along as-grown defects, disturbing the uniform alignment of C=O groups in EVA, and enhancing uniaxial symmetry. NEXAFS beam travels along z axis with electric field vector along x axis. Each plane shows relaxed and excited states: left and right respectively.

tions, with pendant C=O groups in a preferred uniform arrangement with respect to CNT axes.[23,24] Despite the strain-induced alignment, CNTs still have natural kinks and imperfections from growth and processing.

Upon actuation under increasing temperature, CNTs could experience torsion and buckling which would break the orientation of C=O groups and render them isotropic (Figure 5.8).[25] This would result in the gradual decrease of $\pi^*_{C=O}$ intensity in temperature-resolved NEXAFS spectra. Further, this torsion would also enhance the uniaxial symmetry of the CNT-polymer ensamble, as shown in the xz plane in Figure 5.9: in fact, the π^* orbitals represented within the shaded rectangle—priorly inaccessible to the beam along the z axis—would become visible as this CNT torsion progresses, increasing the $\pi^*_{C=C}$ contribution (and therefore overall intensity) in NEXAFS.

The nature of the torsional deformation in CNTs is still unclear, but Ahir and coworkers suggested that active behaviour of nanocomposites originates from nanotube units inde-

[23] A. Beigbeder et al. *Adv. Mater.*, **20**: 1003–1007, 2008.
[24] S. L. Teh, D. Linton, and M. D. Dadmun. *Macromolecules*, **44**: 7737–7745, 2011.
[25] Y. Y. Zhang, C. M. Wang, and V. B. C. Tan. *Nanotechnology*, **20**: 215702, 2009.

pendently of host matrix.[26] It has also been previously reported that buckling is necessary to explain macroscopic contractions of up to 15%,[12] which concept attracted interest for CNT-based artificial muscles.[27,28]

Finally, as this model considers only one CNT, a degree of alignment would be needed to translate the behaviour to the macroscale. This could explain the increasing macroscopic response as alignment increases, as well as the prior trend discussion.[11]

5.7 Summary

This chapter documented the *in situ* temperature-resolved NEXAFS studies of photo- and thermoactive EVA|MWCNT nanocomposites. The 50% uniaxial strain induced filler alignment, as revealed by $D_{\parallel}/D_{\perp}$ and $G_{\parallel}/G_{\perp}$ intensity ratios in Raman spectroscopy. NEXAFS spectra of strained composite also confirmed filler alignment, as well as enhanced anisotropy of polymeric C=O groups, suggesting an overall alignment of EVA chains. Repeated NEXAFS acquisitions from different locations in both unstrained and strained composites implied sufficient nanofiller dispersion, undoubtedly assisted by sonication and noncovalent PyChol functionalisation.

Temperature-resolved scans revealed inversely proportional intensity variations of $\pi^*_{C=C}$ and $\pi^*_{C=O}$ resonances (indicators of CNTs and EVA chains respectively), suggesting conformational behaviour. This trend was considerably more accentuated in strained composites, where CNTs and polymeric chains were more aligned. Active behaviour was modelled as torsion of CNTs upon irradiation, increasing uniaxial symmetry of CNT-polymer systems. The model also addressed the importance of CNT alignment, which would facilitate the constructive translation of molecular phenomena to the macroscale as mechanical actuation.

[26] S. V. Ahir, Y. Y. Huang, and E. M. Terentjev. *Polymer*, **49**: 3841–3854, 2008.
[27] J. Foroughi et al. *Science*, **334**: 494–497, 2011.
[28] M. D. Lima et al. *Science*, **338**: 928–932, 2012.

Bibliography

[1] S. Lu and B. Panchapakesan. Photomechanical responses of carbon nanotube/polymer actuators. *Nanotechnology*, **18**: 305502, 2007.

[2] R. H. Baughman, C. X. Cui, A. A. Zakhidov, Z. Iqbal, and J. N. Barisci. Carbon nanotube actuators. *Science*, **284**: 1340–1344, 1999.

[3] L. Ionov. Actively-moving materials based on stimuli-responsive polymers. *Journal of Materials Chemistry*, **20**: 3382–3390, 2010.

[4] K. Takagi, S. Kikuchi, J.-F. Li, H. Okamura, R. Watanabe, and A. Kawasaki. Ferroelectric and Photostrictive Properties of Fine-Grained PLZT Ceramics Derived from Mechanical Alloying. *Journal of the American Ceramic Society*, **87**: 1477–1482, 2004.

[5] P. M. Hogan, A. R. Tajbakhsh, and E. M. Terentjev. UV manipulation of order and macroscopic shape in nematic elastomers. *Physical Review E*, **65**: 041720, 2002.

[6] J. Suski, D. Largeau, A. Steyer, F. C. M. Van de Pol, and F. R. Blom. Optically activated ZnO/Sio 2/Si cantilever beams. *Sensors and Actuators A: Physical*, **24**: 221–225, 1990.

[7] H. Koerner, G. Price, N. A. Pearce, M. Alexander, and R. A. Vaia. Remotely actuated polymer nanocomposites—stress-recovery of carbon-nanotube-filled thermoplastic elastomers. *Nature materials*, **3**: 115–120, 2004.

[8] S. V. Ahir and E. M. Terentjev. Photomechanical actuation in polymer-nanotube composites. *Nature Materials*, **4**: 491–495, 2005.

[9] J. Loomis, B. King, T. Burkhead, P. Xu, N. Bessler, E. Terentjev, and B. Panchapakesan. Graphene-nanoplatelet-based photomechanical actuators. *Nanotechnology*, **23**: 045501, 2012.

[10] K. Czaniková, I. Krupa, M. Ilčíková, P. Kasák, D. Chorvár, M. Valentin, M. Šlouf, J. Mosnáček, M. Mičušík, and M. Omastová. Photo-actuating materials based on elastomers and modified carbon nanotubes. *Journal of Nanophotonics*, **6**: 810707, 2011.

[11] S. V. Ahir and E. M. Terentjev. Fast relaxation of carbon nanotubes in polymer composite actuators. *Physical Review Letters*, **96**: 133902–133904, 2006.

[12] R. Vaia. Nanocomposites: Remote-controlled actuators. *Nature Materials*, **4**: 429–430, 2005.

[13] A. D. Winter, E. Larios, F. M. Alamgir, C. Jaye, D. A. Fischer, M. Omastová, and E. M. Campo. Thermo-active behaviour of ethylene-vinyl acetate | multiwall carbon nanotube composites examined by in situ near edge x-ray absorption fine structure spectroscopy. *The Journal of Physical Chemistry C*, **118**: 3733–3741, 2014.

[14] J. Genzer, E. Sivaniah, E. J. Kramer, J. Wang, H. Korner, K. Char, C. K. Ober, B. M. DeKoven, R. A. Bubeck, D. A. Fischer, and S. Sambasivan. Temperature Dependence of Molecular Orientation on the Surfaces of Semifluorinated Polymer Thin Films. *Langmuir*, **16**: 1993–1997, 2000.

[15] B. Ravel and M. Newville. Athena, Artemis, and Hephaestus. *Journal of synchrotron radiation*, **12**: 537–541, 2005.

[16] G. Hähner. Near edge X-ray absorption fine structure spectroscopy as a tool to probe electronic and structural properties of thin organic films and liquids. *Chemical Society Reviews*, **35**: 1244–1255, 2006.

[17] R. Saito, T. Takeya, T. Kimura, G. Dresselhaus, and M. S. Dresselhaus. Raman intensity of single-wall carbon nanotubes. *Physical Review B*, **57**: 4145, 1998.

[18] M. S. Dresselhaus, A. Jorio, M. Hofmann, G. Dresselhaus, and R. Saito. Perspectives on carbon nanotubes and graphene Raman spectroscopy. *Nano Letters*, **10**: 751–758, 2010.

[19] M. Shimoyama, H. Maeda, K. Matsukawa, H. Inoue, T. Ninomiya, and Y. Ozaki. Discrimination of ethylene/vinyl acetate copolymers with different composition and prediction of the vinyl acetate content in the copolymers using Fourier-transform Raman spectroscopy and multivariate data analysis. *Vibrational spectroscopy*, **14**: 253–259, 1997.

[20] S. Abbasi, P. J. Carreau, and A. Derdouri. Flow induced orientation of multiwalled carbon nanotubes in polycarbonate nanocomposites: Rheology, conductivity and mechanical properties. *Polymer*, **51**: 922–935, 2010.

[21] J. Komornicki, M. Bourrel, G. Marin, and M. Brogly. Thermal and visco-elastic properties of EVA-based hot-melt adhesives: relationship to peel behaviour. *Journal of Adhesion Science and Technology*, **6**: 293–305, 1992.

[22] A. M. Marconnet, N. Yamamoto, M. A. Panzer, B. L. Wardle, and K. E. Goodson. Thermal Conduction in Aligned Carbon Nanotube-Polymer Nanocomposites with High Packing Density. *ACS nano*, **5**: 4818–4821, 2011.

[23] A. Beigbeder, M. Linares, M. Devalckenaere, P. Degée, M. Claes, D. Beljonne, R. Lazzaroni, and P. Dubois. CH-π Interactions as the Driving Force for Silicone-Based Nanocomposites with Exceptional Properties. *Advanced Materials*, **20**: 1003–1007, 2008.

[24] S. L. Teh, D. Linton, and M. D. Dadmun. Controlling Non-Covalent Interactions to Modulate the Dispersion of Fullerenes in Polymer Nanocomposites. *Macromolecules*, **44**: 7737–7745, 2011.

[25] Y. Y. Zhang, C. M. Wang, and V. B. C. Tan. Buckling of carbon nanotubes at high temperatures. *Nanotechnology*, **20**: 215702, 2009.

[26] S. V. Ahir, Y. Y. Huang, and E. M. Terentjev. Polymers with aligned carbon nanotubes: Active composite materials. *Polymer*, **49**: 3841–3854, 2008.

[27] J. Foroughi, G. M. Spinks, G. G. Wallace, J. Oh, M. E. Kozlov, S. Fang, T. Mirfakhrai, J. D. W. Madden, M. K. Shin, S. J. Kim, et al. Torsional carbon nanotube artificial muscles. *Science*, **334**: 494–497, 2011.

[28] M. D. Lima, N. Li, M. J. De Andrade, S. Fang, J. Oh, G. M. Spinks, M. E. Kozlov, C. S. Haines, D. Suh, J. Foroughi, et al. Electrically, chemically, and photonically powered torsional and tensile actuation of hybrid carbon nanotube yarn muscles. *Science*, **338**: 928–932, 2012.

Chapter 6

Ageing-derived failure of EVA|MWCNT composites

6.1 Introduction

In the previous chapter, a synchronous interplay between $\pi^*_{C=C}$ and $\pi^*_{C=O}$ resonances was revealed in *in situ* temperature-resolved NEXAFS spectra of freshly synthesised thermoactive EVA|MWCNT composites, which suggested conformational variations between polymeric chains and CNTs. The proposed model explained this observation as torsional deformations in CNTs upon irradiation, which in turn disrupted the aligned orientation of CH–π-bound polymeric chains. As alignment is a critical aspect in active behaviour,[1] the model also accounted for the increased spectral response of strained composite, which showed enhanced alignment.

A seldom addressed aspect in the study of non-covalent interactions in nanocomposites is that of durability and ageing effects. This property is important considering that these interactions—in this case, π-π interactions between filler and dispersant, and CH−π interactions between dispersant and polymer—are individually weak, and rely on cooperativity effects for effective adhesion:[2] any time-dependent effects in molecular structure and bonding have direct consequences on commercialisation of nanocomposite systems. This chapter reports on the molecular durability of EVA|MWCNT composites 12 months after synthesis as a vehicle to explore the molecular communication between MWCNTs, PyChol, and EVA, as related to fabrication and further relaxation upon ageing.[3]

[1] S. V. Ahir and E. M. Terentjev. *Phys. Rev. Lett.*, **96**: 133902–133904, 2006.
[2] D. Baskaran, J. W. Mays, and M. S. Bratcher. *Chem. Mater.*, **17**: 3389–3397, 2005.
[3] A. D. Winter et al. *APL Mater.*, **2**: 066105, 2014.

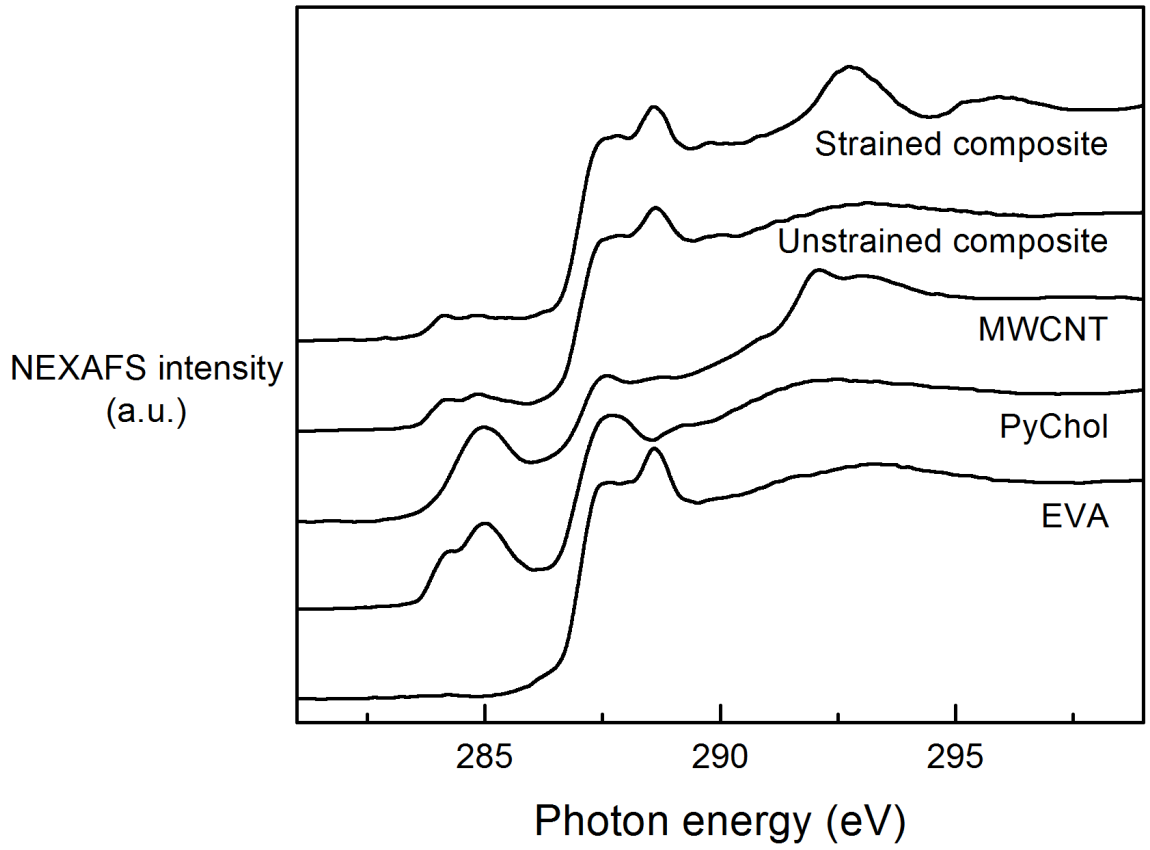

Figure 6.1: Room-temperature Carbon *K*-edge NEXAFS spectra of aged composites and constituents.

6.2 Ageing effects in NEXAFS spectroscopy

Room temperature Carbon *K*-edge NEXAFS spectra of PyChol and MWCNTs, and aged (12 months after synthesis) EVA, PyChol, MWCNTs and unstrained and strained EVA|MWCNT-PyChol composites are shown in Figure 6.1. EVA shows three typical resonances at 287 eV, 288.9 eV, and 293 eV, attributed to $1s \rightarrow \sigma^*_{C-H}$, $1s \rightarrow \pi^*_{C=O}$, and $1s \rightarrow \sigma^*_{C-C}$ electronic transitions.[4] Fresh EVA (discussed in the previous chapter), also showed an additional feature at 285 eV, which is absent here. This confirms the earlier assignment to this emission as reflective of surficial carbonaceous impurity, which have unlatched over time.[3]

Spectral features in PyChol have been addressed in the previous chapter, but it is worth highlighting again possible origins of both $\pi^*_{C=C}$ emissions at lower energies. PyChol molecules have two groups permissive of $1s \rightarrow \pi^*_{C=C}$ transitions: pyrene, which—given the chemical similarity to CNT walls—is attributed the 285 eV resonance,[5] and the single C=C bond within the cholesteryl group.[3] Since the latter is within a different chemical structure,

[4] A. D. Winter et al. *J. Phys. Chem. C*, **118**: 3733–3741, 2014.
[5] V. Lee et al. *J. Phys. Chem. Lett.*, **1**: 1247–1253, 2010.

Table 6.1: Energy (eV) and intensity values (a.u.) of $\pi^*_{C=C}$ and $\pi^*_{C=C}$ NEXAFS resonances in fresh and aged composites and constituents.

System	$E(\pi^*_{C=C})$	$\Delta E(\pi^*_{C=C})^a$	$I(\pi^*_{C=C})$	$E(\pi^*_{C=O})$	$\Delta E(\pi^*_{C=O})^b$	$I(\pi^*_{C=O})$
PyChol	285.0	—	0.40	—	—	—
EVA	—	—	—	288.6	—	1.13
Unstrained†	284.9	-0.1	0.22	288.6	0.0	0.91
Strained†	284.9	-0.1	0.09	288.5	-0.1	1.17
Unstrained‡	284.8	-0.2	0.17	288.6	0.0	1.00
Strained‡	284.8	-0.2	0.16	288.5	0.01	1.06

[a] Calculated against reference provided by PyChol.

[b] Calculated against reference provided by EVA.

† Fresh unstrained and strained composites.

‡ Aged unstrained and strained composites.

it is expected to produce a NEXAFS intensity at a different photon energy.[6,7]

NEXAFS spectrum of MWCNTs is once again characterised by a sharp resonance at 285 eV, corresponding to $1s \rightarrow \pi^*_{C=C}$ transitions, and $1s \rightarrow \sigma^*_{C-C}$ transition resonances above 290 eV, convoluted as a broader resonance.[8] In the energy region of 287-299 eV, the spectrum shows a series of intensities present in both EVA and PyChol, representative in MWCNTs of chemical impurities from growth.[9]

Following a building block model, spectrum of aged unstrained composite shows spectral fingerprints of all three constituents: $\pi^*_{C=C}$ resonances from MWCNTs and PyChol, σ^*_{C-H} and $\pi^*_{C=O}$ from EVA and PyChol (and to a lesser extent, impurities in MWCNTs), and σ^*_{C-C} resonances from MWCNTs, PyChol and EVA. To aid the comparison upon ageing, spectral differences are summarised in Table 6.1. Two differences are noted between spectra of fresh and aged unstrained composite: firstly, a broadened σ^*_{C-C} feature, and secondly, a −0.1 eV shift in $\pi^*_{C=C}$ resonances. These observations are discussed later.

It was previously observed that, upon straining, NEXAFS composite spectra revealed conformational changes: decreased $\pi^*_{C=C}$ intensity from cholesteryl group in PyChol, increased $\pi^*_{C=O}$ intensity, and an negative shift of 0.1 eV in this latter resonance. These effects were spectral confirmation of CNT alignment, which, in turn, promoted alignment of EVA chains.[4]

[6] J. Stöhr. *NEXAFS Spectroscopy*. Springer, 2003.

[7] G. Hähner. *Chem. Soc. Rev.*, **35**: 1244–1255, 2006.

[8] T. Hemraj-Benny et al. *Small*, **2**: 26–35, 2006.

[9] A. Hirsch. *Angew. Chem. Int. Ed.*, **41**: 1853–1859, 2002.

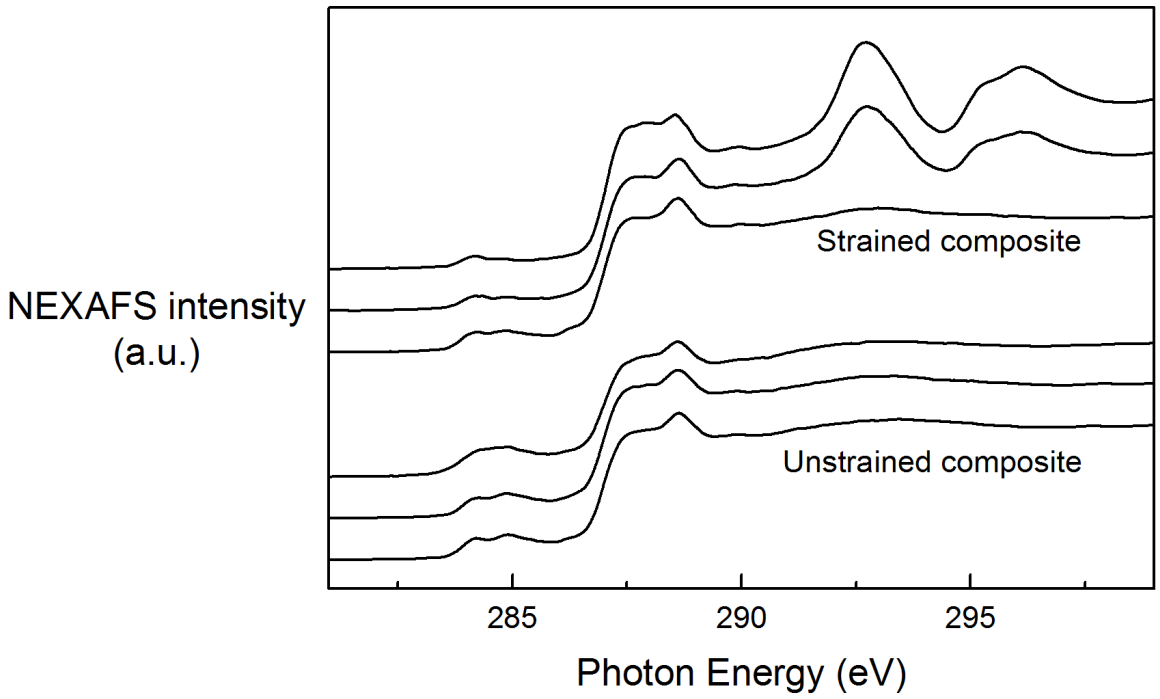

Figure 6.2: Room temperature Carbon *K*-edge NEXAFS spectra from three different sample locations reveal a lack of homogeneity, more evident in prestrained composite.

It is evident that these conformational mechanisms have been lost upon ageing, since there are no significant spectral differences between unstrained and strained composites up to ~291 eV (Figure 6.1, Table 6.1). This is the first suggestion that the strain introduced during composite synthesis has relaxed over time.

The negative shift in $\pi^*_{C=C}$ resonances of unstrained composite are also evident in strained composite. Indeed, a shift of −0.1 eV was observed first in fresh spectra of both composites, with reference to MWCNTs and PyChol, which was attributed to CNT functionalisation with PyChol molecules through π–π interactions.[10] The additional −0.1 eV shift in both composites upon ageing suggests, therefore, that π–π interactions have altered over time.[3]

At energies above 291 eV, the previously broad σ^*_{C-C} emission in fresh strained composite (in reality, a convolution of resonances at slightly different energies) is now deconvolved into separate, narrower resonances (Figure 6.1). This is suggestive of molecular disorder, since this resonance is produced by every composite constituent. As before, NEXAFS spectra were acquired from three irradiated regions in the composite. Whereas the earlier scans showed molecular homogeneity in both systems, only unstrained composite is spectrally homogeneous; strained composite shows large spatial variations in σ^*_{C-C} resonances (Figure 6.2). The difference between homogeneity in strained and unstrained aged composites

[10]N. Kocharova et al. *Langmuir*, **24**: 3235–3243, 2008.

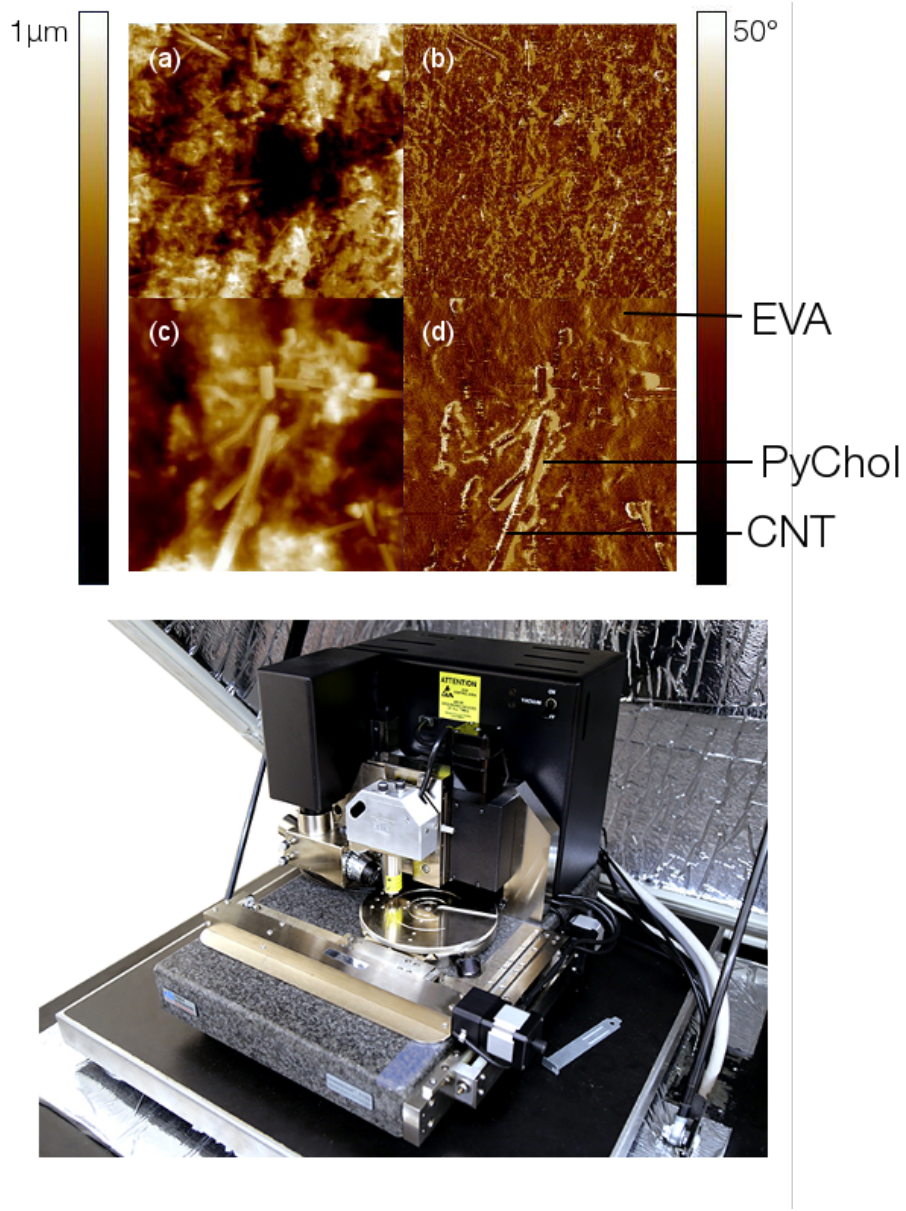

Figure 6.3: AFM height (a and c) and corresponding phase (b and d) morphologies of aged strained composite at different magnifications. Scan sizes are 50 µm (a and b) and 15 µm (c and d), with z-scales of 1 µm (a and c) and 50°(b and d). Reprinted with permission,[3] ©AIP Publishing LLC. Acquired with Digital Instruments Dimension 3100 Atomic Force Microscope (bottom) at Bangor University.

points again to effects of pre-strain relaxation.

AFM maps reveal elongated structures associated with CNTs, and some roughness in the matrix background (Figure 6.3a). Topographic micrographs are complemented here with phase characterisation, as it distinguishes between mechanical properties such as Young's modulus, viscoelasticity, and adhesion, crucial for composite systems. In this case, phase

contrast allows the differentiation of systems with segregated soft and hard phases.[11] It has been shown that a brighter phase contrast results from stiffer phases in soft and moderate tapping modes, which were used here.[12] Additionally, crystalline phases are predicted to yield brighter phase contrasts, caused by decreased dissipation and damping, relative to amorphous phases.[11] In Figures 6.3b and d, two distinct phases are identified: amorphous EVA matrix, shown as dark background, and crystalline PyChol, seen as bright phase. This classification is particularly important in Figure 6.3d, where bright regions around CNTs correspond to deposits of unlatched PyChol. Indeed, PyChol unlatching from CNT walls is one possible mechanism that would result in the molecular disorder observed primarily in NEXAFS.

6.3 Failure of active behaviour

An inverse variation in $\pi^*_{C=C}$ and $\pi^*_{C=O}$ resonance intensities was observed in *in situ* temperature-resolved NEXAFS spectra of freshly synthesised EVA|MWCNT-PyChol composites, which was correlated to macroscopic thermo-active behaviour.[4,13] Given the spectral evidence of ageing in the same composites, the question then arises: how has ageing affected the temperature response? A similar *in situ* NEXAFS experiment was conducted on the aged systems, and the data is shown in Figure 6.4.

Although $\pi^*_{C=C}$ intensities do increase at a higher temperature (as before), $\pi^*_{C=O}$ intensities show a slight decrease in unstrained composite, and almost no variation in strained composite. This lack of temperature-dependent $\pi^*_{C=O}$ intensity suggests disconnection between MWCNT and EVA chains, following the actuation model proposed in the previous chapter. Further supporting this, aged strained composite no longer demonstrates angular dependence of $\pi^*_{C=O}$ resonances at room temperature (Figure 6.5), which was observed in fresh strained composite (Figure 5.8)—this again suggests decreased CNT-polymer interactions. As seen in AFM, PyChol unlatching is the likely cause of this.

From all ageing observations thus far, three distinct stages for the composites under study can be deduced, shown schematically in Figure 6.6 (EVA polymer shown only as vinyl acetate for simplicity): mixing/sonication, strain, and ageing-derived relaxation/disorder. Upon sonication (Figure 6.6a), MWCNTs are non-covalently functionalised with PyChol molecules through π–π interactions (suggested by an energy shift of $\pi^*_{C=C}$ resonances),[4,10] and EVA chains wrap around MWCNT-PyChol ensembles through CH—π interactions.[2,4,14]

[11] P. Schön et al. *Eur. Polym. J.*, **47**: 692–698, 2011.
[12] S. N. Magonov and D. H. Reneker. *Annu. Rev. Mater. Sci.*, **27**: 175–222, 1997.
[13] K. Czaniková et al. *J. Nanophotonics*, **6**: 810707, 2011.
[14] A. D. Winter et al. *Langmuir*, **29**: 15822–15830, 2013.

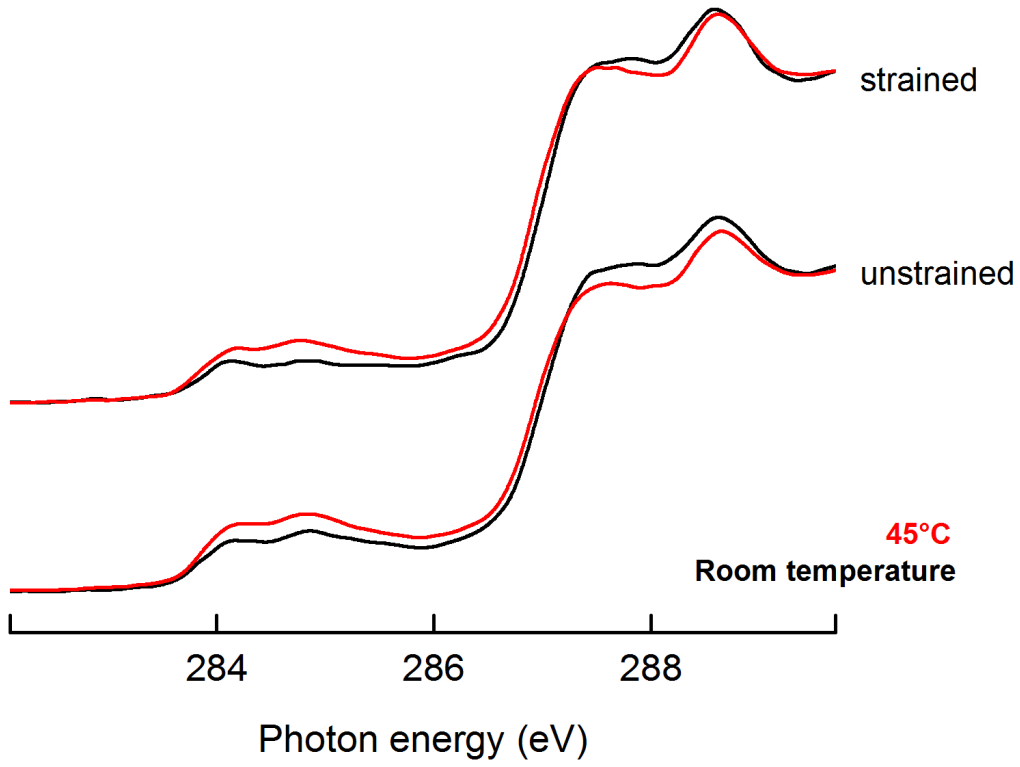

Figure 6.4: Temperature-resolved NEXAFS spectra of aged strained and unstrained composites. Coupled intensity interplay for $\pi^*_{C=C}$ and $\pi^*_{C=O}$ resonances is no longer observed.

When uniaxial strain is applied (Figure 6.6b), CNTs align as expected (evidenced by Raman spectroscopy). This leads to enhanced alignment of EVA chains as well, observed as an increase in $\pi^*_{C=O}$ intensity in NEXAFS. This $\pi^*_{C=O}$ resonance also experiences a shift, which possibly indicates modification in the chemical environment at the vicinity of C=O groups. Temperature-resolved NEXAFS spectra of fresh strained composite showed an improved thermal macroscopic and molecular response, compared to unstrained composite, which tentatively has been attributed to improved interfacial connectivity i.e. straining has resulted in stronger π–π interactions.[3] The externally provided elastic energy could be stored in a metastable modified π–π system, which resonates with the concept of nanomechanical interlocking.[15] Incidently, the notion of stronger interactions resulting from straining bears resemblance to so-called 'catch' bonds in biophysics.[16] In contrast with conventional, or 'slip' bonds, where bond lifetimes and strengths decrease with applied tensile force,[17] the lifetime

[15]M. Wong et al. *Polymer*, **44**: 7757–7764, 2003.
[16]S. Rakshit and S. Sivasankar. *Phys. Chem. Chem. Phys.*, **16**: 2211–2223, 2014.
[17]G. I. Bell. *Science*, **200**: 618–627, 1978.

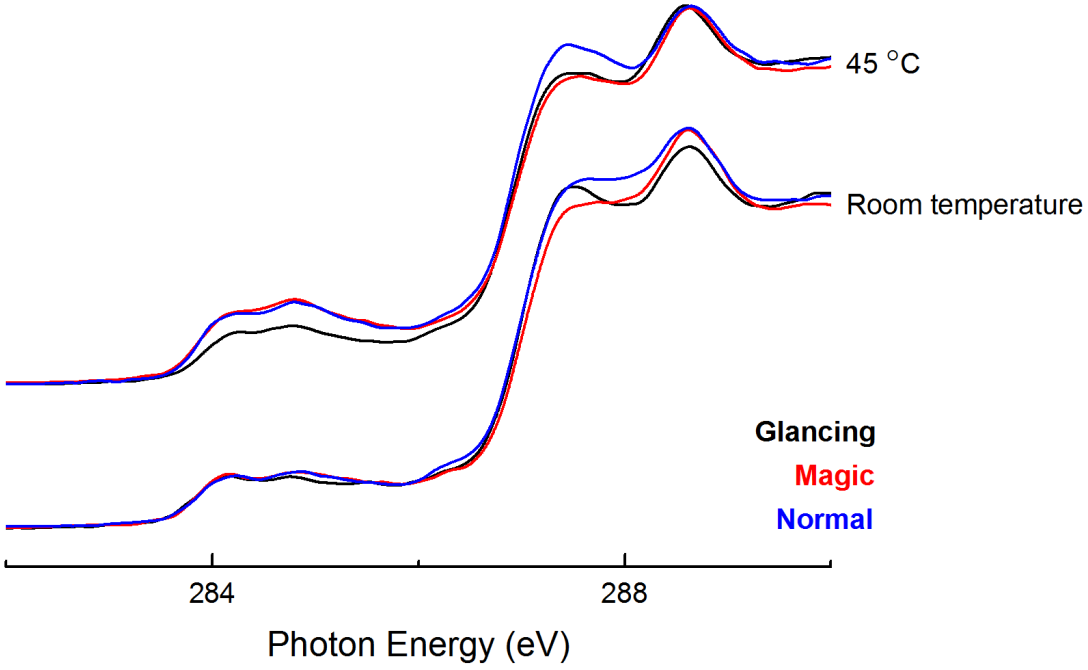

Figure 6.5: Angular dependence of $\pi^*_{C=O}$ resonances no longer change in aged strained composite at higher temperatures, unlike fresh composites.

and strength of catch bonds lie at some non-zero applied force.[18,19]

Upon ageing (Figure 6.6c), π–π interactions binding PyChol molecules to MWCNT walls deteriorate, breaking effective interactions between fillers and polymer, and this is accentuated by relaxation of strain.[3] In fact, all conformational phenomena indicated by NEXAFS spectra is reversed: in this scheme, the stored energy in the proposed metastable π–π system (Figure 6.6b) could, upon relaxation, act as the driving force towards increased entropy in a PyChol-segregating system.[20]

Although the lack of CNT-EVA interactions is unlikely to render macroscopic actuation, it is worth analysing the temperature-derived trends in comparison to those of fresh composites. Indeed, since MWCNTs and EVA chains are connected through PyChol molecules, the differences in comparative parameters in Table 6.2 are reflecting changes in π-π interactions between MWCNTs and PyChol, allowing for a semi-quantitative description to be derived. Since ageing effects are observed in both unstrained and strained composites, two

[18]W. E. Thomas, V. Vogel, and E. Sokurenko. *Biophysics*, **37**: 399–416, 2008.

[19]H. Chen and A. Alexander-Katz. *Biophys. J.*, **100**: 174–182, 2011.

[20]S. Giri and C. Wan. "Electronic Applications of Ethylene Vinyl Acetate and Its Composites" in: *Flexible and Stretchable Electronic Composites*. Springer, 2016. 61–85

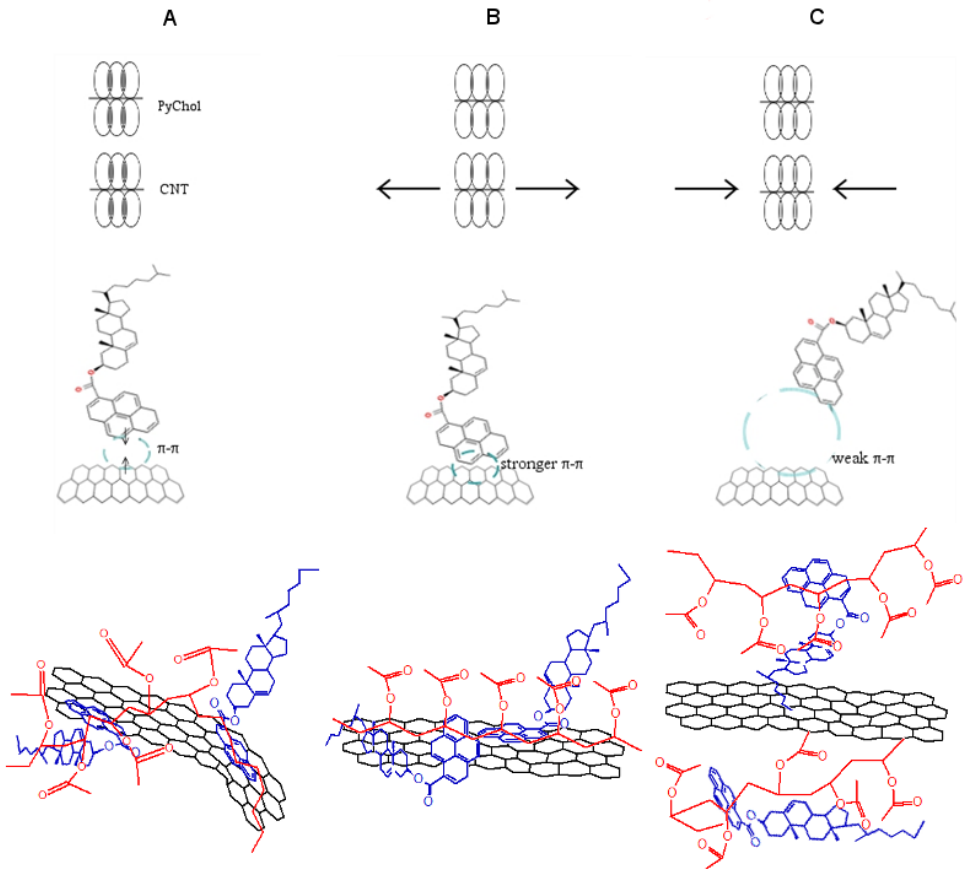

Figure 6.6: Proposed model of interaction dynamics: a) mixing/sonication, b) straining, and c) ageing. Reprinted with permission,[3] ©AIP Publishing LLC.

Table 6.2: Energy and intensity values of $\pi^*_{C=C}$ and $\pi^*_{C=C}$ NEXAFS resonances in fresh and aged composites and constituents.

Parameter	Fresh	Aged
$x_{\text{unstrained}}$	5	4
x_{strained}	10	54
$y_{C=C}$	7	3
$y_{C=O}$	4	0.17

mechanisms are likely promoting the total degradation of π-π interactions (A_T). The first of these is a natural lifetime of π-π interactions ($A_{\pi-\pi}$), distinct from actuation fatigue. The second mechanism derives from relaxation of strain (A_ε). The total ageing is therefore a sum of these two phenomena (equation 6.1).

$$A_T = A_{\pi-\pi} + A_\varepsilon \tag{6.1}$$

Clearly, $A_\varepsilon = 0$ in unstrained composites, and these will solely reflect $A_{\pi-\pi}$. The parameter x compares the temperature-dependent intensity variations of $\pi^*_{C=C}$ and $\pi^*_{C=O}$ resonances, and can serve as a measure of MWCNT-EVA interconnectivity (through PyChol molecules). The decrease upon ageing of $x_{\text{unstrained}}$ from 5 to 4 may be interpreted as a 20% decrease in PyChol CNT coverage ($A_{\pi-\pi} = 20\%$).

The same rationale may not be applied to aged strained composites. Figure 6.4 shows a lack of synchronicity between intensities of $\pi^*_{C=C}$ and $\pi^*_{C=O}$ resonances; the ratio of $x_{\text{strained}} = 54$ lacks physical meaning, and an alternative method is needed to quantify ageing effects. Whilst equation 5.1 is a measure of filler-matrix connectivity through PyChol, equation 5.2 highlights the impact of strain on the temperature response of EVA. In fresh composites $y_{C=O} = 4$ was obtained, where 100% PyChol coverage is assumed. By the same argument, in the aged scenario, $y_{C=O} = 0.17$ correlates to only 4% PyChol coverage, where 96% has unlatched. Since strained composites would undergo both $A_{\pi-\pi}$ and A_ε, it follows under these considerations that $A_T = 96\%$, where $A_{\pi-\pi} = 20\%$ and $A_\varepsilon = 76\%$.

6.4 Summary

This comparative NEXAFS study enabled the identification of π-π interactions in priorly thermoactive EVA|MWCNT composites, as evidenced by an energy shift. Spectral signatures of the 12-month aged composites revealed chemical disorder—also confirmed by AFM—suggesting π-π interactions forming the supramolecular system have a limited lifetime. The disorder was seen to a greater extent in strained composites, suggesting a relaxation over time. The previously found inversely coupled intensity interplay between $\pi^*_{C=C}$ and $\pi^*_{C=O}$ resonances in temperature-resolved spectra was not observed, suggesting the aged composites are no longer thermoactive.

All observations from NEXAFS and AFM pointed to PyChol molecules unlatching from CNT walls and segregating as a consequence of ageing. Application of strain during composite synthesis, which promotes alignment and results in stronger π-π interactions (in good agreement with nanomechanical interlocking in nanocomposites and catch bonds in biophysics), also accelerates the ageing-derived failure of the system. These are important considerations towards microsystem manufacturing to ensure device longevity.

Bibliography

[1] S. V. Ahir and E. M. Terentjev. Fast relaxation of carbon nanotubes in polymer composite actuators. *Physical Review Letters*, **96**: 133902–133904, 2006.

[2] D. Baskaran, J. W. Mays, and M. S. Bratcher. Noncovalent and nonspecific molecular interactions of polymers with multiwalled carbon nanotubes. *Chemistry of Materials*, **17**: 3389–3397, 2005.

[3] A. D. Winter, C. Jaye, D. A. Fischer, M. Omastová, and E. M. Campo. Prestrain relaxation in non-covalently modified ethylene-vinyl acetate | PyChol | multiwall carbon nanotube nanocomposites. *APL Materials*, **2**: 066105, 2014.

[4] A. D. Winter, E. Larios, F. M. Alamgir, C. Jaye, D. A. Fischer, M. Omastová, and E. M. Campo. Thermo-active behaviour of ethylene-vinyl acetate | multiwall carbon nanotube composites examined by in situ near edge x-ray absorption fine structure spectroscopy. *The Journal of Physical Chemistry C*, **118**: 3733–3741, 2014.

[5] V. Lee, C. Park, C. Jaye, D. A. Fischer, Q. Yu, W. Wu, Z. Liu, J. Bao, S.-S. Pei, C. Smith, P. Lysaght, and S. Banerjee. Substrate hybridization and rippling of graphene evidenced by near-edge X-ray absorption fine structure spectroscopy. *The Journal of Physical Chemistry Letters*, **1**: 1247–1253, 2010.

[6] J. Stöhr. *NEXAFS Spectroscopy*. Springer, 2003.

[7] G. Hähner. Near edge X-ray absorption fine structure spectroscopy as a tool to probe electronic and structural properties of thin organic films and liquids. *Chemical Society Reviews*, **35**: 1244–1255, 2006.

[8] T. Hemraj-Benny, S. Banerjee, S. Sambasivan, M. Balasubramanian, D. Fischer, G. Eres, A. A. Puretzky, D. B. Geohegan, D. H. Lowndes, W. Han, J. A. Misewich, and S. S. Wong. Near-Edge X-ray Absorption Fine Structure Spectroscopy as a Tool for Investigating Nanomaterials. *Small*, **2**: 26–35, 2006.

[9] A. Hirsch. Functionalization of single-walled carbon nanotubes. *Angewandte Chemie International Edition*, **41**: 1853–1859, 2002.

[10] N. Kocharova, J. Leiro, J. Lukkari, M. Heinonen, T. Skála, F. Šutara, M. Skoda, and M. Vondrácek. Self-assembled carbon nanotubes on gold: polarization-modulated infrared reflection-absorption spectroscopy, high-resolution X-ray photoemission spectroscopy, and near-edge x-ray absorption fine structure spectroscopy study. *Langmuir*, **24**: 3235–3243, 2008.

[11] P. Schön, K. Bagdi, K. Molnár, P. Markus, B. Pukánszky, and G. Julius Vancso. Quantitative mapping of elastic moduli at the nanoscale in phase separated polyurethanes by AFM. *European Polymer Journal*, **47**: 692–698, 2011.

[12] S. N. Magonov and D. H. Reneker. Characterization of polymer surfaces with atomic force microscopy. *Annual Review of Materials Science*, **27**: 175–222, 1997.

[13] K. Czaniková, I. Krupa, M. Ilčíková, P. Kasák, D. Chorvár, M. Valentin, M. Šlouf, J. Mosnáček, M. Mičušík, and M. Omastová. Photo-actuating materials based on elastomers and modified carbon nanotubes. *Journal of Nanophotonics*, **6**: 810707, 2011.

[14] A. D. Winter, E. Larios, F. M. Alamgir, C. Jaye, D. A. Fischer, and E. M. Campo. Near-edge x-ray absorption fine structure studies of electrospun poly (dimethylsiloxane)/poly (methyl methacrylate)/multiwall carbon nanotube composites. *Langmuir*, **29**: 15822–15830, 2013.

[15] M. Wong, M. Paramsothy, X. J. Xu, Y. Ren, S. Li, and K. Liao. Physical interactions at carbon nanotube-polymer interface. *Polymer*, **44**: 7757–7764, 2003.

[16] S. Rakshit and S. Sivasankar. Biomechanics of cell adhesion: how force regulates the lifetime of adhesive bonds at the single molecule level. *Physical Chemistry Chemical Physics*, **16**: 2211–2223, 2014.

[17] G. I. Bell. *Science*, **200**: 618–627, 1978.

[18] W. E. Thomas, V. Vogel, and E. Sokurenko. Biophysics of catch bonds. *Biophysics*, **37**: 399–416, 2008.

[19] H. Chen and A. Alexander-Katz. Polymer-based catch-bonds. *Biophysical journal*, **100**: 174–182, 2011.

[20] S. Giri and C. Wan. "Electronic Applications of Ethylene Vinyl Acetate and Its Composites" in: *Flexible and Stretchable Electronic Composites*. Springer, 2016. 61–85

Chapter 7

Excessive sonication in EVA|MWCNT composites

7.1 Introduction

One of the key points highlighted in the previous chapter was the natural lifetime of non-covalent π-π interactions, which, in the case of thermoactive EVA|MWCNT composites, leads to device failure by disrupting propagation of physical phenomena from nanotubes to polymer.[1] It was also shown that strain considerably exacerbates interactions' lifetimes.[1] In these composites, π-π interactions are initially established upon sonication of nanotubes along with the dispersant PyChol molecules,[2] yet excessive sonication can damage the graphitic lattice in CNTs, ultimately resulting in scission.[3–7] This damage alters the pristine π system in CNTs thereby altering π-π interactions. This chapter furthers investigations of EVA|MWCNT composites, synthesised as in the previous chapters, but with four times the acoustic energy density delivered in sonication, yielding mechanically inactive composites.[8] In particular, this chapter reports the damage caused by excessive sonication of MWCNT with PyChol, and the subsequent dynamics of the EVA|MWCNT composites following progressive strain addressed by monitoring molecular arrangements through NEXAFS and Raman spectroscopies: the former monitoring polymer behaviour and the latter MWCNT behaviour.

[1] A. D. Winter et al. *APL Mater.*, **2**: 066105, 2014.
[2] K. Czaniková et al. *J. Nanophotonics*, **6**: 810707, 2011.
[3] K. L. Lu et al. *Carbon*, **34**: 814–816, 1996.
[4] Y. Y. Huang, T. P. J. Knowles, and E. M. Terentjev. *Adv. Mater.*, **21**: 3945–3948, 2009.
[5] Y. Y. Huang and E. M. Terentjev. *Polymers*, **4**: 275–295, 2012.
[6] M. D. Rossell et al. *Carbon*, **61**: 404–411, 2013.
[7] K. G. Dassios et al. *J. Phys. Chem. C*, **119**: 7506–7516, 2015.
[8] A. D. Winter et al. *J. Phys. Chem. C*, **119**: 20091–20099, 2015.

7.2 Experimental

7.2.1 Nanocomposite fabrication

EVA|MWCNT composites were synthesised in a similar fashion to those in previous chapters. The one key difference lies in the sonication set-up: while the same sonication energy was delivered to the MWCNT|PyChol chloroform suspension by using the same parameters as before,[9] here the sonication energy *density* was increased fourfold by reducing the sonication volume from 100 ml to 25 ml to yield an excessive sonication scheme.[10]

7.2.2 Characterisation

Angle-resolved NEXAFS Carbon *K*-edge spectra were collected at the NIST beamline U7A, NSLS, BNL, with an energy resolution of 0.1 eV, under glancing (20°), magic (55°) and normal (90°) incidence angles. An electron flood gun was used to prevent charging at the polymeric surfaces during acquisition.

Aberration-corrected TEM characterisation of pre- and post-sonication MWCNTs was performed using a JEOL JEM-2010F field-emission operated at 200 kV and a JEOL JEM-ARM200F electron microscope. Images were recorded in the high-angle annular dark-field (HAADF) and bright-field (BF) modes simultaneously at 80 kV.

Raman spectroscopy was performed with a Renishaw inVia microscope and Argon laser, and with a Renishaw Ramascope and a RL633 HeNe laser. AFM characterisation was performed with a Digital Instruments Dimension 3100 atomic force microscope in topographic mode, and operating in tapping mode.

7.3 Damage to graphitic structure

Figure 7.1a shows the sidewall of a MWCNT (∼50 graphitic layers visible) prior to sonication, with carbonaceous impurities from growth seen as blurred regions and the extra features appended to the leftmost layer, as well as dislocations, highlighted in the rectangle. Significant differences are observed upon excessive sonication (Figure 7.1b). Firstly, much of the impurities have detached from the CNT: indeed, though the primary motivation of ultrasonication in this case is to break up CNT bundles into individual nanotubes, the stripping of adsorbed moieties is a positive side effect of the procedure.

[9] A. D. Winter et al. *J. Phys. Chem. C*, **118**: 3733–3741, 2014.

[10] J. S. Taurozzi, V. A. Hackley, and M. R. Wiesner. *NIST Special Publication*, **1200-2**: 1–15, 2012.

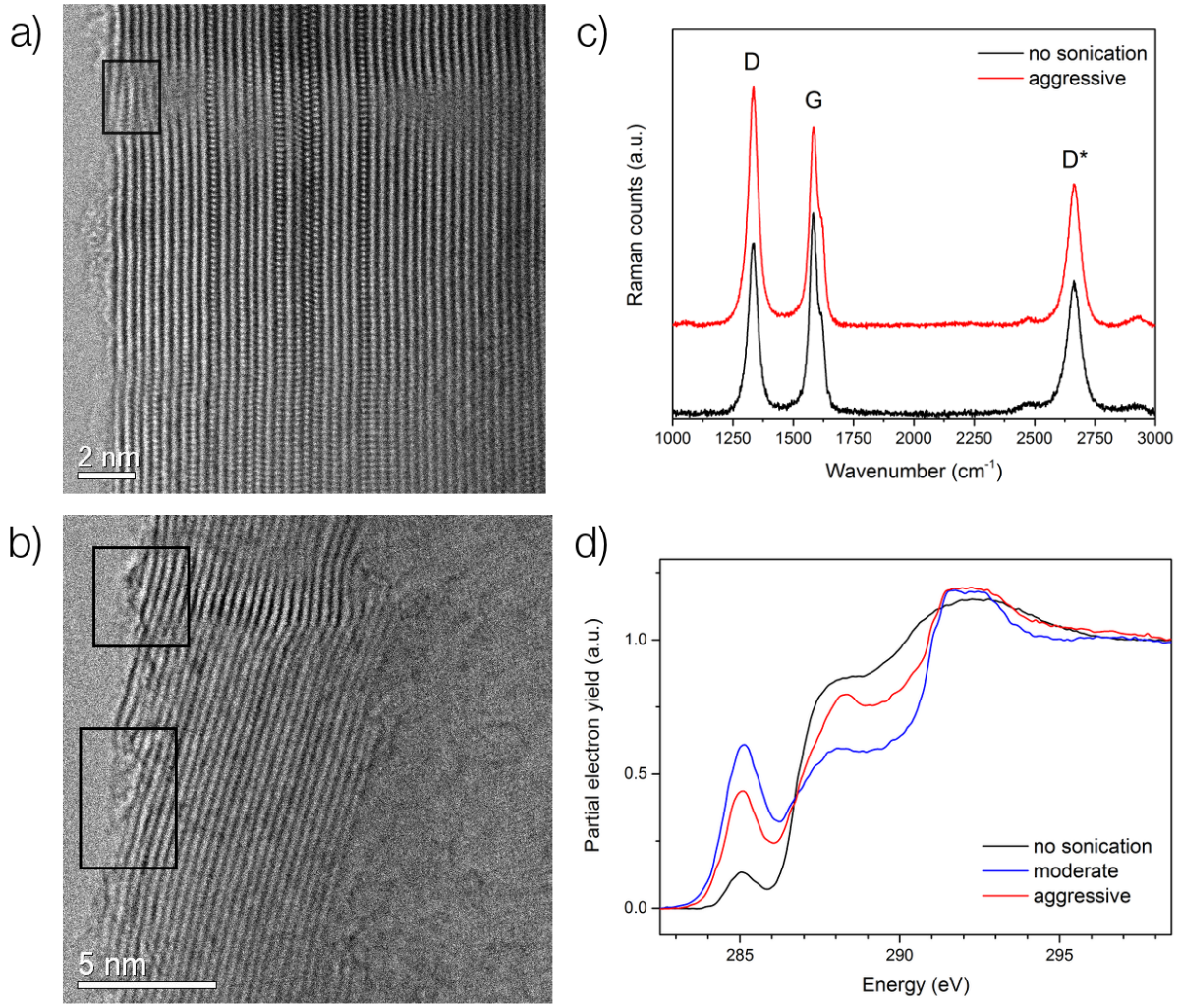

Figure 7.1: a) Aberration-corrected TEM micrograph of unsonicated MWCNT, where the rectangle indicates dislocations from imperfect growth. b) Upon sonication, severe sidewall damage is visible. c) Sonication-induced damage can be monitored by Raman spectroscopy by monitoring changes in I_D/I_G ratios. d) NEXAFS spectra highlight the evolution of impurities ($1s \rightarrow \sigma^*_{C-H}$ and $1s \rightarrow \sigma^*_{C-O}$), as well as graphitic carbon ($1s \rightarrow \pi^*_{C=C}$), with sonication. Adapted with permission.[8] Copyright 2015 American Chemical Society.

Additionally, Figure 7.1b shows severe sidewall damage where the crystalline sp^2 structure has become amorphous (rectangles), and pronounced dislocations in the inner walls, suggesting sonication effects propagate throughout the structure. The dislocations resemble glide-climb interactions reported by Huang and coworkers, which yield cross-linked graphitic layers.[11] Clearly the π system is significantly altered, conditioning subsequent functionalisation of PyChol through π-π interactions, and final interactions with EVA polymer.

Sonication damage can be conveniently monitored using Raman and NEXAFS spec-

[11] J. Y. Huang, F. Ding, and B. I. Yakobson. *Phys. Rev. Lett.*, **100**: 035503, 2008.

troscopy. In Raman spectra, damage to CNTs will be reflected by an increase in D band intensity attributed to defects in the sp^2 carbon network,[12–14] and often as an additional decrease in G band intensity, which arises from tangential vibrations along the tube axis and is characteristic of sp^2 hybridisation.[12,13] Both these intensity variations are observed in Figure 7.1c, and can be accounted for by the I_D/I_G intensity ratio, frequently used to discuss CNT quality.[13] In Figure 7.1c, unsonicated CNTs have a ratio of 0.85, while following aggressive sonication, the ratio increases to 1.20, confirming damage to graphitic structure. Due to contributions of carbonaceous impurities (such as those seen in Figure 7.1), the interpretation of this ratio alone is insufficient to assess CNT damage/quality.[13] It was later reported that a more descriptive measurement is derived from the I_D*/I_D ratio: the D* band, a second-order harmonic of D modes (often labelled as G' or 2D), arises from a two-phonon process and is therefore less sensitive to carbonaceous impurities.[15] In the study of sonication damage, however, a significant amount of these carbonaceous impurities result from amorphisation of sp^2 carbon from the nanotube walls, and therefore are an important aspect of the system.

NEXAFS spectra (Figure 7.1d) shows a low $1s \rightarrow \pi^*_{C=C}$ resonance at 285 eV in unsonicated MWCNTs, which increases considerably under moderate sonication. The low initial intensity is likely to be due to CNT bundles. As these bundles are disentangled, more π* orbitals are rendered accessible to the beam, producing a higher intensity. An additional effect of moderate sonication, which cannot be derived from Raman spectra, is the decrease in states in the range of 287–290 eV, attributed to the stripping of adsorbed impurities, inclusive of C–H and C=O moieties from growth.[16] Further, or *aggressive*, sonication decreases once again the $1s \rightarrow \pi^*_{C=C}$ resonance intensity which—consistent with both TEM and Raman—indicates graphitic damage. As cavitation damages the graphitic lattice, dangling bonds are likely to be passivated by impurities from the sonication medium: indeed, all impurity states show an increase in intensity, with resonances from $1s \rightarrow \pi^*_{C=O}$ at ~288 eV being the most prominent.

Polarised Raman spectra of composites under all strains in the range of the G band is shown in Figure 7.2a. Raman D bands from embedded CNTs were not observed. It was reported by Jorio *et al* that from a large number of CNT spectra, 50% showed D bands with intensities 100 times weaker than G bands.[14] It is possible that D bands here are just as weak, and not observable due to attenuation from the EVA matrix. Measurements were acquired with the beam polarisation parallel (black line) and perpendicular (red line) to the strain direction for the purpose of assessing CNT alignment, which was previously achieved

[12] M. S. Dresselhaus et al. *Nano Lett.*, **10**: 751–758, 2010.
[13] J. H. Lehman et al. *Carbon*, **49**: 2581–2602, 2011.
[14] A. Jorio et al. *New J. Phys.*, **5**: 139, 2003.
[15] R. A. DiLeo, B. J. Landi, and R. P. Raffaelle. *J. Appl. Phys.*, **101**: 064307, 2007.
[16] A. Hirsch. *Angew. Chem. Int. Ed.*, **41**: 1853–1859, 2002.

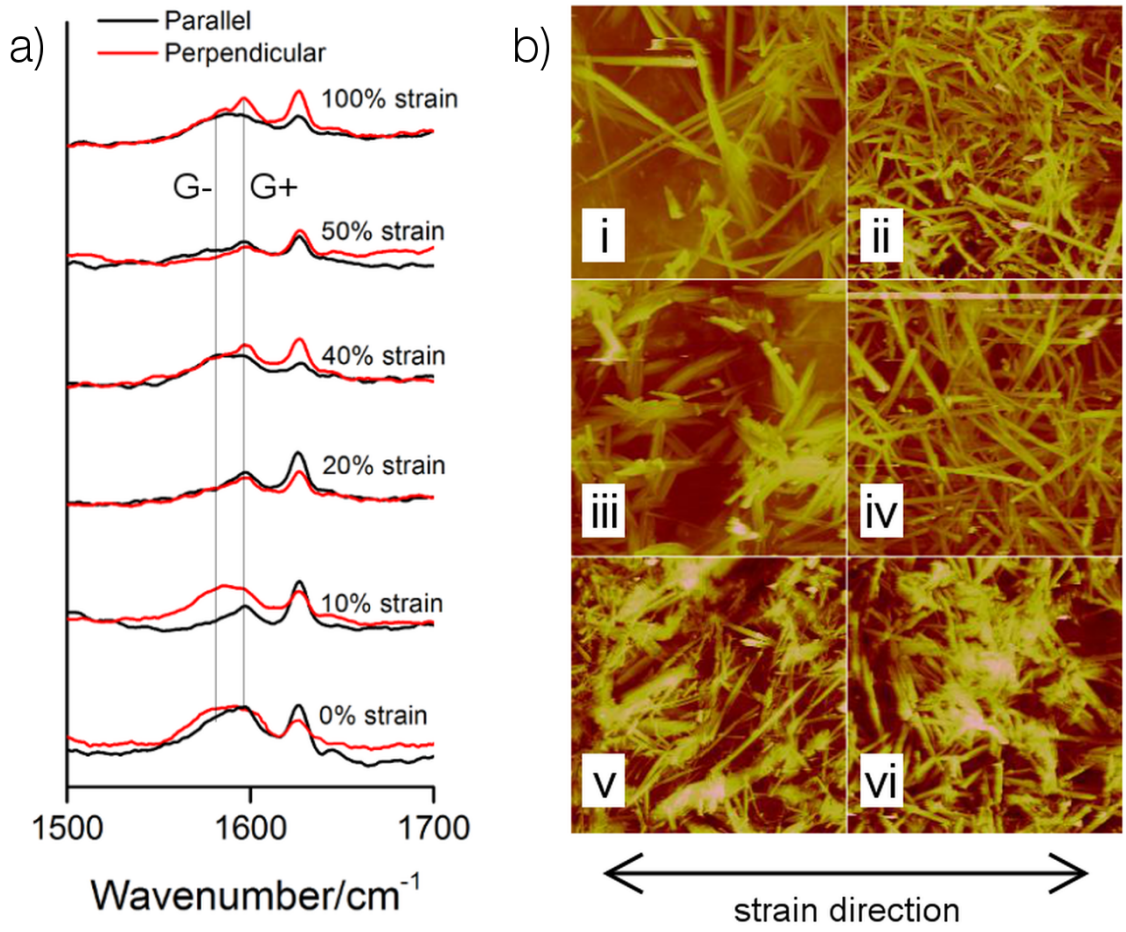

Figure 7.2: a) Polarised Raman spectra acquired with the beam polarisation parallel and perpendicular show no consistent variations. b) AFM micrographs reveal no enhanced alignment with increasing strains of i) 0%, ii) 10%, iii) 20%, iv) 40%, v) 50%, and vi) 100%. Scanned regions are 40 μm. Adapted with permission.[8] Copyright 2015 American Chemical Society.

through straining.[2,9] As was discussed in prior chapters, nanotube alignment is commonly examined through $G_{\parallel}/G_{\perp}$ ratio, where a ratio of 1 indicates isotropy, and an increasing ratio represents increasing isotropy in the parallel direction. [9,17]

The G band in carbon nanotubes is the combination of two vibration modes: vibrations along the tube axis, which produce the G+ band, and circumferential vibrations, producing G– bands.[13] Interestingly, G– mode is only shown intermittently, while only the G+ mode is consistently present. Under optimal sonication conditions, this was not the case, and in fact the two bands were convoluted and presented as one G resonance.[8] The sporadic G– signal, which is dependent on CNT diameter,[14,18] may be indicative of graphitic exfoliation: in this scheme, damage interrupts the effective CNT diameter, while allowing tangential

[17]S. Abbasi, P. J. Carreau, and A. Derdouri. *Polymer*, **51**: 922–935, 2010.
[18]M. S. Dresselhaus et al. *Phys. Rep.*, **409**: 47–99, 2005.

vibrations from inner walls, producing G+ signal. For this reason, $G_{\parallel}/G_{\perp}$ ratios cannot be reliably obtained to assess alignment.

Nevertheless, CNT alignment has been addressed through AFM in height mode, shown in Figure 7.2b. The needle-like structures have diameters in the micron range, suggesting CNT bundling. Indeed, sonication-induced damage to MWCNT walls disturb pristine π systems which, in turn, hinder formation of optimal π-π interactions with PyChol dispersant. As mentioned in earlier chapters, the cholesteryl group in PyChol is intended to act as 'spacers' between adjacent nanotubes: due to suboptimal CNT–PyChol interactions, CNTs are prone to rebundling.

Further, no increase in alignment is observed with increasing strain (Figure 7.2b). This is in contrast to CNT dynamics under adequate sonication, where 50% strain ensured sufficient alignment for actuation,[9] and suggests poor interactions—either through PyChol or directly—between polymeric chains (through which the strain is applied) and MWCNTs. This is investigated in the next section.

7.4 Load transfer

As was seen in Figure 7.2, straining of composites processed with aggressive sonication did not yield alignment. Increasing levels of strain, however, can be used to probe the non-covalent interactions by analysing load transfer. Raman spectroscopy has become a standard tool for this purpose.[19–21] In particular, the position of the D* band from nanotubes is sensitive to CNT strain (or C–C bond length), as well as to local chemical environment.[8,22]

Figure 7.3a shows Raman D* bands of the six composites fitted with Gaussians. These bands show a two peak structure, which has been attributed to the 2D stacking of graphene layers, or, in this case, multiwalls.[23] To highlight the band shifts, these have been plotted against strain (Figure 7.3b), where the error bars reflect shifts from repeated measurements. Evidently, the D* position shifts to lower wavenumbers until 40% strain, which represents lengthening of C–C bonds and is indicative of load transfer.[8,24] Indeed, Lourie and coworkers found a shift of -6 cm^{-1} in MWCNTs under hydrostatic compression.[19] Here, however, the general trend is oscillatory: after the initial downshift at 10% strain, there is an upshift at 20%. Ruan and coworkers observed a similar behaviour in strained ultrahigh molecular weight

[19] O. Lourie and H. D. Wagner. *J. Mater. Res.*, **13**: 2418–2422, 1998.
[20] X. Yan et al. *J. Phys. Chem. C*, **116**: 17897–17903, 2012.
[21] N. Lachman et al. *J. Phys. Chem. C*, **113**: 4751–4754, 2009.
[22] P. M. Ajayan et al. *Adv. Mater.*, **12**: 750–753, 2000.
[23] M. A. Pimenta et al. *Phys. Chem. Chem. Phys.*, **9**: 1276–1290, 2007.
[24] L. S. Schadler, S. C. Giannaris, and P. M. Ajayan. *Appl. Phys. Lett.*, **73**: 3842, 1998.

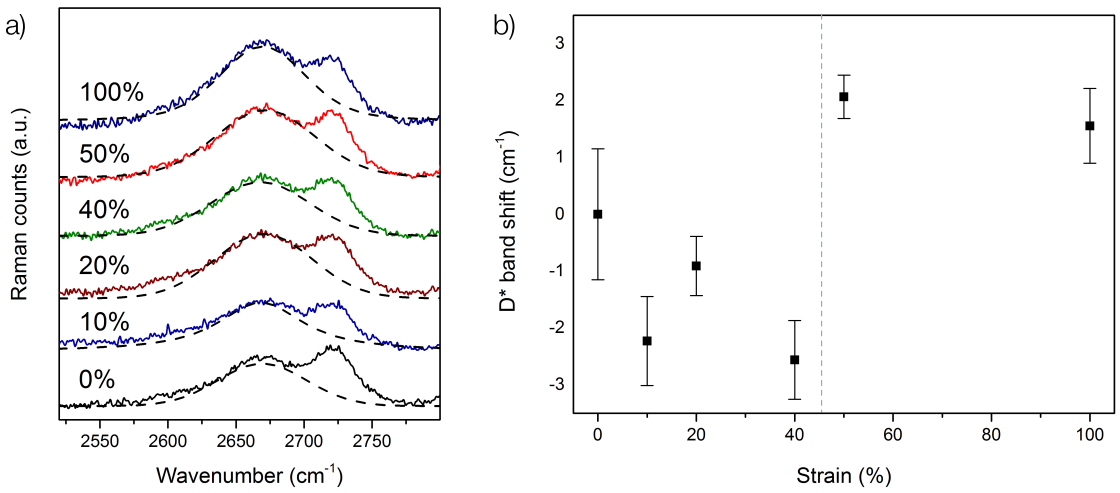

Figure 7.3: a) Fitted Raman D* bands of strained composites (in dashed lines) indicate shifts in wavenumber with every strain. b) This shift reveals an oscillatory behaviour. Adapted with permission.[8] Copyright 2015 American Chemical Society.

polyethylene (UHMWPE)|MWCNT composites, and attributed this to so-called *stick and slip* dynamics, where some strain is propagated from the polymer to the nanotubes, followed by the matrix yielding.[25] This notion is compatible with the idea of weaker interactions between CNTs and dispersant—due to sonication damage—failing as the strain increases.

A significant shift to higher wavenumber is noted at 50% strain, which, under the above considerations, would represent compression (Figure 7.3b). This is clearly infeasible, and the shift is instead suggestive of a new chemical environment in the CNT vicinity. Continuing the stick-slip unwrapping scheme, this chemical change may be explained by the polymeric chains finally detaching completely from CNTs. Additional strain shifts D* band due to hydrostatic effects.[8] The dashed line in Figure 7.3b therefore separates stick-slip dynamics (0–40% strain) and chain detachment (strains $>$ 40%).

7.5 Angular- and strain-resolved NEXAFS spectroscopy

NEXAFS resonances observed in Figure 7.4a are similar to those in prior chapters dealing with EVA|MWCNT composites. Three notable difference are observed with the systems under optimal sonications. Firstly, $1s \rightarrow \pi^*_{C=C}$ resonance intensities at 284.7 eV, which arise from PyChol cholesteryl groups (labelled π^*_1) and from CNT walls and PyChol pyrene groups (π^*_2), are drastically reduced. Under optimal sonication, composites produced clear and intense $\pi^*_{C=C}$ resonances:[9] in agreement with weak Raman G bands, the decrease

[25] S. L. Ruan et al. *Polymer*, **44**: 5643–5654, 2003.

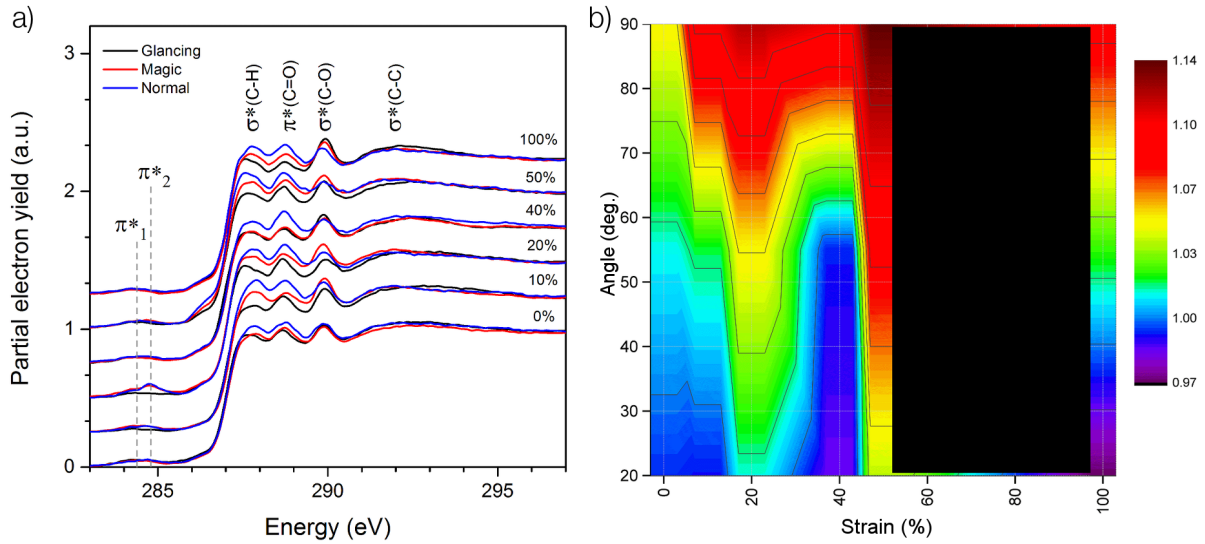

Figure 7.4: a) Angular-resolved C *K*-edge NEXAFS spectra of nanocomposites under various strains informs on the orientation of polymeric C=O groups. b) Anglular- and strain-resolved $1s \rightarrow \pi^*_{C=O}$ resonance intensity map. Adapted with permission.[8] Copyright 2015 American Chemical Society.

in $\pi^*_{C=C}$ intensities here clearly reflects damage to π systems in CNT walls from excessive sonication.[8] Secondly, Figure 7.4a shows a strong $1s \rightarrow \sigma^*_{C-O}$ resonance just below 290 eV, priorly hidden in the spectral background.[8] This signal originates from PyChol, and the increased intensity may indicate less PyChol appended to CNTs due to excessive sonication, rendering more σ^*_{C-O} accessible to the synchrotron beam. The third spectral difference as compared to optimally-sonicated systems is an increased $1s \rightarrow \sigma^*_{C-H}$ resonance, possibly reflecting an increased hydrogen content. Indeed, sonication-induced graphitic damage resulting in dangling bonds may be readily passivated with hydrogen moieties.[26]

Spectral evolutions captured at glancing, magic and normal angles are not immediately evident. Indeed, the lack of angular-dependence in $\pi^*_{C=C}$ resonances (Figure 7.4a) is explained by the lack of strain-induced CNT alignment (Figure 7.2), compounded with low intensities as described above. On the polymeric side, angular-resolved $\pi^*_{C=O}$ resonance intensities have been exploited in prior chapters to reveal conformation effects, given the efficiency of NEXAFS spectroscopy in probing bond directionality.[1,9,27,28] Here, these intensities can further inform on the interactions following a stick-slip mechanism. Figure 7.4b shows the angular- and strain-resolved $\pi^*_{C=O}$ intensities extracted from Figure 7.4a. Through linear interpolations on both strain and angle axes, the map provides a reasonable description of the angular momentum. Where the interpolation was not valid due to sparse measurements

[26] S. Banerjee et al. *ChemPhysChem*, **5**: 1416–1422, 2004.
[27] A. D. Winter et al. *Langmuir*, **29**: 15822–15830, 2013.
[28] J. Stöhr. *NEXAFS Spectroscopy*. Springer, 2003.

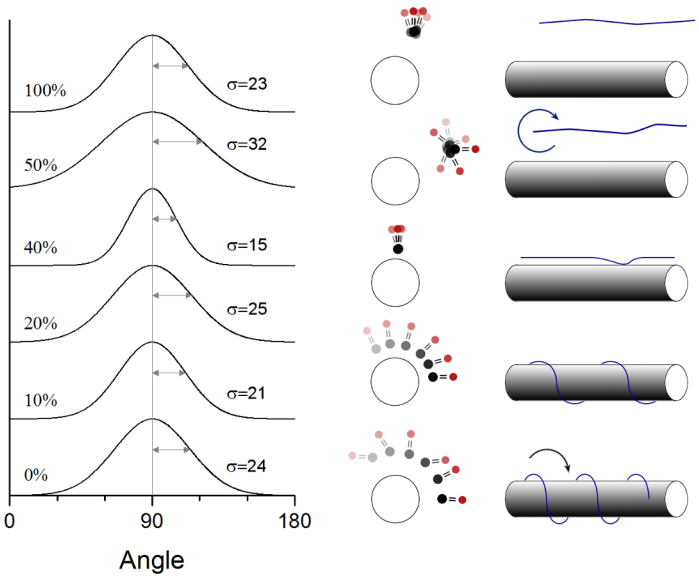

Figure 7.5: Angular frequency distributions of C=O polymeric groups from different composites (left) obtained by Gaussian fitting the mirror-symmetrised cross-sections at the three measured angles from Figure 7.4b, which are consistent with polymer unwrapping through stick-slip mechanism followed by backbone twisting (right). Adapted with permission.[8] Copyright 2015 American Chemical Society.

(i.e. between 50% and 100% strain), the map has been obscured.

For all strains, higher intensities are measured under 90° and lower under 20°, revealing that—given the symmetry of the π bond—polymeric C=O groups are predominantly oriented along the surface normal. This preferential orientation has been seen across a wide range of polymeric systems.[9,27,29] Though this is true across all strains, the intensity dynamic range evolves considerably with increasing strain.

7.6 Model: stick-slip dynamics and backbone twisting

To aid interpretation of the map in Figure 7.4b, it's useful to consider two extreme polymeric configurations: in a perfectly aligned system, with all C=O groups aligned at 90°, the dynamic range would be maximal, and the C=O angular frequency distribution would be represented by a delta function; on the other hand, a completely isotropic configuration would yield zero dynamic range (since there are C=O groups oriented at every angle), and the angular frequency distribution would be constant. In fact, the dynamic intensity range at each strain is inversely proportional to the angular frequency distribution which aids the prediction of polymeric orientations; thus Figure 7.5 shows the angular frequency distribution of C=O

[29]T. Gross et al. *Appl. Surf. Sci.*, **68**: 291–298, 1993.

groups at every strain, modelled by fitting the mirror-symmetrised angular intensities with Gaussian curves, and characterised by their standard deviation σ. This procedure suggests that the C=O populations available to the synchrotron beam lying within 85–95° for 0, 10, 20, 40, 50, and 100% strains are 17%, 19%, 16%, 26%, 12% and 17%.

From the above findings, the σ increase from 0% to 20% strain predicts pendant C=O groups tending towards a more isotropic configuration, as depicted in the cross-sectional view in Figure 7.5. Conversely, σ significantly decreases at 40%, suggesting a considerably anisotropic arrangement of C=O groups. Unsurprisingly, σs seem to follow an oscillatory trend, which resonates with that found for D* band shifts in Raman spectra (Figure 7.3b), which were attributed to stick-slip behaviour.

The lateral view in Figure 7.5 shows a polymeric chain wrapped around a CNT at 0% strain. As was discussed in prior chapters, polymer wrapping through cooperative CH−π interactions is a universal phenomenon.[30,31] With increasing strain, the model shows the chain unwrapping through a stick-slip mechanism until 40%, where the chain is depicted anchored to the nanotube by only one point. At 50% strain, and again, predicted by Raman spectroscopy, the few interactions binding the chain to the CNT break, and the chain becomes completely detached. The subsequent change in σs may be explained by further strain promoting polymeric backbone twisting. Incidently, this twisting has been the subject of much research in the field of photovoltaic devices, where the overlap in molecular orbitals of conjugated polymers promoted by backbone twisting results in increased ionization potentials.[32]

Figure 7.6 describes a model which supports all findings from NEXAFS and Raman spectroscopies. Aggressive sonication results in graphitic damage—seen clearly in TEM micrographs—which perturbs the native π system in CNTs (Figure 7.6a).[3,5] Indeed, carbon vacancies will likely induce rehybridisation of surrounding atoms from sp^2 to sp^3, as suggested by significantly decreased $1s \rightarrow \pi^*_{C=C}$ and increased $1s \rightarrow \sigma^*_{C-H}$ transition intensities in NEXAFS spectra (Figure 7.4a), as well as weak Raman G bands (indicative of sp^2 carbon), which present sporadic G– intensities (Figure 7.2a). Suboptimal π systems in CNTs will hinder optimal PyChol functionalisation through π–π interactions.[2,9] Consenquently, embedding MWCNT–PyChol ensemble into EVA matrix results in polymeric chains interacting with CNTs—which can readily rebundle—directly through CH−π interactions (Figure 7.6b). Like the frustrated π–π interactions, suboptimal CH−π interactions are also expected, relying on now damaged π systems. Nevertheless, some extent of polymeric wrapping will likely occur, as is widely reported in the literature.[9,27,30]

[30]D. Baskaran, J. W. Mays, and M. S. Bratcher. *Chem. Mater.*, **17**: 3389–3397, 2005.
[31]I. Gurevitch and S. Srebnik. *J. Chem. Phys.*, **128**: 144901, 2008.
[32]S. Ko et al. *J. Am. Chem. Soc.*, **134**: 5222–5232, 2012.

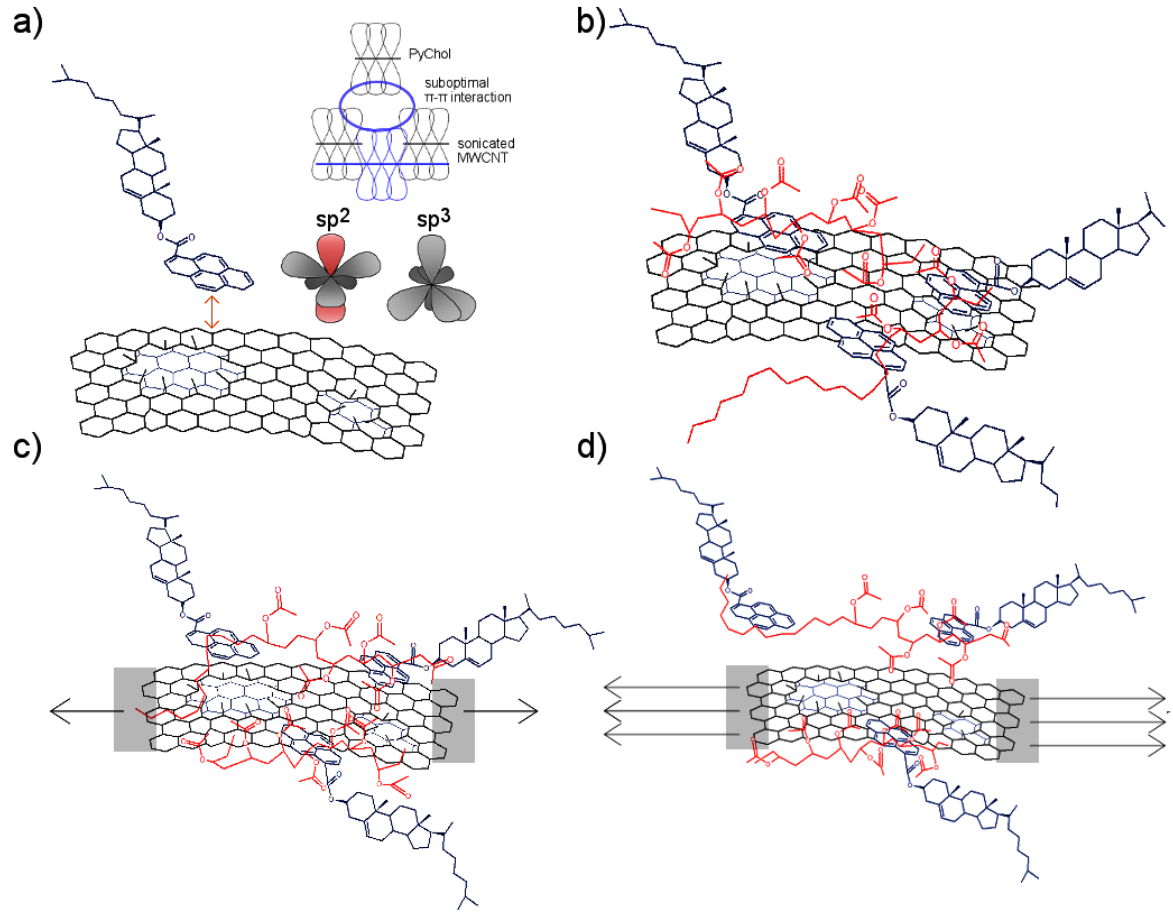

Figure 7.6: Molecular interactions model. a) Damage to MWCNT walls, caused by aggressive sonication, interrupts the pristine π system and hinders optimal π-π noncovalent interactions with PyChol molecules; b) EVA chains interact mostly with MWCNTs directly through CH-π interactions; c) Under small strains, some residual strain is transferred to MWCNTs, but chains begin to unwrap through stick-slip dynamics, preventing MWCNT alignment; d) Higher strains cause chains to completely detach, with further strain resulting in backbone twisting. Reprinted with permission.[8] Copyright 2015 American Chemical Society.

As was shown through Raman spectroscopy and AFM (Figure 7.2), straining does not promote CNT alignment, unlike the system under optimal sonication parameters.[2,9] Instead, under increasing strain up to 40% polymers gradually unwrap from CNTs through stick-slip mechanisms (Figure 7.6c), as evidenced by Raman D* band shifts (Figure 7.3). This is clearly a direct consequence of poor non-covalent interactions between chains and nanotubes, either through PyChol or directly, which are insufficiently strong to transfer the load from chains to CNTs. Instead, after some initial load transfer ('stick'), the matrix yields ('slip').

Eventually, polymeric chains detach completely at higher strains (Figure 7.6d). The blue-shifted Raman D* band at 50% strain (Figure 7.3b) is clearly reflective of the new chemical

environment rendered by broken non-covalent interactions.[22] Subsequent strain on detached polymeric chains results in backbone twisting, revealed by continually changing NEXAFS $\pi^*_{C=O}$ dynamic intensity range at 100% strain.

7.7 Summary

The effects of excessive sonication on non-covalent interactions in EVA|MWCNT composites is drastic. Reduction of sonication volume by a factor of four, which increases the acoustic energy density by the same factor, rendered mechanically inactive composites. The reason for this becomes clear through TEM, AFM, Raman and NEXAFS characterisation: significant sonication-induced damage to CNT structures prevents formation of efficient non-covalent π–π interactions between PyChol and CNTs and CH—π interactions between PyChol and EVA chains. The same physical phenomena occurring upon optical or thermal excitation in CNTs within the mechanically active composites discussed in prior chapters presumably occurs here. However, suboptimal interactions within the excessively sonicated composites prevent the propagation of these phenomena from the CNTs at the nanometre level to the bulk composite at the micron scale.

Bibliography

[1] A. D. Winter, C. Jaye, D. A. Fischer, M. Omastová, and E. M. Campo. Prestrain relaxation in non-covalently modified ethylene-vinyl acetate | PyChol | multiwall carbon nanotube nanocomposites. *APL Materials*, **2**: 066105, 2014.

[2] K. Czaniková, I. Krupa, M. Ilčíková, P. Kasák, D. Chorvár, M. Valentin, M. Šlouf, J. Mosnáček, M. Mičušík, and M. Omastová. Photo-actuating materials based on elastomers and modified carbon nanotubes. *Journal of Nanophotonics*, **6**: 810707, 2011.

[3] K. L. Lu, R. M. Lago, Y. K. Chen, M. L. H. Green, P. J. F. Harris, and S. C. Tsang. Mechanical damage of carbon nanotubes by ultrasound. *Carbon*, **34**: 814–816, 1996.

[4] Y. Y. Huang, T. P. J. Knowles, and E. M. Terentjev. Strength of nanotubes, filaments, and nanowires from sonication-induced scission. *Advanced Materials*, **21**: 3945–3948, 2009.

[5] Y. Y. Huang and E. M. Terentjev. Dispersion of carbon nanotubes: mixing, sonication, stabilization, and composite properties. *Polymers*, **4**: 275–295, 2012.

[6] M. D. Rossell, C. Kuebel, G. Ilari, F. Rechberger, F. J. Heiligtag, M. Niederberger, D. Koziej, and R. Erni. Impact of sonication pretreatment on carbon nanotubes: A transmission electron microscopy study. *Carbon*, **61**: 404–411, 2013.

[7] K. G. Dassios, P. Alafogianni, S. K. Antiohos, C. Leptokaridis, N.-M. Barkoula, and T. E. Matikas. Optimization of sonication parameters for homogeneous surfactant-assisted dispersion of multiwalled carbon nanotubes in aqueous solutions. *The Journal of Physical Chemistry C*, **119**: 7506–7516, 2015.

[8] A. D. Winter, K. Czaniková, E. Larios, V. Vishniyakov, C. Jaye, D. A. Fischer, M. Omastová, and E. M. Campo. Interface Dynamics in Strained Polymer Nanocomposites: Stick-Slip Wrapping as a Prelude to Mechanical Backbone Twisting Derived from Sonication-Induced Amorphization. *The Journal of Physical Chemistry C*, **119**: 20091–20099, 2015.

[9] A. D. Winter, E. Larios, F. M. Alamgir, C. Jaye, D. A. Fischer, M. Omastová, and E. M. Campo. Thermo-active behaviour of ethylene-vinyl acetate | multiwall carbon nanotube composites examined by in situ near edge x-ray absorption fine structure spectroscopy. *The Journal of Physical Chemistry C*, **118**: 3733–3741, 2014.

[10] J. S. Taurozzi, V. A. Hackley, and M. R. Wiesner. Preparation of nanoparticle dispersions from powdered material using ultrasonic disruption. *NIST Special Publication*, **1200-2**: 1–15, 2012.

[11] J. Y. Huang, F. Ding, and B. I. Yakobson. Dislocation dynamics in multiwalled carbon nanotubes at high temperatures. *Physical review letters*, **100**: 035503, 2008.

[12] M. S. Dresselhaus, A. Jorio, M. Hofmann, G. Dresselhaus, and R. Saito. Perspectives on carbon nanotubes and graphene Raman spectroscopy. *Nano Letters*, **10**: 751–758, 2010.

[13] J. H. Lehman, M. Terrones, E. Mansfield, K. E. Hurst, and V. Meunier. Evaluating the characteristics of multiwall carbon nanotubes. *Carbon*, **49**: 2581–2602, 2011.

[14] A. Jorio, M. A. Pimenta, A. G. Souza Filho, R. Saito, G. Dresselhaus, and M. S. Dresselhaus. Characterizing carbon nanotube samples with resonance Raman scattering. *New Journal of Physics*, **5**: 139, 2003.

[15] R. A. DiLeo, B. J. Landi, and R. P. Raffaelle. Purity assessment of multiwalled carbon nanotubes by Raman spectroscopy. *Journal of Applied Physics*, **101**: 064307, 2007.

[16] A. Hirsch. Functionalization of single-walled carbon nanotubes. *Angewandte Chemie International Edition*, **41**: 1853–1859, 2002.

[17] S. Abbasi, P. J. Carreau, and A. Derdouri. Flow induced orientation of multiwalled carbon nanotubes in polycarbonate nanocomposites: Rheology, conductivity and mechanical properties. *Polymer*, **51**: 922–935, 2010.

[18] M. S. Dresselhaus, G. Dresselhaus, R. Saito, and A. Jorio. Raman spectroscopy of carbon nanotubes. *Physics reports*, **409**: 47–99, 2005.

[19] O. Lourie and H. D. Wagner. Evaluation of Young's modulus of carbon nanotubes by micro-Raman spectroscopy. *Journal of Materials Research*, **13**: 2418–2422, 1998.

[20] X. Yan, T. Itoh, Y. Kitahama, T. Suzuki, H. Sato, T. Miyake, and Y. Ozaki. A Raman spectroscopy study on single-wall carbon nanotube/polystyrene nanocomposites: mechanical compression transferred from the polymer to single-wall carbon nanotubes. *The Journal of Physical Chemistry C*, **116**: 17897–17903, 2012.

[21] N. Lachman, C. Bartholome, P. Miaudet, M. Maugey, P. Poulin, and H. D. Wagner. Raman response of carbon nanotube/PVA fibers under strain. *The Journal of Physical Chemistry C*, **113**: 4751–4754, 2009.

[22] P. M. Ajayan, L. S. Schadler, C. Giannaris, and A. Rubio. Single-walled carbon nanotube-polymer composites: strength and weakness. *Advanced Materials*, **12**: 750–753, 2000.

[23] M. A. Pimenta, G. Dresselhaus, M. S. Dresselhaus, L. G. Cancado, A. Jorio, and R. Saito. Studying disorder in graphite-based systems by Raman spectroscopy. *Physical Chemistry Chemical Physics*, **9**: 1276–1290, 2007.

[24] L. S. Schadler, S. C. Giannaris, and P. M. Ajayan. Load transfer in carbon nanotube epoxy composites. *Applied Physics Letters*, **73**: 3842, 1998.

[25] S. L. Ruan, P. Gao, X. G. Yang, and T. X. Yu. Toughening high performance ultrahigh molecular weight polyethylene using multiwalled carbon nanotubes. *Polymer*, **44**: 5643–5654, 2003.

[26] S. Banerjee, T. Hemraj-Benny, M. Balasubramanian, D. Fischer, J. A. Misewich, and S. S. Wong. Surface chemistry and structure of purified, ozonized, multiwalled carbon nanotubes probed by NEXAFS and vibrational spectroscopies. *ChemPhysChem*, **5**: 1416–1422, 2004.

[27] A. D. Winter, E. Larios, F. M. Alamgir, C. Jaye, D. A. Fischer, and E. M. Campo. Near-edge x-ray absorption fine structure studies of electrospun poly (dimethylsiloxane)/poly (methyl methacrylate)/multiwall carbon nanotube composites. *Langmuir*, **29**: 15822–15830, 2013.

[28] J. Stöhr. *NEXAFS Spectroscopy*. Springer, 2003.

[29] T. Gross, A. Lippitz, W. Unger, C. Wöll, G. Hähner, and W. Braun. Some remarks on fitting standard-and high resolution C 1s and O 1s x-ray photoelectron spectra of PMMA. *Applied Surface Science*, **68**: 291–298, 1993.

[30] D. Baskaran, J. W. Mays, and M. S. Bratcher. Noncovalent and nonspecific molecular interactions of polymers with multiwalled carbon nanotubes. *Chemistry of Materials*, **17**: 3389–3397, 2005.

[31] I. Gurevitch and S. Srebnik. Conformational behavior of polymers adsorbed on nanotubes. *The Journal of chemical physics*, **128**: 144901, 2008.

[32] S. Ko, E. T. Hoke, L. Pandey, S. Hong, R. Mondal, C. Risko, Y. Yi, R. Noriega, M. D. McGehee, and J.-L. Brédas. Controlled conjugated backbone twisting for an increased open-circuit voltage while having a high short-circuit current in poly (hexylthiophene) derivatives. *Journal of the American Chemical Society*, **134**: 5222–5232, 2012.

Chapter 8

Conclusions

Mass adoption of PNC technology is hindered by the incomplete understanding of the processing–structure–property relationship. This fundamental gap makes reproducibility a nontrivial issue, and is the main obstacle preventing tailoring of PNC properties and materials by design. One possible route towards overcoming this limitation is through studies of PNC systems which isolate particular processing variables, thus creating a large database. When the database is sufficiently populated, it can be mined using machine learning approaches to elucidate this key processing–structure–property paradigm. To this end, this thesis reported NEXAFS spectroscopy investigations of four PNC case studies, focussed on various processing and nanostructural parameters which condition the final properties at the macroscale.

The study of PDMS–PMMA|MWCNT composites addressed the interactions resulting from electrospinning, which is seldom investigated. It also discussed the CNT diameter dependence on such interactions. Good electrospinning-induced alignment of CNTs within the polymeric fibres was observed through SEM, consistent with prior reported findings, and multiple NEXAFS acquisitions from various irradiated areas in the samples produced identical spectra, suggesting chemical homogeneity at the macroscale. However, SEM also showed fibres with no CNTs: this suggests magnetic stirring alone did not sufficiently disperse CNTs within the polymer blend solution.

Angle-resolved NEXAFS of all samples revealed a distinct signature acquired at glancing angle; comparison with spectra reported in the literature suggested this glancing spectra were PMMA, while normal and magic spectra were PDMS. Indeed, well-known phase segregation between PDMS and PMMA was observed through SEM. Interfacial energy calculations predicted CNTs to lie within the PMMA phase. This is an important consideration, since PMMA was initially introduced as a carrier for electrospinning, but in fact formed the matrix–filler interface—the possible origin for PNC properties. The interface was probed in NEXAFS spectra through glancing incidence angles, and revealed significant differences depending

on CNT diameter. Spectra suggested stronger interactions with larger-diameter CNTs. Both non-covalent interaction models proposed support the notion of stronger interactions with larger diameter. CH–π interactions involve C–H groups in the chains and π system in CNTs: the latter increasingly distorts with decreasing diameter (increasing curvature), allowing better interactions with larger-diameter CNTs. Likewise, the proposed hydrogen bonding scheme requires impurities on CNT sidewalls, and higher NEXAFS intensities arising from such impurity states were recorded for larger CNTs. CNT diameter is therefore another important variable when strong non-covalent interactions are required.

The case study of freshly synthesised thermoactive EVA|MWCNT composites was a good platform to investigate the processing–structure–property relationship in this particular PNC by first observing structural parameters derived from sonication, functionalisation, and uniaxial strain (processing–structure), followed by the *in situ* temperature–resolved NEXAFS study of macroscopic actuation (structure–processing).

Both Raman and NEXAFS spectroscopies showed good alignment induced by straining, the latter also showing alignment of the polymeric chains. Sonication in the presence of PyChol compatibiliser was expected to non-covalently functionalise CNTs and sufficiently disperse them throughout the matrix. Repeated NEXAFS acquisitions indeed confirmed macroscopic homogeneity (good dispersion was reported elsewhere).

In situ excitation revealed a coupled interplay in NEXAFS $\pi^*_{C=C}$ (increasing with temperature) and $\pi^*_{C=O}$ (decreasing with temperature) resonance intensities strongly suggesting conformational effects from CNTs and EVA respectively, possibly responsible for macroscopic actuation. This effect was accentuated in strained composite, indicating that alignment in this system is required for actuation. More, angle-resolved spectra showed a transition of C=O groups in EVA from anisotropic to isotropic as the temperature increased.

The proposed actuation model based on CNT torsion provides explanations to these observations. Inverse intensity trends in $\pi^*_{C=C}$ and $\pi^*_{C=O}$ NEXAFS intensities can be explained as higher accessible $\pi^*_{C=C}$ states as CNTs become more uniaxially aligned, whereas the initially aligned chains become isotropically distributed, decreasing the number of C=O groups accessible to the beam at any particular angle. For this nanoscale effect to propagate constructively to the macroscale, CNTs need to be aligned with respect to each other—hence the decreased trends observed for unstrained composites.

This actuation model needs to be verified: first through similar studies of other 'smart' PNCs such as PDMS|MWCNT composites, and secondly, with other external stimuli (e.g. light). Indeed, a limitation of this investigation is the lack of a cooling mechanism, required under ultra-high vacuum conditions if the actuation reversibility is to be studied.

Identical EVA|MWCNT composite systems were investigated one year after synthesis to

study the lifetime of non-covalent interactions. NEXAFS spectra acquired at room temperature revealed drastic ageing effects. This time, strained and unstrained composites were spectrally identical, and repeated acquisitions showed significant chemical inhomogeneity.

Phase-mode AFM micrographs were key in identifying PyChol molecules as the failure points in these particular composites. Non-covalent π–π interactions degraded and PyChol molecules unlatched from CNTs and segregated. *In situ* temperature-resolved NEXAFS still showed increasing $\pi^*_{C=C}$ resonance intensities from CNTs with increasing temperature, but this time without the coupled decrease in $\pi^*_{C=O}$ intensities. This suggested that initial actuation phenomena in CNTs still occurred, but the matrix–filler interface—through PyChol molecules—was broken, preventing propagation of nanoscale actuation to the macroscopic bulk.

Semiquantitative analysis of ageing-derived failure identified first a natural lifetime of π–π interactions, but this was dramatically accelerated by strain relaxation. Current methodologies used for straining and non-covalent functionalisation, therefore, although producing well aligned and well dispersed nanoparticles within the polymer matrix, limit the durability. Covalent functionalisation, on the other hand, would result in considerably stronger interactions, but necessarily compromises the π system in CNTs, possibly responsible for initial actuation. Alternative dispersion and alignment procedures are therefore needed for long-lived actuation.

The final case study was in principle identical to the previous two i.e. MWCNT sonicated in the presence of PyChol compatibiliser and dispersed within an EVA matrix. Yet the was one critical difference in the processing scheme: the sonicated volume was four times smaller. Even with the same sonication parameters, this resulted in a fourfold increase in acoustic energy density.

Even freshly synthesised, these composites were macroscopically thermally innactive, and TEM micrographs offered an immediate explanation. This time, CNTs were heavily damaged by sonication, which, disrupting the π system, prevented π–π interactions with PyChol dispersant. Highlighting the interdependence of nanostructural parameters, compromised CNT structures prevented the formation of effective matrix–filler interfaces. In turn, this prevented filler alignment through uniaxial strain, which had priorly succeeded. Instead, in this excessively sonicated scheme, increasing strain progressively unwrapped weakly-bound polymeric chains from CNTs through stick and slip dynamics. Further strain, after the chains completely detached, caused polymeric backbone twisting, evidenced by NEXAFS $\pi^*_{C=O}$ intensity fluctuations.

Sonication is widely used in PNC fabrication because of its effectiveness in breaking CNT bundles and achieving good dispersions within polymer matrices. Yet only vague parameters

are typically reported. This case study highlights the need for controlling every variable in sonication to prevent damage, and to achieve reproducible results.

The findings presented here contribute to knowledge of the fundamental gap in PNC technology, highlighting particular issues that are not often considered but have important consequences e.g. lifetime of non-covalent interactions as a consequence of processing methodologies. Further, they provide additional points in the growing dataset found in the literature, which could be exploited by machine learning, clustering algorithms and other big data approaches to extrapolate the processing–structure–property paradigm needed for PNCs to reach their potential.

Appendix A

Collaborations and authorship

The work presented here is the result of several collaborations. This appendix acknowledges the work not performed by the PhD candidate, crediting the appropriate individuals.

Chapter 4—Electrospun PDMS–PMMA|MWCNT composites

- Composite synthesis was performed by Dr Eva M. Campo at the University of Pennsylvania, Philadelphia, USA.
- SEM and TEM characterisation was performed by Dr Eva M. Campo, Laboratory for Matter Dynamics, Bangor Univeristy, UK.

Chapter 5—EVA|MWCNT composites: Thermoactive behaviour

- Composite synthesis was performed by Klaudia Czaniková, from Mária Omastová's research group in Polymer Institute, Slovak Academy of Sciences, Bratislava, Slovakia.

Chapter 7—Excessive sonication in EVA|MWCNT composites

- Composite synthesis was performed by Klaudia Czaniková, from Mária Omastová's research group in Polymer Institute, Slovak Academy of Sciences, Bratislava, Slovakia.
- Aberration-corrected TEM characterisation was performed by Dr Eva M. Campo, Laboratory for Matter Dynamics, Bangor Univeristy, UK.